Diffusion MRI of Complex Tissue Structure

by

David Solomon Tuch

B.A., Physics, University of Chicago (1996)

Submitted to the Division of Health Sciences and Technology
in partial fulfillment of the requirements for the degree of

Doctor of Philosophy in Biomedical Imaging

at the

MASSACHUSETTS INSTITUTE OF TECHNOLOGY

January 2002
[February 2002]

Author .....
Division of Health Sciences and Technology
January 11, 2002

Certified by.....
Van Jay Wedeen
Associate Professor of Radiology, Harvard Medical School
Thesis Supervisor

Certified by.....
John Belliveau
Associate Professor of Radiology, Harvard Medical School
Thesis Supervisor

Accepted by .....
Martha L. Gray
Edward Hood Taplin Professor of Medical and Electrical Engineering
Co-director, Harvard-MIT Division of Health Sciences and Technology

Diffusion MRI of Complex Tissue Structure

by

David Solomon Tuch

Submitted to the Division of Health Sciences and Technology
on January 11, 2002, in partial fulfillment of the
requirements for the degree of
Doctor of Philosophy in Biomedical Imaging

Abstract

Magnetic resonance diffusion imaging provides an exquisitely sensitive probe of tissue microstructure. Owing to the microscopic length scale of diffusion in biological tissues, diffusion imaging can reveal histological architecture irresolvable by conventional magnetic resonance imaging methods. However, diffusion imaging methods to date have chiefly been based on analytical models of the underlying diffusion process. For example, diffusion tensor imaging assumes homogeneous Gaussian diffusion within each voxel, an assumption which is clearly invalid for the vast majority of the brain at presently achievable voxel resolutions.

In this thesis I developed a diffusion imaging method capable of measuring the microscopic diffusion function within each voxel. In contrast to previous approaches to diffusion imaging, the method presented here does not require any assumptions on the underlying diffusion function. The model-independent approach can resolve complex intravoxel tissue structure including fiber crossing and fiber divergence within a single voxel. The method is capable of resolving not only deep white matter intersections, but also composite tissue structure at the cortical margin, and fiber-specific degeneration in neurodegenerative pathology. In sum, the approach can reveal complex intravoxel tissue structure previously thought to be beyond the scope of diffusion imaging methodology.

Thesis Supervisor: Van Jay Wedeen
Title: Associate Professor of Radiology, Harvard Medical School

Thesis Supervisor: John Belliveau
Title: Associate Professor of Radiology, Harvard Medical School

Acknowledgments

I would first and foremost like to express my deep gratitude to my advisers Jack Belliveau and Van Wedeen. My many discussions with Jack and Van provided invaluable advice on science and life. Jack encouraged me to have a scientific dream and with Van helped me realize that dream. I would also like to express my deep thanks to my thesis readers Anders Dale and David Cory for their support and helpful comments. I am also indebted to my unofficial cosupervisor, John George of the Los Alamos National Lab, Biophysics Group. John provided invaluable advice on the conductivity project not to mention the breathtaking aerial tours of the Los Alamos canyons.

I feel fortunate to have been at the Massachusetts General Hospital Martinos Center during a period of tremendous growth. The Center, under the inspirational leadership of Bruce Rosen, provided a fantastically vibrant environment in which to come of intellectual age. I particularly valued my interactions with Bruce Fischl, Tim Davis, Vitaly Napdov, Nikos Makris, David Kennedy, Roger Tootell, David Salat, Ken Kwong, Eric Halgren, Tim Reese, Robert Weisskoff, Ona Wu, Rick Hoge, Bruce Jenkins, Rick Dijkhuizen, Krastan Blagoev, and Diana Rosas. I would also like to thank Greg Sorensen for helping to implement many of the methods developed here in the clinic. Thanks are also due to Rick Hoge, Vitaly Napdov, and Krastan Blagoev for proofreading the thesis. Their comments were invaluable. Needless to say, any remaining mistakes are my own.

Thanks to my friends: Jesse Quinn, Vitaly Napadov, Paul Murphy, John Carney, Matthias Gruson, Jeff Girshman, Pablo Redondo, Ed Moffett, Melinda Papowitz, Neil Katz, Scott Packard, Sham Sokka, David Rosenberg, Marc Burock, Ngon Dao, Seth Birnbaum, Ciamac Moallemi, Patrick Purdon, Sari Levanen, Alex Barnett, Liz Canner, and Nouchine Hadjikhani. Thanks everybody for the welcome diversions, the support, the road trips, and trouble making excursions too numerous to mention.

I never would have been able to have finished the document you are now reading were it not for the unwavering love and support of my family: my father, Ronald Tuch, my mother, Gail Tuch, my sister, Becky Tuch, my girlfriend, Mette Wiegell,

and my as yet unnamed son. My father gave me the precious gift of caring about thinking, and my mother, the gift of thinking about caring. My sister taught me the how to care about the spirit, and Mette taught me the nature of true love. As for my expected son, I am sure he has a thing or two he plans on teaching me. This thesis is dedicated to them.

Support

I would like to thank the generous financial support from the organizations which made this work possible. The work presented in this thesis was supported by the Sol Goldman Charitable Trust, an NIH grant (5RO1 NS 38477-02), and a Human Brain Project/Neuroinformatics research project grant (MH 60993-04) to Los Alamos National Laboratory and Massachusetts General Hospital which was funded jointly by the National Center for Research Resources, National Institute of Mental Health, National Institute of Drug Abuse, and the National Science Foundation.

Contents

1 Introduction **21**

1.1 Introduction 21

1.2 Motivation 22

1.3 Outline 22

1.4 Original Contributions 24

2 A Brief History **25**

2.1 Brownian Motion 25

2.2 Diffusion NMR 27

2.3 Diffusion MRI 28

2.4 Diffusion Tensor MRI and Beyond 29

2.4.1 Diffusion Anisotropy 29

2.4.2 The Tensor Model 30

2.5 References 31

3 Principles of Diffusion Physics **35**

3.1 Preface 35

3.2 Diffusion Physics 36

3.2.1 Molecular Hydrodynamics of Diffusion 36

3.2.2 Diffusion Propagator 38

3.2.3 Diffusion Equation 39

3.2.4 Free Diffusion 40

3.2.5 Restricted Diffusion 41

3.2.6 Spectral Decomposition 42
3.2.7 From the Ensemble-Average Propagator to Microgeometry . . 43
3.2.7.1 The Structure Factor from the Long-Time Limit . . 44
3.2.7.2 The Return-to-Origin Probability and the Spectral Sum 45
3.3 Discussion 46
3.4 References 48

4 Principles of Diffusion NMR and MRI **53**
4.1 Introduction 53
4.2 Diffusion NMR 54
4.2.1 The Bloch-Torrey Equations 54
4.2.2 Pulsed Gradient Spin Echo Experiment 55
4.2.2.1 The Stejskal-Tanner Equation 57
4.2.2.2 The Fourier Relationship 57
4.3 Relation to Microgeometry 60
4.3.1 The Pore Autocorrelation from the Long Time Limit 60
4.3.2 The Return-To-Origin Probability and the Spectral Sum . . . 61
4.3.3 Free Diffusion 62
4.4 Diffusion MRI 62
4.4.1 Diffusion-Weighted Imaging 62
4.4.2 Diffusion Tensor Imaging 62
4.4.2.1 Background 62
4.4.2.2 Diffusion Tensor Reconstruction 63
4.4.2.3 Diffusion Tensor Eigensystem 64
4.4.2.4 Scalar Measures 67
4.5 Discussion 69
4.6 References 70

5 Cross-Property Relations / Conductivity Tensor Mapping **73**
5.1 Preface 73
5.2 Abstract 74

5.3 Introduction 74
5.4 Model 76
5.4.1 Cross-Property Relation 77
5.4.2 Bounds 80
5.5 Methods 81
5.5.1 MRI Methods 81
5.5.2 Comparison to Invasive Measurements 81
5.6 Results 82
5.7 Discussion 83
5.8 References 86

6 Thalamic Parcellation **91**
6.1 Preface 91
6.2 Abstract 91
6.3 Introduction 92
6.4 Methods 94
6.4.1 Data Acquisition 94
6.4.2 Automatic Segmentation Procedure 95
6.4.3 Center-of-Mass Comparison 97
6.5 Results 97
6.6 Discussion 105
6.7 Acknowledgments 107
6.8 References 108

7 Multi-Tensor Imaging **115**
7.1 Preface 115
7.2 Introduction 116
7.3 Model 118
7.4 Experimental Methods 119
7.4.1 MRI Methods 119
7.4.2 Multi-Tensor Reconstruction 119

7.5 Results . . . 120
7.5.1 Raw Data . . . 120
7.5.2 Multi-Tensor Reconstruction . . . 120
7.5.3 Comparison to Tensor Model . . . 123
7.6 Discussion . . . 123
7.7 Appendix . . . 125
7.8 References . . . 128

8 Diffusion Spectrum Imaging **131**
8.1 Preface . . . 131
8.2 Abstract . . . 132
8.3 Introduction . . . 132
8.3.1 Q-Space Imaging . . . 133
8.3.2 Modifications to Q-Space Imaging Experiment . . . 135
8.3.2.1 Twice-Refocused Balanced Echo Sequence . . . 135
8.3.2.2 Effectively Constant Gradient . . . 136
8.3.2.3 Modulus Fourier Transform . . . 138
8.3.2.4 Radial Projection Transform . . . 140
8.4 Methods . . . 142
8.5 Results . . . 145
8.5.1 Healthy Volunteers . . . 145
8.5.2 Patients . . . 148
8.6 Discussion . . . 154
8.7 References . . . 158

9 Connectivity Mapping **161**
9.1 Preface . . . 161
9.2 Introduction . . . 162
9.2.1 Tractography . . . 163
9.2.2 Diffusion Spectrum Imaging . . . 164
9.2.3 Generalized Streamline Tractography . . . 167

9.2.4 Volume Segmentation 169
9.2.5 Connectivity Matrix 170
9.2.5.1 Model 170
9.2.5.2 Algorithm 174
9.3 Methods 175
9.3.1 Imaging 175
9.3.2 Connectivity 176
9.3.2.1 Generalized Streamline Tractography 176
9.3.2.2 Volume Segmentation 176
9.3.2.3 Connectivity Matrix 177
9.3.3 Results 178
9.3.3.1 Tractography and Volume Segmentation 178
9.3.3.2 Connectivity Matrix 181
9.3.4 Discussion 184
9.4 References 186

10 Q-Ball Imaging **191**

10.1 Introduction 191
10.2 Theory 193
10.2.1 Fourier Relation 193
10.2.2 Orientation Distribution Function 193
10.2.3 Reciprocal Space Funk Transform 194
10.3 Methods 197
10.3.1 Imaging 197
10.3.2 Reconstruction Algorithm 198
10.4 Results 199
10.5 Discussion 201
10.6 Appendix 204
10.7 References 206

11 Conclusions **207**

11.1 Summary 207

11.2 Open Problems 208

11.2.1 Experimental 208

11.2.2 Theoretical 210

11.3 References 213

A Notation **215**

B Abbrevations **219**

List of Figures

4-1 Pulse diagram for the PGSE experiment 56

4-2 Schematic diagram of the spin phase distribution during the PGSE experiment 56

4-3 Diffusion tensor image of frontal white matter 65

4-4 Isoprobability ellipsoid for a Gaussian diffusion function 66

4-5 Examples of scalar images derived from DTI 69

5-1 Theoretical cross-property relationship between the conductivity and diffusion tensor eigenvalues 81

5-2 Experimental relationship between the conductivity and diffusion tensor eigenvalues 83

5-3 Axial electrical conductivity tensor map of the human brain derived from the linear cross-property relation 84

6-1 Mid-thalamic diffusion tensor images of 4 subjects 98

6-2 Comparison between diffusion tensor image of the thalamus and a histological slice 99

6-3 Automatic segmentation results 100

6-4 Surface rendering of the thalamus 101

6-5 Segmentation results from individual subject 102

6-6 Comparison between center-of-mass coordinates obtained from histological atlas and diffusion tensor segmentation 103

7-1 Gradient directions for the high angular resolution diffusion experiment 119

7-2 Spherical polar plots of the ADC in the fascicle base of the frontal gyri 121
7-3 Comparison of single-tensor and two-tensor fits to diffusion signal . . 122
7-4 Error of the tensor model as a function of the oblateness of the apparent tensor 123
7-5 Single voxel showing disagreement between the ADC function and the two-tensor fit 125

8-1 Pulse sequence diagram for the effectively constant gradient twice-refocused balanced echo (cgTRBE) experiment 135
8-2 Diffusion in a constant magnetic field gradient 137
8-3 Keyhole Cartesian sampling scheme 142
8-4 Schematic diagram of the ODF reconstruction scheme 144
8-5 Subject A: Two sagittal diffusion spectrum images of the brainstem at the level of the pontine decussation 146
8-6 Diffusion propagator taken from a single voxel in the brainstem . . . 147
8-7 Subject B: Comparison of DSI and DTI of the brainstem 147
8-8 Subject B: Comparison of DSI and DTI at a three-way fiber crossing 148
8-9 Subject A: Two sagittal slice diffusion spectrum images of motor cortex 149
8-10 Subject A: Zoomed view of a single slice from Fig. 8-9 150
8-11 Subject C: Axial DSI of the occipital pole 151
8-12 Subject D: Sagittal DSI of patient one year post cingulotomy for OCD 152
8-13 Subject E: Coronal DSI of patient with a resected oligodendroglioma 153
8-14 Subject F: Sagittal DSI of patient with temporal lobe tumor 153
8-15 Subject G: Axial DSI of patient with a chronic thalamic infarct . . . 154
8-16 Subject H: Axial DSI of patient with chronic left occipital stroke . . . 155

9-1 Robust curvature penalty function 168
9-2 Tractography of the antero- and mediodorsal thalamic nuclei 178
9-3 Tractography of the pontine decussation 179
9-4 Projections from the rostral pons 180

9-5 Tractography of the corona radiata, the cingulum, and the corpus callosum 181
9-6 Volume segmentation of the corona radiata, the corpus callosum, the cingulum bundle, and the projections of the cingulum 182
9-7 Example simulated annealing run for the path between primary motor and primary sensorimotor cortices 182
9-8 Connectivity matrix for all test points 183

10-1 The Funk transform 194
10-2 Gradient directions for the q-ball imaging experiment 197
10-3 Comparison of DSI and q-ball images from the intersection of the corpus callosum with the corona radiata 200
10-4 Q-ball image from the temporal lobe 202

List of Tables

6.1 Mean fiber orientations of the individually segmented nuclei 103

6.2 Thalamic nuclei and output projections 104

8.1 Protocols for DSI experiments 142

9.1 Points selected for connectivity matrix calculation 177

Chapter 1

Introduction

"Is there something finished? And some new beginning on the way?"

Carl Sandberg, *Falltime*

1.1 Introduction

While water appers static to the naked eye, at microscopic resolutions the water molecules are in constant random motion. The erratic motion of the molecules in a liquid or gas is a phenomenon termed Brownian motion after the Scottish Naturlist who first observed the phenomenon in pollen grains suspended in water. It was not until Albert Einstein studied the problem, however, did it become clear that Brownian motion is due to the thermal agitation of the water molecules.

Imagine for a moment that we could tag one of the water molecules inside of the brain and chart its migration. We would see that the path taken by the water molecule is shaped by the microscopic structure of the brain tissue. We might see, for example, that the water molecule cannot readily penetrate cells and tends rather to diffuse along the cells. Or we might observe that the water molecule is confined within particular compartments. The path of the water molecule therefore reflects the structure of its microscopic environment. The basic idea of magnetic resonance diffusion imaging is to measure the diffusion of water molecules and use these measurements to probe the underlying structure of the tissue.

1.2 Motivation

Magnetic resonance diffusion imaging provides an exquisitely sensitive probe of tissue microstructure. Owing to the microscopic length scale of diffusion in biological tissues, diffusion imaging can reveal histological architecture irresolvable by conventional magnetic resonance imaging methods. However, diffusion imaging methods to date have chief been based on analytical models of the underlying diffusion process. For example, diffusion tensor imaging assumes homogeneous Gaussian diffusion within each voxel, an assumption which is clearly invalid for the vast majority of the brain at presently achievable voxel resolutions.

In this thesis I developed a diffusion imaging method capable of measuring the microscopic diffusion function within each voxel. In contrast to previous approaches to diffusion imaging, the method does not require any assumptions on the underlying diffusion function. The model-independent approach can resolve complex intravoxel tissue structure including fiber crossing and fiber divergence within a single voxel. The method is capable of resolving not only deep white matter intersections, but also composite tissue structure at the cortical margin, and fiber-specific degeneration in neurodegenerative pathology. Moreover, the ability to disentangle fiber crossing renders computational reconstruction of white matter pathways, the so-called white matter tractography problem, for more tractable. In sum, the approach can reveal complex intravoxel tissue structure previously thought to be beyond the scope of diffusion imaging methodology.

1.3 Outline

This thesis is divided into three parts. In Part I (Chapters 2-4) we briefly review the history of diffusion nuclear magnetic resonance (NMR) and magnetic resonance imaging (MRI) (Chapter 2), and provide the requisite background on diffusion physics (Chapter 3) and diffusion NMR and MRI (Chapter 4).

The techniques introduced in Chapters 3 and 4, specifically the diffusion tensor

imaging (DTI) method, are applied in Part II which consists of Chapters 5 and 6. In 5 we derive a relationship between the water diffusion tensor measured by DTI and the spatial statistics of the underlying tissue microstructure. The relation is used to provide a connection between the water diffusion tensor and the more general family of transport tensors in biological tissue, with a particular emphasis on the electrical conductivity tensor in brain tissue.

In addition to providing insight into transport in tissue, the diffusion tensor can resolve anatomy not seen on conventional MRI. Chapter 6 uses the DTI method to resolve the nuclei of the thalamus, a structure which displays no internal contrast on conventional MRI. Using an automatic segmentation algorithm, we validated the DTI results against a published histological atlas.

While the tensor paradigm employed by DTI provides a constructive framework for diffusion imaging when the fibers are strongly aligned with a voxel, the tensor model is incapable of resolving multiple fiber populations within a voxel such as may arise from fiber crossing or fiber divergence within a voxel. Prompted by the detection of significant secondary structure in the thalamus with DTI, we developed a set of diffusion imaging methods capable of resolving multiple fiber populations within a voxel, architecture irresolvable by the tensor model. The development of these methods forms the basis of Part III which consists of Chapters 7-10.

In Chapter 7 we develop a diffusion imaging reconstruction scheme which can describe a finite mixture of Gaussian diffusion processes. However, the Gaussian mixture modeling approach requires an iterative reconstruction scheme and suffers from possible model misspecification. In Chapter 8 we develop a diffusion imaging method termed diffusion spectrum imaging (DSI) which is capable of resolving the three-dimensional spin displacement probability density function without the need for any assumptions on the analytical form of the underlying diffusion process.

Chapter 9 considers the problem of reconstructing the white matter connectivity of the brain from DSI. We develop three separate approaches to the connectivity problem: streamline tractography, volume segmentation, and connectivity matrix inference. The approaches operate in different spaces, respectively, in path space, in

the anatomical volume, and on the cortical surace, and therefore offer relative analytical and practical advantages. For exampl,e he tractography and connectivity matrix approaches provide reconstructions of the individual white matter pathways, but, additionaly, the ability to express the connectivity matrix solutions on the cortical surface provides a register for inter-subject averaging. Moreover, the probabilistic framework of the connectivity matrix program facilitates hypothesis testing on the connectivity structures within a between subjects.

The DSI method presented in Chapter 8 requires extremely high spatial resolution of the diffusion function. In Chapter 10 we develop a diffusion imaging reconstruction scheme based on the Funk transform which like the DSI method is model-independent, but has the further advantages of not requiring high diffusion spatial resolution and allowing for direct reconstruction of the spin displacement orientation distribution function on the projective space. The development of what we call the q-ball imaging method gives an appealing narrative closure as it builds on the spherical sampling scheme we began with in Chap. 7, and exploits the principle presented in Chapter 8 that the directional contrast-to-noise of the diffusion function is contained in a narrow spatial frequency band.

1.4 Original Contributions

The most significant original contributions of this thesis are (i) the development of a practical experimental method for spin displacement imaging of the human brain *in vivo* (Chap. 8), and (ii) the demonstration that this method can resolve complex intravoxel tissue structure such as fiber crossing within a single voxel. The method opens a whole new class of tissue structural properties for investigation by diffusion imaging. In particular, the method enables the detection of selective white matter fiber loss and rearrangement in white matter disease. I hope that spin displacement imaging will ultimately provide better diagnosis of neurodegenerative disease and help elucidate the connectivity structure of the human brain.

Chapter 2

A Brief History

"The moments of the past do not remain still..."

Marcel Proust, "The Sweet Cheat Gone," *Remembrance of Things Past*

2.1 Brownian Motion

In 1828 the Scottish Naturalist Robert Brown published a pamphlet entitled 'A Brief account of microscopical observations ...'. In this pamphlet Brown recorded that pollen grains of *Clarkia pulchella* suspended in water under a microscope exhibited a peculiar "rapid oscillatory motion" (1). Brown initially believed that such motion was particular to the male sexual cells of plants, but was later startled to observe that pollen of plants suspended in alcohol for almost eleven months exhibited the same erratic motion: a "very unexpected fact of seeming vitality being retained by these 'molecules' so long after the death of the plant." Further studies with not only other organic substances but chips of glass, granite, particles of smoke, and rocks "of all ages" revealed such motion to be a general property of small particles suspended in solution.

The erratic particle motion observed by Brown would remain unexplained until the dawn of the kinetic theory of matter in the third quarter of the nineteenth century. Pioneered by Maxwell, Boltzmann, and Claussius, the kinetic theory of matter introduced the radical concept that the heat of a liquid or gas is mediated by the

constant random thermal motion of the molecules in the medium. The kinetic theory would inspire Weiner to declare in 1863 that the particle motion observed by Brown could not be due to convection currents in the fluid, but was rather due to collisions between the particles and the surrounding molecules of the fluid. The molecular kinetic explanation for Brownian motion was reiterated some years later in 1877 by two Jesuit priests, Fathers Delsaulx and Carbonnelle, but it was not until G.L. Gouy in 1888-9 showed that Brownian motion is more rapid for smaller particles and never reaches equilibrium that the problem of Brownian motion assumed a place among the classical problems of physics.

Albert Einstein, apparently unaware of any of the previous observations of Brownian motion,[1] was motivated to provide an experimentally testable hypothesis for the kinetic-molecular theory of matter when in 1905 he showed how the random thermal motion of the molecules in a liquid or gas could be imparted to larger particles. He predicted that the motion of these larger particles could be observed under the microscope (2, 3) and could therefore provide an experimentally testable hypothesis for the kinetic theory. Einstein's theory accounted for the dependence of the effect on the temperature and viscosity of the solution, and the size of the suspended particle, and thereby provided a set of experimentally testable predictions for the kinetic theory of matter. The same formulation was also developed independently by the Polish mathematician Marian Smoluchowski in 1905-06 albeit with a different approach (4). Einstein's theoretical studies were experimentally confirmed by Jean Babtiste Perrin (5) who measured the dependence of Brownian motion on temperature and particle size. By demonstrating that colloidal particles obey Einstein's formulation, Perrin was able to calculate Avogadro's number and obtain direct verification for the kinetic-molecular theory of gases, a finding which earned him the Nobel Prize for physics in 1926.

While Brownian motion is a microscopic phenomenon it gives rise to a macroscopically observable phenomenon known as diffusion. On a microscopic level, diffusion

[1] In a letter to Michele Besso in January 6, 1948, Einstein wrote that he had "deduced [Brownian motion] from mechanics, without knowing that anyone had already observed anything of the kind".

arises from th microscopic intermingling of the molecules as the result of Brownian motion. While we are familiar with the diffusion of a substance in another host substance, the physics of diffusion makes no essential distinction between the two. Hence, the theory of diffusion can be applied to the diffusion of a substance in its own medium, for example the diffusion of water in water. This phenomenon is referred to as self-diffusion or, with some abuse of terminology, simply diffusion. In the following we briefly review the historical origins of diffusion measurements with nuclear magnetic resonance and the development toward magnetic resonance imaging of diffusion *in vivo*.

2.2 Diffusion NMR

Shortly after the initial discovery of the NMR phenomenon by Bloch (6,7) and Purcell (8), Hahn published his seminal paper (9) on the NMR spin echo in which he noted that the random thermal motion of the spins would reduce the amplitude of the observed spin echo signal in the presence of a magnetic field inhomogeneity. Carr and Purcell (10) shortly after developed a set of equations for relating the echo amplitude attenuation to discrete jumps of the spins. Torrey (11) subsequently developed a continuum description based on the magnetization diffusion equation, the so-called Bloch-Torrey equation.

In their classic paper on the spin diffusion experiment, Stejskal and Tanner (12) developed the methodology and theory of the pulsed gradient spin echo experiment which made possible direct measurement of the diffusion function and opened the window for quantitative measurements of molecular diffusion coefficients. Early work on diffusion in restricted spaces was performed by Woessner (13), Stejskal and Tanner (12,14,15), and Cotts (16,17). The late nineteen seventies and early eighties saw the beginning of diffusion NMR applied to a wide range of biological samples (18–23). Using the diffusion propagator formalism (14,24), Cory (25) demonstrated that the size of a diffusion compartment can be directly inferred from the observed diffusion function, a discovery which enabled quantitative morphometry of the pore spaces in

porous media.

In 1991 Callaghan experimentally demonstrated and provided an elegant theoretical explanation for the diffusion-diffraction phenomenon (26) in which the spin echo signal is observed to decrease non-monotonically as a function of the applied diffusion gradient magnitude. The diffusion-diffraction phenomenon provided a valuable bridge between diffusion NMR and other imaging methods such as inelastic neutron scattering and x-ray crystallography where diffraction effects are commonly observed (27). The late nineties witnessed the application of diffusion NMR to a wide range of complex fluid motions including vortex and shear flow, an evolution which is described in an excellent review by Callaghan (28).

2.3 Diffusion MRI

In 1973 the chemist Paul Lauterbur, then at the State University of New York at Stony Brook, published a groundbreaking paper (29) entitled "Image formation by induced local interactions: Examples employing nuclear magnetic resonance". Lauterbur's key insight was to superimpose a magnetic field gradient on the static uniform magnetic field. Owing to the Larmor principle, different parts of the sample would have different resonance frequencies, and thus, a given resonance frequency could be associated with a given position. Using a technique called backprojection which he borrowed from computerized x-ray tomography, Lauterbur produced an image of a pair of test tubes immersed in a vial of water. He continued to image small objects, including a tiny crab scavenged by his daughter from the Long Island beach near his home.

Meanwhile across the Atlantic at the University of Nottingham, Peter Mansfield had developed a magnetic field gradient scheme called echo-planar imaging (EPI) which did not require repeated excitation-sampling cycles, effectively reducing the required imaging time to tens of milliseconds (30). The EPI method was first implemented in practice in 1984 (31) and on high magnetic field whole body scanners in 1987 (32). The fast imaging times provided by EPI facilitated the development of diffusion MRI which is inherently sensitive to patient motion.

Shortly following the first description of diffusion imaging by Taylor and Bushell (33), Denis LeBihan obtained the first diffusion images on a whole-body system (34, 35). The clinical importance of diffusion imaging became apparent when Michael Moseley's group in San Francisco (36) reported that diffusion imaging can detect ischemic tissue within minutes after stroke in an experimental animal model. Prior, no other imaging technique with the exception of positron emission tomography had been able to discriminate ischemic versus normal tissue at the acute time period after stroke onset. In years following, diffusion imaging has emerged as the standard for diagnosis of early cerebral infarct.

2.4 Diffusion Tensor MRI and Beyond

2.4.1 Diffusion Anisotropy

Diffusion anisotropy refers to the dependence of the apparent diffusion on the direction in which it is measured. In general, anisotropy arises in materials with strongly aligned microstructure such as fibrous biological tissues, or polymers, or nematic liquid crystals. In such materials the diffusion is more restricted perpendicular to the grain of the material than along the axis of the grain. The presence of anisotropy provides a contrast mechanism for detecting the alignment of the material microstructure.

Cleveland (19) was the first to measure anisotropic diffusion in a biological sample, in this case excised skeletal muscle, with diffusion NMR. It was not until 1990 however that images of diffusion anisotropy were obtained *in vivo* by Moseley in the cat spinal cord (37) and Doran and Chenevert in cerebral white matter (38, 39). The study of diffusion anisotropy in biological tissues became systematized with the introduction of the diffusion tensor model by Basser (40).

2.4.2 The Tensor Model

In 1994 Peter Basser (40) introduced the diffusion tensor model to diffusion imaging. The tensor model provided a systematic analytical framework for describing diffusion anisotropy in tissue and entrenched Gaussian diffusion as the dominant model for diffusion imaging of anisotropy. In particular, the identification of the diffusion tensor major eigenvector with the dominant fiber orientation enabled the fiber orientation mapping program.

While the Gaussian diffusion model posited by DTI greatly simplifies the analysis and interpretation of diffusion imaging experiments, the assumption of Gaussian diffusion obscures many phenomena. For example, the tensor model is incapable of describing restricted diffusion, diffusion heterogeneity, or surface relaxation to name but a few examples. The development of a model-independent diffusion imaging paradigm which can resolve these phenomena represents one of the major goals of this thesis.

2.5 References

[1] R. Brown. A brief account of microscopical observations made in the months of June, July, and August 1827 on the particles contained in the pollen of plants; and on the general existence of active molecules in organic and inorganic bodies. *Philosoph. Mag.*, 4:161, 1828.

[2] A. Einstein. Über die von der molekularkinetischen Theorie der Wärme geforderte Bewegung von in ruhenden Flüssigkeiten suspendierten Teilchen. *Ann. Physik.*, 4:549–560, 1905. (English translation in Ref. 41).

[3] A. Einstein. Sue Theorie der Brownschen Bewengung. *Ann. Physik.*, 19:371–381, 1906. (English translation in Ref. 41).

[4] M.R. von Smoluchowski. Zur kinetischen Theorie der Brownschen Molekularbewegung und der Suspensionen. *Ann. Phys.*, 21:756–780, 1906.

[5] J.B. Perrin. Mouvement brownien et réalité moléculaire. *Annales de chimie et de physiqe*, VIII 18:4–114, 1909.

[6] F. Bloch. Nuclear induction. *Phys. Rev.*, 70:460–474, 1946.

[7] F. Bloch, W. W. Hansen, and M. Packard. Nuclear induction. *Phys. Rev.*, 69:127, 1946.

[8] E. M. Purcell, H. C. Torrey, and R. V. Pound. Resonance absorption by nuclear magnetic moments in a solid. *Phys. Rev.*, 69:37, 1946.

[9] E.L. Hahn. Spin echoes. *Phys. Rev.*, 80:580–594, 1950.

[10] H.Y. Carr and E.M. Purcell. Effects of diffusion on free precession in nuclear magnetic resonance experiments. *Phys. Rev.*, 94:630–638, 1954.

[11] H.C. Torrey. Bloch equations with diffusion terms. *Phys. Rev.*, 104:563–565, 1956.

[12] E.O. Stejskal and J.E. Tanner. Spin diffusion measurements: spin echoes in the presence of a time-dependent field gradient. *J. Chem. Phys.*, 42:288–292, 1965.

[13] D.E. Woessner. NMR spin-echo self-diffusion measurements on fluids undergoing restricted diffusion. *J. Phys. Chem.*, 67:1365–1366, 1963.

[14] E.O. Stejskal. Use of spin echoesd in a pulsed magnetic-field gradient to study anisotropic, restricted diffusion and flow. *J. Chem. Phys.*, 43:3597–3603, 1965.

[15] J.E. Tanner and E.O. Stejskal. Restricted self-diffusion of protons in colloidal systems by the pulsed-gradient, spin-echo method. *J. Chem. Phys.*, 49:1768–1777, 1968.

[16] J.S. Murday and R.M. Cotts. Self-diffusion coefficient of liquid lithium. *J. Chem. Phys.*, 48:4938–4945, 1968.

[17] R.C. Wayne and R.M. Cotts. Nuclear-magnetic-resonance study of self-diffusion in a bounded medium. *Phys. Rev.*, 151:264–272, 1966.

[18] R. L. Cooper, D. B. Chang, A. C. Young, C. J. Martin, and B. Ancker-Johnson. Restricted diffusion in biophysical systems. *Biophys. J.*, 14:161–1771, 1974.

[19] G.G. Cleveland, D.C. Chang, and C.F. Hazlewood. Nuclear magnetic resonance measurements of skeletal muscle. Anisotropy of the diffusion coefficient of the intracellular water. *Biophys. J.*, 16:1043–1053, 1976.

[20] J.E. Tanner. Transient diffusion in a system partitioned by permeable barriers. Application to NMR measurements with a pulsed field gradient. *J. Chem. Phys.*, 69:1748–1754, 1978.

[21] J.E. Tanner. Self diffusion of water in frog muscle. *Biophys. J.*, 28:107–116, 1979.

[22] K.R. Brownstein and C.E. Tarr. Importance of classical diffusion in NMR studies of water in biological cells. *Phys. Rev. A*, 19:2446–2453, 1979.

[23] J.E. Tanner. Intracellular diffusion of water. *Arch. Biochem. Biophys.*, 224:416–428, 1983.

[24] J. Kärger and W. Heink. The propagator representation of molecular transport in microporous crystallites. *J. Magn. Reson.*, 51:1–7, 1983.

[25] D.G. Cory and A.N. Garroway. Measurement of translational displacement probabilities by NMR: an indicator of compartmentation. *Magn. Reson. Med.*, 14:435–444, 1990.

[26] P.T. Callaghan, A. Coy, D. Macgowan, K.J. Packer, and F.O. Zelaya. Diffraction-like effects in NMR diffusion studies of fluids in porous solids. *Nature*, 351:467, 1991.

[27] P.T. Callaghan. *Principles of nuclear magnetic resonance microscopy.* Oxford, Great Britain, 1993.

[28] P.T. Callaghan. Rheo-NMR: nuclear magnetic resonance and the rheology of complex fluids. *Rep. Prog. Phys.*, 62:599–670, 1999.

[29] P.C. Lauterbur. Image formation by induced local interactions: examples employing nuclear magnetic resonance. *Nature*, 242:190–191, 1973.

[30] P. Mansfield. Multi-planar image formation using NMR spin echoes. *J. Phys. C*, 10:55–58, 1977.

[31] P. Mansfield. Real-time echo-planar imaging by NMR. *Br. Med. Bull.*, 40:187–190, 1984.

[32] R. Rzedzian and I. Pykett. Instant images of the human heart using a new, whole-body MR imaging system. *Amer. J. Roent.*, 149:245–250, 1986.

[33] D.G. Taylor and M. C. Bushell. The spatial mapping of translational diffusion coefficients by the NMR imaging technique. *Phys. Med. Biol.*, 30:345–349, 1985.

[34] D. LeBihan, E. Breton, D. Lallemand, P. Grenier, E. Cabanis, and M. Laval-Jeantet. MR imaging of intravoxel incoherent motions: application to diffusion and perfusion in neurologic disorders. *Radiology*, 161:401–407, 1986.

[35] D. LeBihan, E. Breton, D. Lallemand, M-L. Aubin, J. Vignaud, and M. Laval-Jeantet. Separation of diffusion and perfusion in intravoxel incoherent motion MR imaging. *Radiology*, 168:497–505, 1988.

[36] M.E. Moseley, Y. Cohen, J. Mintorovitch, L. Chileuittand H. Shimizu, J. Kucharczyj, M.F. Wendland, and P.R. Weinstein. Early detection of regional cerebral ischemia in cats: comparison of diffusion- and T2-weighted MRI and spectroscopy. *Magn. Reson. Med.*, 14:330–346, 1990.

[37] M.E. Moseley, Y. Cohen, J. Kucharczyk, J. Mintorovitch, H.S. Asgari, M.R. Wendland, J. Tsuruda, and D. Norman. Diffusion weighted MR imaging of anisotropic water diffusion in cat central nervous system. *Radiology*, 176:439–446, 1990.

[38] M. Doran, V. Hajnal, N. Van Bruggen, M.D. King, I.R. Young, and G.M. Bydder. Normal and abnormal white matter tracts shown by MR imaging using directional diffusion weighted sequences. *J. Comput. Assist. Tomogr.*, 14:865–873, 1990.

[39] T.L. Chenevert, A. Brunberg, and J.G. Pipe. Anisotropic diffusion in human white matter: demonstration with MR techniques in vivo. *Radiology*, 177:401–405, 1990.

[40] P.J. Basser, J. Mattiello, and D. Le Bihan. MR diffusion tensor spectroscopy and imaging. *Biophys. J.*, 66:259–267, 1994.

[41] A. Einstein. In R. Furthe and A.D. Cowper, editors, *Investigations on the theory of Brownian motion*. Dover, New York, 1956. (Collection of papers translated from the German).

Chapter 3

Principles of Diffusion Physics

"As water is in water."

William Shakespeare, *Antony and Cleopatra*

3.1 Preface

In this section we describe the physical principles governing diffusion in materials with a particular focus on biological tissues. We introduce the diffusion propagator formalism and discuss how properties related to the microgeometry of the material can be inferred from the diffusion propagator. The diffusion-structure relations we present here will be explored more fully in the following chapter on diffusion NMR and MRI.

While this section seeks to present a standard background on diffusion physics relevant to NMR we have included a number of new results where appropriate. Eqns. 3.13, 3.14 represent, to our knowledge, the first time that the complete surface boundary conditions for diffusion with relaxing, partially permeable barriers have been written down. Furthermore, we offer a proof of the positive-definiteness of the diffusion propagator which makes possible the diffusion spectrum imaging and q-ball imaging methods presented in Chaps. 8 and 10.

3.2 Diffusion Physics

Molecular spin diffusion is, simply stated, the random thermal motion of spins. Owing to the microscopic length-scale of diffusion in tissue, the diffusion process provides an exquisitely sensitive probe of tissue microstructure. However, in order to relate the observed diffusion signal to the underlying tissue microstructure, it is helpful to have an understanding of how the diffusion signal is influenced by the tissue geometry and properties. In the present section we introduce the diffusion propagator formalism which provides a remarkably powerful framework for describing and predicting diffusion behavior in complex materials such as biological tissues.

The particle most commonly measured in biological applications is the proton and its most common host is the water molecule. Notwithstanding the work on other nuclei and other metabolic hosts, we will focus this discussion on the behavior of water protons, which, for sake of convenience, we simply refer to as spins. It should be borne in mind, however, that much of the framework developed here is generally applicable to other metabolic species.

3.2.1 Molecular Hydrodynamics of Diffusion

How is the diffusion behavior we observe with NMR related to the underlying molecular hydrodynamics? Let us begin by considering how the statistics of the spin displacement gives rise to the diffusion coefficient and, in the case of anisotropic materials, the diffusion tensor. If we consider the spin position $\mathbf{r}'$ at time 0 and the subsequent spin position $\mathbf{r}$ at time τ then the diffusion coefficient D is given by Einstein's relation (1)

$$D = \frac{1}{6\tau} \langle \mathbf{R}^T \mathbf{R} \rangle \tag{3.1}$$

where $\mathbf{R} = \mathbf{r} - \mathbf{r}'$ is the relative spin displacement as a function of time τ, and $\langle ... \rangle$ is the average over the spin ensemble. For a given diffusion time τ, the diffusion coefficient defines a characteristic length scale

$$\ell = \sqrt{6D\tau} \tag{3.2}$$

which is referred to as variously the Einstein length, the diffusion length, or the mixing length.

In cases where the medium is anisotropic, the Einstein relation easily generalizes to the diffusion tensor

$$\mathbf{D} = \frac{1}{6\tau} \langle \mathbf{R}\mathbf{R}^T \rangle . \tag{3.3}$$

where the diffusion tensor $\mathbf{D}$ is a three-dimensional rank-2 tensor. According to Onsager's hypothesis (2) the diffusion tensor is symmetric ($\mathbf{D} = \mathbf{D}^T$). Refs. 3 and 4 argue that the diffusion tensor is also positive definite.

While the Einstein relation relates the diffusion tensor to the spin position, the diffusion tensor can also be related to the spin velocity through the spin velocity autocorrelation tensor $\boldsymbol{\phi}(\tau)$ (5,6)

$$\boldsymbol{\phi}(\tau) = \mathbf{v}'\mathbf{v}^T. \tag{3.4}$$

where $\mathbf{v}$ is the spin velocity. The spin velocity autocorrelation tensor is related to the diffusion tensor through the Green-Kubo relation (6–8)

$$\mathbf{D} = \frac{1}{3} \int_0^\infty \langle \boldsymbol{\phi}(\tau) \rangle d\tau \tag{3.5}$$

The normalized scalar velocity autocorrelation

$$\hat{\phi}(\tau) = \mathbf{v}^T\mathbf{v}'/(\mathbf{v}^T\mathbf{v}) \tag{3.6}$$

is often used to define a correlation time (9)

$$\tau_c = \int_0^\infty \hat{\phi}(\tau) d\tau \tag{3.7}$$

which characterizes the decay rate of the velocity autocorrelation function and the time-scale of the transition from the molecular dynamic, or non-Markovian, regime where memory effects dominate to the hydrodynamic, or Markovian, regime where memory effects are negligible.

The velocity autocorrelation function is an oscillatory decreasing function of time subject to the constraint that $-1 < \phi(\tau) < 1$ where the decay rate is characterized by the correlation time. The decay of the velocity autocorrelation function to approximately zero defines the transition from the molecular dynamic region, where memory effects are significant, to the hydrodynamic region, where memory effects are negligible. These two regions are also referred to as the non-Markovian and Markovian regimes (6).

In free solution, the hydrodynamic transition has a molecular time-scale. However, in porous media such as biological tissue spins take much longer to thermalize because the length-scales of the spatial heterogeneities are typically much larger than the molecular scale. Hence, time-dependent diffusion coefficients in porous media (10,11) typically reflect not a molecular time-scale phenomenon, but rather the fact that the spin distribution has not yet fully sampled the heterogeneous environment.

The Einstein and Green-Kubo relations provide an essential connection between the diffusion tensor $\mathbf{D}$ which is a macroscopic property, and the the spin velocity $\mathbf{v}$ which is a microscopic property. The time integral and the ensemble average remove the details of the velocity distribution from the observed measurement of $\mathbf{D}$, but the diffusion tensor nevertheless captures a great deal of information about the microscopic environment. We will return to the diffusion tensor in Sec. 4.4.2.3 when we discuss the eigenstructure of the diffusion tensor.

3.2.2 Diffusion Propagator

As we will see in the later sections, the diffusion tensor framework can only describe a very limited class of diffusion phenomena. Specifically, the diffusion tensor only fully characterizes what is variously called Fickian, Case I, or Gaussian diffusion. Such diffusion excludes a vast range of phenomena which are commonly observed in *in vivo* such as restriction, heterogeneity, anomalous diffusion, and finite boundary permeability.

The diffusion propagator formalism, on the other hand, offers a far more robust descriptive framework which is capable of characterizing all of the phenomena men-

tioned above. The diffusion propagator $P(\mathbf{r}, \mathbf{r}', \tau)$ gives the probability of a spin traveling from position $\mathbf{r}'$ to $\mathbf{r}$ in the diffusion time τ (12–14). For example, if one were to release a spin at position $\mathbf{r}'$ and time 0, the propagator gives the probability of finding that spin at position $\mathbf{r}$ at time τ (15). The PDF is also referred to as the diffusion Green's function, the van Hove self-correlation function (16), or the conditional displacement probability density function (cPDF).

Given that the diffusion tensor only fully describes a very special case of diffusion, namely, pure Gaussian diffusion, the reader is encouraged, whenever possible, to think of the underlying diffusion process in terms of the propagator. Whereas the diffusion coefficient (or diffusion tensor) framework greatly simplifies experimental acquisition and interpretation, the diffusion coefficient model obscures as much as it reveals. For example, the diffusion coefficient model cannot describe heterogeneity effects, true restriction, anomalous diffusion, and a host of other phenomena. The propagator formalism, however, is naturally suited to describe these effects. The propagator framework also supports a major theme of the later chapters of this thesis which is to conceptualize diffusion not as an intrinsic property but rather as a reflection of the underlying microstructure.

3.2.3 Diffusion Equation

The relationship between the observed diffusion propagator and the underlying microstructure is ultimately governed by the diffusion equation and the attending boundary conditions. By understanding how the tissue microstructure enters into the diffusion equation and the boundary conditions we can obtain an understanding of the relationship between the observed diffusion propagator and the underlying structure. In order to derive the diffusion equation and the boundary conditions we begin by introducing the spin probability density flux $\mathbf{j}(\mathbf{r})$ which describes the flux into a unit area at position $\mathbf{r}$ and time τ. The flux is related to the spatial gradient of the diffusion propagator by Fick's first law (17, 18)

$$\mathbf{j}(\mathbf{r}) = -\mathbf{D}(\mathbf{r})\nabla P(\mathbf{r}, \mathbf{r}', \tau) \tag{3.8}$$

where the gradient is taken with respect to $\mathbf{r}$, and $\mathbf{D}(\mathbf{r})$ is the diffusion tensor at position $\mathbf{r}$. The continuity theorem

$$\frac{\partial}{\partial \tau} P(\mathbf{r}, \mathbf{r}', \tau) = -\nabla \mathbf{j}(\mathbf{r}) - \rho(\mathbf{r}) P(\mathbf{r}, \mathbf{r}', \tau) \tag{3.9}$$

states that the time rate of change of the spin displacement probability is equal to the probability lost to spin flux $\mathbf{j}$ plus the probability lost to bulk relaxation ρ. Substitution of Fick's first law (Eqn. 3.8) into the continuity theorem (Eqn. 3.9) gives the diffusion-absorption equation

$$\left[\frac{\partial}{\partial \tau} - \nabla(\mathbf{D}(\mathbf{r})\nabla) + \rho(\mathbf{r})\right] P(\mathbf{r}, \mathbf{r}', \tau) = \delta(\mathbf{r} - \mathbf{r}')\delta(\tau) \tag{3.10}$$

where the right-hand side is for a δ-function initial condition. The diffusion equation without the absorption term is sometimes referred to as Fick's second law for diffusion (17).

3.2.4 Free Diffusion

If there is no absorption ($\rho \rightarrow 0$) and no additional boundary conditions, i.e., no diffusion barriers, then the diffusion is said to be free. In such case the diffusion equation (Eqn. 3.10) is solved by the Gaussian propagator P_G

$$P_G(\mathbf{R}, \tau) = (|\mathbf{D}|(4\pi\tau)^3)^{-1/2} \exp\left(-\mathbf{R}^T\mathbf{D}^{-1}\mathbf{R}/(4\tau)\right) \tag{3.11}$$

where $\mathbf{D}$ is the diffusion tensor, $\mathbf{R} = \mathbf{r} - \mathbf{r}'$ is the relative spin displacement, and $|.|$ is the determinant. In an isotropic media with diffusion coefficient D the Gaussian propagator simplifies to

$$P_G(|\mathbf{R}|, \tau) = ((4\pi D\tau)^3)^{-1/2} \exp\left(-|\mathbf{R}|^2/(4D\tau)\right) \tag{3.12}$$

The Gaussian propagator provides a connection between the diffusion tensor and the diffusion propagator only for an unrestricted, homogeneous diffusion process. In the

following section we describe the more general case in which the propagator has no simple analytical form.

3.2.5 Restricted Diffusion

In materials with restricting, permeable, or relaxing walls the diffusion equation (3.10) is subject to additional surface boundary conditions. Writing the surface boundary conditions requires some care though. Let us label the variables on the outside of the surface with a plus sign (+) and those on the inside of the surface with a minus sign (-), bearing in mind that this is an artificial distinction. The flux from outside of the surface into the inside is labeled $\mathbf{j}_+(\mathbf{r})$ and $\mathbf{j}_-(\mathbf{r})$ for the vice versa. The flux across a given compartment is

$$\mathbf{j}_\pm(\mathbf{r}) = \left\{ -\left[\mathbf{n}(\mathbf{r})^T \mathbf{D}_\pm(\mathbf{r})\nabla + \mu_\pm(\mathbf{r})\right] P_\pm(\mathbf{r}, \mathbf{r}', \tau) \right\}_{\mathbf{r}\in\partial\Sigma} \tag{3.13}$$

where $\mathbf{n}(\mathbf{r})$ is the surface normal to the diffusion barrier at position $\mathbf{r}$, $\mu(\mathbf{r})$ is the surface relaxation at position $\mathbf{r}$, and $\partial\Omega$ is the diffusion compartment boundary (19). The spins do not accumulate at the boundary so we have the continuity condition $\mathbf{j}_+(\mathbf{r}) = \mathbf{j}_-(\mathbf{r})$.

The surface boundary condition gives the flux conditions at the surface of the diffusion compartments but does not include the effects of finite surface permeability, a condition which is commonly encountered in biological tissue since the cell membrane is partially permeable. If we assume that the diffusion barrier is thin relative to the diffusion length then the surface permeability boundary condition (20–22) can be written

$$P_+(\mathbf{r}, \mathbf{r}', \tau) - P_-(\mathbf{r}, \mathbf{r}', \tau) = -\mathcal{P}^{-1}\mathbf{j}_\pm(\mathbf{r}). \tag{3.14}$$

where $\mathcal{P}$ is the surface permeability. This boundary condition is sometimes referred to as Fick's first law of membranes. It was first used in the context of diffusion NMR by Tanner (22).[1] In the limit of impenetrable barriers ($\mathcal{P} \to 0$) the inside and outside of

[1] In recognition of Tanner's original insight, Powles (21) coined this equation, somewhat tongue-in-cheek, the leather boundary condition.

the diffusion compartments are completely isolated. Consequently, there is no surface flux $\mathbf{j}_+(\mathbf{r}) = \mathbf{j}_-(\mathbf{r}) = 0$, and P_+ and P_- are independent.

Given the diffusion equation and the surface boundary conditions it is possible to obtain analytical descriptions for the diffusion behavior in a large number of toy models. However, given the complexity of limited information available on biological media, it is often difficult to construct accurate analytical models with any predictive value. The following sections lay the framework for methods which are capable of describing properties of the tissue geometry without need for any specific realization of the tissue geometry.

3.2.6 Spectral Decomposition

The propagator has the spectral decomposition

$$P(\mathbf{r}, \mathbf{r}', \tau) = \sum_n u_n(\mathbf{r}) u_n^*(\mathbf{r}') e^{-E_n \tau} \tag{3.15}$$

where $\{u_n\}$ are the orthonormal eigenfunctions of the propagator (23, 24). The orthonormality condition can be written

$$\int u_n(\mathbf{r}) u_n^*(\mathbf{r})\, d\mathbf{r} = \delta_{mn} \tag{3.16}$$

The diffusion propagator is real and symmetric for a pure diffusion process (no coherent motion) so all of the eigenfunctions are real everywhere: $u_n^*(\mathbf{r}) = u_n(\mathbf{r})$ for all $\mathbf{r}$.

Note that from the spectral decomposition one can easily prove the Chapman-Kolmogorov theorem

$$\int P(\mathbf{r}, \mathbf{r}', \tau) P(\mathbf{r}'', \mathbf{r}, \eta)\, d\mathbf{r} = P(\mathbf{r}'', \mathbf{r}', \tau + \eta). \tag{3.17}$$

We can also use the spectral decomposition to show that all of the eigenvalues E_n are real and consequently the propagator is positive definite. Substituting the spectral decomposition into the diffusion equation gives the Helmholtz eigenvalue equation

parameterized by the eigenvalues E_n

$$[\nabla(\mathbf{D}(\mathbf{r})\nabla) + E_n]\, u_n(\mathbf{r}) = 0. \tag{3.18}$$

From the eigenvalue equation above we see that since all of the eigenfunctions are real all of the eigenvalues E_n are real as well. In the spectral decomposition the eigenvalues appear in the exponential, and hence the diffusion propagator is positive definite. The reality of the eigenvalues can be seen a physical consequence of the fact that all of the eigenmodes of the diffusion propagator decay monotonically with time. We will return to the positivity of the propagator later in Chap. 8 when we discuss the diffusion spectrum imaging method.

3.2.7 From the Ensemble-Average Propagator to Microgeometry

The observed diffusion propagator represents a spatial sum over the microscopic environments existing in the voxel, where the resolution of the voxel is defined by the macroscopic spatial encoding as allowed by the available signal-to-noise ratio. We refer to this averaged propagator as the ensemble-average propagator (EAP) defined as the propagator averaged over all initial positions

$$P(\mathbf{R}, \tau) = \int P(\mathbf{r}, \mathbf{r}', \tau) p(\mathbf{r}') dr' \tag{3.19}$$

where $R = \mathbf{r} - \mathbf{r}'$ is the relative spin displacement (13,14), and $p(\mathbf{r}')$ is the initial spin density. The EAP $P(\mathbf{R}, \tau)$ expresses the average probability of a spin displacement $\mathbf{R}$. It should be clear from the context and the notation, two position arguments for the unaveraged propagator and one for the average propagator, whether we are referring to the unaveraged or averaged propagator.

The following section describes how various microgeometric properties of the material can be derived from the EAP. Such relations are key because they allow us to infer properties of the underlying microgeometry without the need to invoke an

analytical representation of the geometry. The limiting conditions required by the models, such as equilibrium, are rarely fully realized in biological applications, but the diffusion-structure relations nevertheless provide a great deal of insight into the principles governing diffusion in complex materials.

Borrowing from the porous medium literature, we will use the terms pore space and grain space to denote, respectively, the space accessible and the space inaccessible to the spins. We realize that this distinction is somewhat ill-fitting in biological tissues which tend to consist of a complex mixture of diffusion environments separated by partially permeable barriers, but the distinction lets us describe the effects of restriction in a simple manner.

3.2.7.1 The Structure Factor from the Long-Time Limit

Given the EAP what can we infer about the underlying microgeometry of the tissue? If the diffusion boundaries are closed, unrelaxing, and completely impermeable, then in the long time Ergodic limit ($\tau \rightarrow \infty$) the propagator will assume the shape of the pore space $\chi(\mathbf{r})$, specifically,

$$P(\mathbf{r}, \mathbf{r}', \tau \rightarrow \infty) = \chi(\mathbf{r}' + \mathbf{r})p(\mathbf{r}'). \tag{3.20}$$

If we identify the initial spin density $p(\mathbf{r}')$ with the shape function $\chi(\mathbf{r}')$ then substituting the above relation into the definition of the EAP (Eqn. 3.19) shows that in the long time limit described above, the EAP will take on the shape of the average spatial autocorrelation of the pore shape, (14, 25)

$$\begin{aligned} P(\mathbf{R}, \tau \rightarrow \infty) &= \sum_{\text{pores}} \int \chi(\mathbf{r} + \mathbf{r}')\chi(\mathbf{r}')d\mathbf{r}' \\ &= \mathcal{F}^{-1}\left[\sum_{\text{pores}} |\mathcal{F}[\chi(\mathbf{q})]|^2\right] \end{aligned} \tag{3.21}$$

where $\mathcal{F}$ is the Fourier transform, and the sum is taken over the isolated pores. This striking result allows for direct inference of the average structure function from the

EAP. However, it should be borne in mind that in biological applications the full equilibrium condition is rarely satisfied due to the finite permeability of cell membranes, surface relaxation, and the high connectivity of the pore space.

3.2.7.2 The Return-to-Origin Probability and the Spectral Sum

The return-to-origin (RTO) probability $\Theta(\tau)$ expresses the average probability that a molecule will return to its starting position (26, 27). The RTO probabilty can be derived from the propagator as follows

$$\Theta(\tau) = \int P(\mathbf{r}', \mathbf{r}', \tau) p(\mathbf{r}') d\mathbf{r}'. \tag{3.22}$$

Substituting the eigenmode expansion for the diffusion propagator we have

$$\Theta(\tau) = \sum_n \int u_n(\mathbf{r}') u_n^*(\mathbf{r}') e^{-E_n \tau} d\mathbf{r}' \tag{3.23}$$

$$= \sum_n e^{-E_n \tau} \tag{3.24}$$

where the last equation follows from the fact that the eigenfunctions form an orthonormal set.

Eqn. 3.24 is referred to as the spectral sum or the spectral partition function and is extensively studied in the field of inverse spectral analysis. Inverse spectral analysis is concerned with the inference of the geometry of a domain from the eigenspectrum of an operator on that domain, also known as the classic problem "Can one hear the shape of a drum?" (28). Building on work from Sleeman and Zayed (29), Mitra (27) showed that the spectral sum is related to the surface-to-volume ratio of the pore interface

$$\Theta(\tau) = \frac{V_p}{(4\pi D_0 \tau)^{3/2}} \left[1 + \frac{\sqrt{\pi}}{2} \frac{S_p}{V_p} \sqrt{D_0 \tau} - \left[\frac{1}{3} \left\langle \frac{1}{R_1} + \frac{1}{R_2} \right\rangle + \frac{\mu}{D_0} \right] \frac{S_p}{V_p} D_0 \tau + \mathcal{O}(\tau^{3/2}) \right] \tag{3.25}$$

where S_p is the surface area of the pore interface, V_p is the volume of the space excluded to diffusion (the grain space), D_0 is the free diffusion coefficient, R_1 and R_2 are the local principal radii of curvature of the pore interface, and $\langle ... \rangle$ is the average over the interface. The above relationship can also be defined in terms of the time-dependent diffusion coefficient (23, 30)

$$D(\tau)/D_0 = 1 - \frac{4}{9\sqrt{\pi}} \frac{S}{V_p} \sqrt{D_0 \tau} + \mathcal{O}(D_0 \tau). \tag{3.26}$$

This expression was experimentally validated by Latour (31) and has been used, either in this form or in a variation thereof, to directly measure the surface-to-volume ratio in a variety of materials (26, 31–33).

3.3 Discussion

In this chapter, we showed how the diffusion tensor is related to the underlying velocity distribution of the spins. This provided an essential connection between the molecular hydrodynamics of the spins and the macroscopic diffusion tensor. The diffusion propagator formalism was introduced and we showed how the propagator is governed by the diffusion equation.

We stated that in the case of free diffusion the diffusion equation is solved by a Gaussian propagator. This seems to present a contradiction however because where could diffusion anisotropy come from if not restriction. The paradox can be resolved by noting that the Gaussian model can also be seen as arising from a low spatial frequency approximation to the diffusion propagator. Considering the isotropic case for notational simplicity, the Fourier transform $F(k, \tau)$ of the propagator has a cumulant expansion (34)

$$\log\left(\frac{F(k,\tau)}{F(0,\tau)}\right) = \sum_{n>0} \frac{\langle (ikR)^n \rangle_c}{(n)!} \tag{3.27}$$

where the cumulant averages are defined as (35)

$$\begin{aligned} \langle R\rangle_c &= \langle R\rangle \\ \langle R^2\rangle_c &= \langle R^2\rangle - \langle R\rangle^2 \\ \langle R^3\rangle_c &= \langle R^3\rangle - 3\langle R^2\rangle\langle R\rangle + 2\langle R\rangle^3 \\ \langle R^4\rangle_c &= \langle R^4\rangle - 4\langle R^3\rangle\langle R\rangle - 3\langle R^2\rangle^2 + 12\langle R^2\rangle\langle R\rangle^2 - 6\langle R\rangle^4 \end{aligned} \tag{3.28}$$

The odd terms which arise from flux asymmetry vanish on averaging for a pure diffusion process. The cumulant expansion truncates with the quadratic term in the case of free diffusion since the higher order cumulants vanish for a Gaussian distribution. Retaining only the first cumulant level leads to the Gaussian diffusion function. Hence, the Gaussian function can be viewed as arising from either free diffusion or a low spatial frequency approximation to a restricted propagator. In Chaps. 8 and 10, we will explore the structure of the propagator in the high spatial frequency regime where the Gaussian model is no longer valid.

In the following chapter, we discuss how the various functions which we introduced in this chapter, such as the diffusion tensor and the EAP, can be measured with NMR and incorporated into an imaging paradigm.

3.4 References

[1] A. Einstein. Über die von der molekularkinetischen Theorie der Wärme geforderte Bewegung von in ruhenden Flüssigkeiten suspendierten Teilchen. *Ann. Physik.*, 4:549–560, 1905. (English translation in Ref. 36).

[2] L. Onsager. Electric moments of molecules in liquids. *J. Amer. Chem. Soc.*, 58:1486–1493, 1936.

[3] L.D. Landau and E.M. Lifschitz, editors. *Statistical Physics.* Butterworth-Heinemann, 1999.

[4] R.K. Pathria, editor. *Statistical Mechanics.* Butterworth-Heinemann, 1996.

[5] N.H. March and M.P. Tosi. *Atomic Dynamics in Liquids.* Dover Publications, New York, 1976.

[6] J.P. Boon and S. Yip. *Molecular hydrodynamics.* McGraw-Hill, New York, 1980.

[7] M.S. Green. Markoff random process and the statistical mechanics of time dependent phenomena. II. Irreversible processes in fluids. *J. Chem. Phys.*, 22:398–412, 1954.

[8] R. Kubo. Statistical-mechanical theory of irreversible processes. I. General theory and simple applications to magnetic and conduction problems. *J. Phys. Soc. Japan*, 12:570–586, 1957.

[9] D.A. McQuarrie, editor. *Statistical Mechanics.* Harper and Row, New York, 1976.

[10] K.G. Helmer, B.J. Dardzinski, and C.H. Sotak. The application of porous-media theory to the investigation of time-dependent diffusion in in vivo systems. *NMR Biomed.*, 8:297–306, 1995.

[11] L.L. Latour, K. Svoboda, P.P. Mitra, and C.H. Sotak. Time-dependent diffusion of water in a biological model system. *Proc. Natl. Acad. Sci. USA*, 15:1229–1233, 1994.

[12] K.J. Packer and C. Rees. Pulsed NMR studies of restricted diffusion I. Droplet size distributions in emulsions. *J. Colloid. Interface Sci.*, 40:206–217, 1972.

[13] J. Kärger and W. Heink. The propagator representation of molecular transport in microporous crystallites. *J. Magn. Reson.*, 51:1–7, 1983.

[14] P.T. Callaghan. *Principles of nuclear magnetic resonance microscopy.* Oxford, Great Britain, 1993.

[15] E.O. Stejskal. Use of spin echoesd in a pulsed magnetic-field gradient to study anisotropic, restricted diffusion and flow. *J. Chem. Phys.*, 43:3597–3603, 1965.

[16] L. Van Hove. Correlation is space and time and Born approximation scattering in systems of interacting particles. *Phys. Rev.*, 95:249–252, 1954.

[17] A. Fick. On liquid diffusion. *Philos. Mag.*, 10:30–39, 1855.

[18] A. Einstein. Elementare Theorie der Brownschen Bewegung. *Z. Electrochemie angewandte Physik. Chemie*, 14:235–239, 1908. (English translation in Ref. 36).

[19] K.R. Brownstein and C.E. Tarr. Importance of classical diffusion in NMR studies of water in biological cells. *Phys. Rev. A*, 19:2446–2453, 1979.

[20] T.F. Weiss. *Cellular biophysics.* MIT Press, Cambridge, Massachusetts, 1996.

[21] J.G. Powles, M.J.D. Mallett, G. Rickayzen, and W.A.B. Evans. Exact analytic solutions of diffusion impeded by an infinite array of partially permeable barriers. *Proc. R. Soc. Lond. A*, 436:391–403, 1992.

[22] J.E. Tanner. Transient diffusion in a system partitioned by permeable barriers. Application to NMR measurements with a pulsed field gradient. *J. Chem. Phys.*, 69:1748–1754, 1978.

[23] P.P. Mitra, P.N. Sen, L.M. Schwartz, and P.L. Doussal. Diffusion propagator as probe of the structure of porous media. *Phys. Rev. Lett.*, 68:3555–3558, 1992.

[24] R.F. Bass and K. Burdzy. Eigenvalue expansions for Brownian motion with an application to occupation times. *Electr. J. Prob.*, 1:1–19, 1996.

[25] D.G. Cory and A.N. Garroway. Measurement of translational displacement probabilities by NMR: an indicator of compartmentation. *Magn. Reson. Med.*, 14:435–444, 1990.

[26] M.D. Hürlimann and L.M. Schwartz amd P.N. Sen. Probability of return to origin at short times: a probe of microstructure in porous media. *Phys. Rev. B*, 51:14936–14940, 1995.

[27] P.P. Mitra, L.L. Latour, R.L. Kleinberg, and C.H. Sotak. Pulsed-field gradient NMR measurements of restricted diffusion and the return-to-origin probability. *J. Magn. Reson. A*, 114:47–58, 1995.

[28] M. Kac. Can one hear the shape of a drum? *Am. Math. Monthly*, 73:1–7, 1966.

[29] B.D. Sleeman and E.M.E. Zayed. *J. Math Anal. Appl.*, 94:78–, 1983.

[30] P.P. Mitra, P.N. Sen, and L.M. Schwartz. Short-time behavior of the diffusion coefficient as a geometrical probe of porous media. *Phys. Rev. B*, 47:8565–8574, 1993.

[31] L.L. Latour, P.P. Mitra, R.L. Kleinberg, and C.H. Sotak. Time-dependent diffusion coefficient of fluids in porous media as a probe of surface-to-volume ratio. *J. Magn. Reson. A*, 101:342–346, 1993.

[32] R.W. Mair, M.D. Hürlimann, P.N. Sen, L.M. Schwartz, S. Patz, and R.L. Walsworth. Tortuosity measurement and the effects of finite pulse widths on xenon gas diffusion NMR studies of porous media. *Magn. Reson. Imag.*, 19:345–351, 2001.

[33] K.G. Helmer, M.D. Hürlimann, T.M. De Swiet, P.N. Sen, and C.H. Sotak. Determination of ratio of surface area to pore volume from restricted diffusion in a constant field gradient. *J. Magn. Reson. A*, 115:257–259, 1995.

[34] P.P. Mitra and P.N. Sen. Effects of microgeometry and surface relaxation on NMR pulsed-field-gradient experiments: simple pore geometries. *Phys. Rev. B*, 45:143–156, 1992.

[35] J. Stepišnik. Validity limits of gaussian approximation in cumulant expansion for diffusion attenuation of spin echo. *Physica B*, 270:110–117, 1999.

[36] A. Einstein. In R. Furthe and A.D. Cowper, editors, *Investigations on the theory of Brownian motion.* Dover, New York, 1956. (Collection of papers translated from the German).

Chapter 4

Principles of Diffusion NMR and MRI

If water is too clear, it will not contain fish.

Chinese Proverb

4.1 Introduction

In this chapter we describe how the diffusion phenomena which we introduced in the previous chapter can be measured and imaged with, respectively, diffusion NMR and MRI. We begin with the classical Bloch-Torrey equation for molecular diffusion and then introduce the pulsed gradient spin echo experiment which enables quantitative diffusion measurements. Upon introducing the basic methodology we derive the key Fourier reciprocal relationship between the spin echo magnitude and the ensemble-average diffusion propagator. Lastly, we discuss how these techniques are applied to generate diffusion-weighted and diffusion tensor images.

4.2 Diffusion NMR

4.2.1 The Bloch-Torrey Equations

The Bloch equations provide a valuable framework for describing many phenomena in NMR (1). In the rotating frame and in the absence of any radiofrequency (rf) field the Bloch equations can be written

$$\frac{\partial}{\partial t} m_+ = -i\gamma \mathbf{r}(t)^T \mathbf{g}(t) - m_+/T_2 \tag{4.1}$$

where $m_+ = m_x + im_y$ is the complex magnetization vector, γ is the gyromagnetic ratio, $\mathbf{r}(t)$ is the spin position as a function of time t, $\mathbf{g}(t) = |\nabla \mathbf{B}(t)|$ is the applied magnetic field gradient, $T_2 = 1/\rho$ is the spin-spin relaxation time, and ρ is the bulk relaxation rate. The Bloch equations were modified by Torrey to include the effects of molecular diffusion and flow to give the Bloch-Torrey equation (2)

$$\frac{\partial}{\partial t} m_+ = -i\gamma \mathbf{r}(t)^T \mathbf{g}(t) - m_+/T_2 + \nabla(\mathbf{D}(\mathbf{r})\nabla m_+) - \nabla \mathbf{v} m_+ \tag{4.2}$$

where $\mathbf{D}$ is the diffusion tensor which we encountered in the previous chapter and $\mathbf{v}$ is the flow vector. The following derivation essentially follows the treatments given by Refs. 3 and 4.

The Bloch-Torrey equation can be solved by making the substitution (5)

$$\begin{aligned} m_+(\mathbf{r}, t) &= \exp(i\langle\varphi(t)\rangle)\exp(-\alpha(t)) && (4.3)\\ &= \exp\left[-i\gamma \int_0^t \mathbf{r}(t')^T \mathbf{g}(t')\, dt'\right] \exp(-\alpha(t)) && (4.4)\\ &= \exp\left[-i\gamma \int_0^t \mathbf{r}(t')^T \mathbf{g}(t')\, dt'\right] A(t)\exp(-t/T_2) && (4.5) \end{aligned}$$

where

$$\varphi(t) = \gamma \int_0^t \mathbf{r}(t')^T \mathbf{g}(t')\, dt' \tag{4.6}$$

is the spin phase as a function of time, and $\langle . \rangle$ denotes the ensemble average. In order to produce an echo at the echo time $t = \mathrm{TE}$ we have the condition that $\int_0^{\mathrm{TE}} \mathbf{g}(t)\, dt =$

0. Consequently, at the echo center we have $m_+(\mathbf{r}, \mathrm{TE}) = A(\mathrm{TE})\exp(-\mathrm{TE}/T_2)$.

Let us define an 'effective gradient' $\mathbf{g}^*(t)$ which incorporates the phase inversions from the rf pulses. Substituting Eqn. 4.3 into the Bloch-Torrey equation gives

$$\frac{\partial}{\partial t}A(t) = \gamma^2 \left(\int_0^t \mathbf{g}^*(t')\, dt'\right)^T \mathbf{D} \left(\int_0^t \mathbf{g}^*(t')\, dt'\right) A(t). \tag{4.7}$$

Defining the matrix

$$\mathbf{B}(t) = \gamma^2 \left(\int_0^t \mathbf{g}^*(t')\, dt'\right) \left(\int_0^t \mathbf{g}^*(t')\, dt'\right)^T, \tag{4.8}$$

which is referred to as the B-matrix (4), leads to the simple relationship

$$\frac{\partial}{\partial t}A(t) = \mathrm{Tr}(\mathbf{B}(t)\mathbf{D})A(t). \tag{4.9}$$

where Tr(.) is the matrix trace. We will return to the B-matrix in more detail when we discuss the diffusion tensor imaging method in Sec. 4.4.2. Solving for $A(t)$ gives (6)

$$A(t) = \exp\left[-\int_0^t \mathrm{Tr}(\mathbf{B}(t')\mathbf{D})\, dt'\right] \exp\left[i\gamma \int_0^t \int_0^{t'} \mathbf{v}^T(t'')\mathbf{g}(t'')\, dt''\, dt'\right]. \tag{4.10}$$

The above equation can be used to calculate the attenuation due to Gaussian diffusion and coherent flow for any gradient profile $\mathbf{g}^*(t)$. The following section describes the pulsed gradient spin echo sequence which allows for direct, quantitative measurement of the diffusion coefficient.

4.2.2 Pulsed Gradient Spin Echo Experiment

The pulsed gradient spin echo (PGSE) experiment pioneered by Stejskal and Tanner (5) is the classical method for measuring diffusion with NMR. The general idea of the PGSE experiment is to excite the spin system with a $\pi/2$-pulse, encode the spin position with a time-constant magnetic field gradient of duration δ, invert the spin

phase with a π-pulse, apply a second magnetic field gradient with equal intensity and duration to the previous gradient and at a time Δ after the first gradient pulse, and then acquire the echo at time TE (Fig. 4-1).

If a given spin moves, say, by diffusion, between the time of the first and second gradients then the phase of the spin will not return to its original orientation. Due to the increased disorder of the spin phase distribution the spin echo signal, which is proportional to the mean phase difference, will be smaller relative to the case in which there was no gradient. Hence, the decrease in the spin echo magnitude will reflect the amount of diffusion which occurred between the two diffusion gradient pulses (Fig. 4-2).

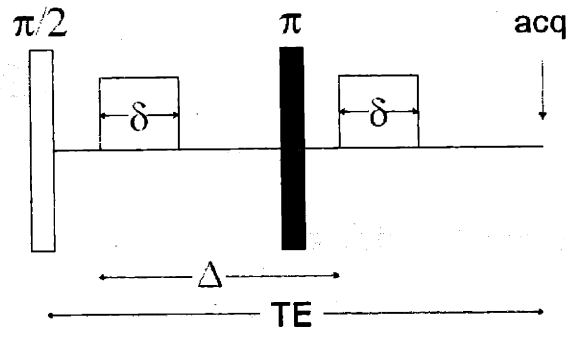

Figure 4-1: Pulse diagram for the PGSE experiment.

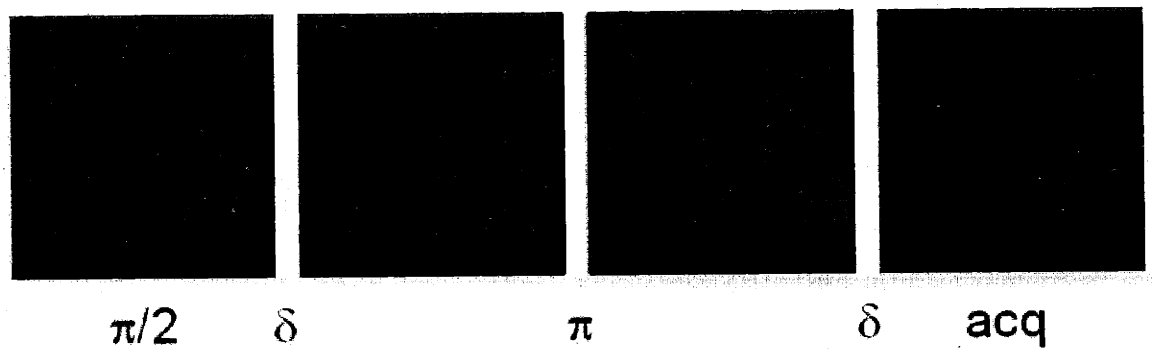

Figure 4-2: Schematic diagram of the spin phase distribution during the PGSE experiment depicted shown in Fig. 4-1. The *pi*/-pulse excites the spin spin system. The diffusion gradient imparts a phase to the spins proportional to their location along the gradient. The π-pulse inverts the spin phases. A second diffusion gradient pulse is applied at time Δ after the first gradient and the echo is acquired at time TE.

4.2.2.1 The Stejskal-Tanner Equation

The spin echo attenuation for the PGSE experiment can be calculated using Eqn. 4.10 from the previous section. The effective gradient for the PGSE sequence is (5)

$$\mathbf{g}^*(t) = -\theta(t) + \theta(t-\delta) + \theta(t-\Delta) - \theta(t-\Delta-\delta) \tag{4.11}$$

where $\theta(t) = \delta(t \geq 0)$ is the Heaviside step function. Substitution of this effective gradient into Eqn. 4.10 gives

$$m_+ = \exp(-\gamma^2\delta^2\mathbf{g}^T\mathbf{D}\mathbf{g}(\Delta - \delta/3)) \exp(-\gamma\delta\Delta\mathbf{g}^T\mathbf{v}) \exp(-\mathrm{TE}/T_2) \tag{4.12}$$

which is the famous Stejskal-Tanner relation (5). The time constant $\tau = \Delta - \delta/3$ defines an effective diffusion time where the $\delta/3$ correction is due to the diffusion which occurs during the time in which the gradients are on.

4.2.2.2 The Fourier Relationship

The Stejskal-Tanner equation allows us to relate the observed diffusion signal to the underlying diffusion coefficient or diffusion tensor assuming that the diffusion is purely Gaussian. The Gaussianity assumption can be easily violated however if the sample contains any restriction, due for example to finitely permeable walls, surface relaxation, or diffusion compartment heterogeneity. While biological diffusion imaging studies commonly assume that the diffusion is Gaussian there is a body of experimental evidence which indicates that this assumption is not valid, principally due to the reasons cited above.[1]

The present section describes a broader interpretive framework which allows us to measure the ensemble-average diffusion propagator (EAP) (3.2.7) from a series of

[1]The prevalance of the Gaussianity assumption in biological diffusion imaging, depsite strong evidence to the contrary, is analogous to the ubiquity of the normal distribution of errors in statistics. As Lippmann stated, "Everybody believes in the exponential law of errors: the experimenters, because they think it can be proved by mathematics; and the mathematicians, because they believe it has been established by observation" (7). These words could equally well apply to the situation in diffusion imaging.

PGSE experiments independent of any assumptions on the form of the underlying diffusion process. The PGSE signal E is simply a superposition of the transverse magnetizations, each with a phase φ

$$E = E_0\langle e^{i\varphi}\rangle \tag{4.13}$$

where $E_0 = E(0,\tau)$ is the spin echo signal in the absence of any applied gradient, $\langle ...\rangle$ denotes the ensemble average, and φ is the spin phase. The ensemble average of any general function $f(\varphi)$ of the phase φ can be written explicitly in terms of the phase probability distribution

$$\langle f(\varphi)\rangle = \int f(\varphi)\, dP(\varphi) = \int f(\varphi)P(\varphi)\, d\varphi \tag{4.14}$$

where $P(\varphi)$ is the probability of a spin phase φ. In the limit of infinitely narrow pulses the effective gradient (Eqn. 4.11) from the Stejskal Tanner experiment is

$$\mathbf{g}^*(t) = \mathbf{g}(\delta(0) - \delta(\Delta)) \tag{4.15}$$

where $\mathbf{g}$ is independent of time. The spin phase φ given by Eqn. 4.6 is then

$$\begin{aligned} \varphi &= \gamma\delta\mathbf{g}^T(\mathbf{r}(0) - \mathbf{r}(\Delta)) && (4.16)\\ &= \gamma\delta\mathbf{g}^T(\mathbf{r}' - \mathbf{r}) && (4.17)\\ &= \gamma\delta\mathbf{g}^T\mathbf{R} && (4.18) \end{aligned}$$

where $\mathbf{r}'$ is the spin position at the time of the first gradient, $\mathbf{r}$ is the spin position at the time of the second gradient, Δ is the time between the two gradients, and $\mathbf{R} = \mathbf{r}' - \mathbf{r}$ is the relative spin displacement. It is convenient to define the displacement reciprocal vector $\mathbf{q} = \gamma\delta\mathbf{g}$ so that we have simply $\varphi = \mathbf{q}^T\mathbf{R}$. As we will see in the following section the reciprocal vector $\mathbf{q}$ plays the important role of the Fourier reciprocal vector to the relative spin displacement vector $\mathbf{R}$.

The narrow pulse condition requires that the diffusion length associated with the

diffusion gradient duration (see Chap. 3) be considerably less than the pore size of the medium (8). For example, the diffusion mixing length of water at room temperature is approximately 1μm in 1ms. Hence, in order to satisfy the narrow pulse condition for a 1μm pore, the diffusion gradient cannot be longer than 1ms. In Chap. 8 we will look at diffusion NMR outside of the narrow pulse regime.

Owing to the linearity of the Larmor relation, the probability of a phase difference φ is proportional to the probability of a spin displacement $\mathbf{R}$. Hence,

$$P(\varphi, \tau) = P(\mathbf{R}, \tau). \tag{4.19}$$

Eqn. 4.13 can then be written (3, 9)

$$\begin{aligned} E(\mathbf{q}, \tau) &= E_0 \int P(\mathbf{R}, \tau) e^{i\mathbf{q}^T\mathbf{R}} \, d\mathbf{R} && (4.20) \\ &= E_0 \mathcal{F}[P(\mathbf{R}, \tau)] && (4.21) \end{aligned}$$

where $P(\mathbf{R}, \tau)$ is the ensemble-average diffusion propagator (EAP) (10) which we introduced in Sec. 3.2.7, and $\mathcal{F}$ is the Fourier transform with respect to the relative spin displacement vector $\mathbf{R}$. By expanding $\mathbf{R} = \mathbf{r}' - \mathbf{r}$, the above equation can also be written in terms of the absolute spin positions as

$$E(\mathbf{q}, \tau) = E_0 \int P(\mathbf{r}', \mathbf{r}, \tau) p(\mathbf{r}) e^{i\mathbf{q}^T(\mathbf{r}-\mathbf{r}')} d\mathbf{r}' \, d\mathbf{r} \tag{4.22}$$

where $P(\mathbf{r}', \mathbf{r}, \tau)$ is the diffusion propagator (3.2.2) and $p(\mathbf{r})$ is the initial spin density.

Eqn. 4.20 clearly illustrates the Fourier reciprocal relationship between the PGSE signal and the EAP (3). This relationship is key and forms the basis of all diffusion imaging experiments. In particular, the Fourier relationship allows for direct reconstruction of the EAP by inverse Fourier transform of the spin echo signal

$$\begin{aligned} P(\mathbf{R}, \tau) &= E_0^{-1} \int E(\mathbf{q}, \tau) e^{-i\mathbf{q}^T\mathbf{R}} \, d\mathbf{q} && (4.23) \\ &= E_0^{-1} \mathcal{F}^{-1}[E(\mathbf{q}, \tau)] \end{aligned}$$

where the inverse Fourier transform $\mathcal{F}^{-1}$ is taken with respect to the reciprocal vector $\mathbf{q}$. Reconstruction of the EAP by inverse Fourier transform of the spin echo signal forms the basis of what is variously called q-space or diffusion displacement imaging (3).

4.3 Relation to Microgeometry

In Sec. 3.2.7 we showed how the EAP is related to a variety of microstructural features. Here, we recast those relations in terms of the PGSE signal.

4.3.1 The Pore Autocorrelation from the Long Time Limit

Substitution of the spectral decomposition (3.15) into the Fourier relation (Eqn. 4.22) gives

$$E(\mathbf{q},\tau) = E_0 \sum_n |\mathcal{F}[u_n(\mathbf{r})]|^2 e^{-E_n \tau}. \tag{4.24}$$

The above equation illustrates that for a pure diffusion process the spin echo signal is positive everywhere. This is a direct consequence of the positive-definiteness of the diffusion propagator.

The positive definiteness of the diffusion propagator, and consequently the positivity of the spin echo signal, can be seen as a physical consequence of the fact that all the diffusion eigenmodes decay monotonically with time. Note for the propagator to be positive definite, it is not sufficient that the propagator simply be monotonically decreasing radially. For example, the functions of the form $P(R) = a\exp(-b|R|^n)$, which are all monotonically decreasing with $|R|$, only have a positive Fourier transform for $n \leq 2$, and only have a Fourier transform which is finite at the origin for $n > 1$.

It is important to note that the positivity and reality of the echo signal only holds for the *ensemble-average* diffusion function and not the unaveraged diffusion function. For example, let us consider the simple case of a one-dimensional compartment with impermeable walls. At long times, the diffusion function is a boxcar, the Fourier

transform of which is a sinc function which is not positive everywhere. However, if we consider the average over all starting positions the diffusion function is a triangle, the auto-correlation of the boxcar, the Fourier transform of which is the sinc-squared function which is positive everywhere. Hence, the averaging of the diffusion signal over the voxel is required to ensure that the echo signal is positive. We will exploit this result in Chaps. 8 and 10 when we discuss the diffusion spectrum imaging and q-ball imaging methods.

If the diffusion function is fully evolved then in the long-time Ergodic limit all of the eigenvalues E_n are zero and the spin echo signal is

$$E(\mathbf{q}, \tau \rightarrow \infty) = E_0 \sum_n |\mathcal{F}[u_n(\mathbf{r})]|^2 \quad (4.25)$$

$$= \sum_{\text{pores}} |\mathcal{F}[\chi(\mathbf{r})]|^2 \quad (4.26)$$

$$= \sum_{\text{pores}} |S(\mathbf{q})|^2 \quad (4.27)$$

where S is called the structure factor of a pore. This equation provides the powerful results that in the fully evolved limit the spin echo signal is the average power spectrum of the pore shape (3).

4.3.2 The Return-To-Origin Probability and the Spectral Sum

The return-to-origin probability (Sec. 3.2.7.2) is simply the total integral of the spin echo signal over reciprocal space (11):

$$\Theta(\tau) = (2\pi)^{-3} \int E(\mathbf{q}, \tau)\, d\mathbf{q} \quad (4.28)$$

. The above relation allows us to directly measure the spectral sum without the need to take the Fourier transform of the experimental spin echo data.

4.3.3 Free Diffusion

We saw in Sec. 4.2.2.1 that for free, anisotropic diffusion the spin echo signal is simply

$$E(\mathbf{q},\tau) = E_0 e^{-\mathrm{Tr}(\mathbf{BD})} \tag{4.29}$$

where $\mathbf{D}$ is the diffusion tensor. For isotropic diffusion the Stejskal-Tanner relation trivially simplifies to

$$E(q,\tau) = E_0 e^{-bD} \tag{4.30}$$

Le Bihan (12) coined the term b-value for the scalar quantity $b = \gamma^2\delta^2 g^2(\Delta - \delta/3) = q^2(\Delta - \delta/3)$. Eqns. 4.29 and 4.30 form the basis of, respectively, the diffusion-weighted and diffusion tensor imaging experiments which we discuss in the next sections.

4.4 Diffusion MRI

4.4.1 Diffusion-Weighted Imaging

The scalar Stejskal-Tanner relation (Eqn. 4.30) contains two unknowns, namely, the unattenuated echo signal E_0 and the diffusion coefficient D. Hence, the diffusion coefficient can be quantitatively estimated from at least two measurements of the signal each with different b-value magnitudes. If we take the natural log of the spin echo signal then the diffusion coefficient can be obtained from a set of diffusion experiments by standard linear regression methods. Diffusion-weighted imaging cannot however describe the anisotropic Gaussian diffusion which is observed in fibrous biological tissues. In such cases the DTI experiment is called for.

4.4.2 Diffusion Tensor Imaging

4.4.2.1 Background

Biological tissues with regularly ordered microstructure such as skeletal muscle, spine, tongue, heart, the eye lens, and cerebral white matter exhibit anisotropic water dif-

fusion when measured by diffusion NMR or MRI (4, 13–18). In the previous chapter we described how in such anistropic materials the diffusion function can be described by the anistropic Gaussian (Eqn.3.11). The anisotropic Gaussian is parameterized by a diffusion tensor $\mathbf{D}$, the eigensystem of which reflects the orientational structure of the underlying material.

The diffusion tensor can be measured with a technique called called magnetic resonance diffusion tensor imaging (DTI) (4) which measures the apparent water self-diffusion tensor under the assumption of Gaussian diffusion (see Chap. 3). Based on the eigenstructure of the measured diffusion tensor it is possible to infer the orientation of the diffusion compartments within the voxel so that, for example, the major eigenvector of the diffusion tensor parallels the mean fiber orientation (4), and the minor eigenvector the normal to the mean plane of fiber dispersion (19). The present section describes how the diffusion tensor can be quantitatively reconstructed from a set of PGSE acquisitions and how the diffusion tensor can be analyzed in terms of its eigensystem.

4.4.2.2 Diffusion Tensor Reconstruction

To begin, the diffusion tensor is a three-dimensional, symmetric rank-2 tensor and therefore has 6 unique coefficients: the 3 diagonal elements and the 3 off-diagonal elements of the tensor. Consequently, at least 7 image acquisitions are required to reconstruct the diffusion tensor: 6 to obtain the 6 unique tensor elements and 1 to estimate the unattenuated signal magnitude E_0. The tensor reconstruction can be formulated as a linear inversion problem (20) as follows.

Due to the symmetry of the diffusion tensor, the diffusion tensor contains 6 unique elements: the 3 diagonal and the 3 off-diagonal elements. Let us denote these elements as $\mathbf{d} = \{d_i\}$ where $i \in [1, 6]$. These elements are assigned to the diffusion tensor coefficients according to $d_1 = D_{xx}$, $d_2 = D_{xy} = D_{yx}$, $d_3 = D_{xz} = D_{zx}$, $d_4 = D_{yy}$, $d_5 = D_{yz} = D_{zy}$, and $d_6 = D_{zz}$. For a set of n experiments obtained with $\mathbf{q}^i$, $i \in [1, n]$

we can define the $n \times 7$ B-matrix (20)

$$\mathbf{B} = \begin{pmatrix} q_1^1 q_1^1 & 2q_1^1 q_2^1 & 2q_1^1 q_3^1 & q_2^1 q_2^1 & 2q_2^1 q_3^1 & q_3^1 q_3^1 & 1 \\ q_1^2 q_1^2 & 2q_1^2 q_2^2 & 2q_1^2 q_3^2 & q_2^2 q_2^2 & 2q_2^2 q_3^2 & q_3^2 q_3^2 & 1 \\ & & & \vdots & & & \\ q_1^n q_1^n & 2q_1^n q_2^n & 2q_1^n q_3^n & q_2^n q_2^n & 2q_2^n q_3^n & q_3^n q_3^n & 1 \end{pmatrix} \tau \tag{4.31}$$

where $\tau = \Delta - \delta/3$ is the effective diffusion time. Note that n needs to be at least 7 in order to obtain a sufficiently determined reconstruction. The condition number of the B-matrix defines the stability of the reconstruction.

Let us define the set of measured spin echo signals in terms of the measurement vector $\mathbf{s} = \{E(\mathbf{q}^i, \tau)\}$. Taking the natural logarithm of both sides of Eqn. 4.29 then gives the simple relation $-\log(\mathbf{s}) = \mathbf{B}(\mathbf{d}^T - \log E_0)^T$. The Gaussian noise-model maximum likelihood estimate (MLE) for the diffusion tensor is then (20)

$$\mathbf{D} = -\mathcal{P}[(\mathbf{B}^T \boldsymbol{\Sigma}^{-1} \mathbf{B})^{-1} \mathbf{B}^T \boldsymbol{\Sigma}^{-1} \log(\mathbf{s})] \tag{4.32}$$

where the partition operation $\mathcal{P}$ is defined as

$$\mathcal{P}[\mathbf{d}] = \begin{pmatrix} d_1 & d_2 & d_3 \\ d_2 & d_4 & d_5 \\ d_3 & d_5 & d_6 \end{pmatrix} \tag{4.33}$$

and $\boldsymbol{\Sigma}$ is the noise covariance matrix associated with $\log(\mathbf{s})$. Fig. 4-3 shows a diffusion tensor image of frontal white matter obtained with the Gaussian MLE. Note that in practice the noise is Rayleigh distributed and not Gaussian distributed. Consequently, the Gaussian MLE will be biased if high q-values are used because the Rayleigh and Gaussian distributions differ significantly at the tails.

4.4.2.3 Diffusion Tensor Eigensystem

Here, we discuss the eigensystem of the diffusion tensor and the structural information which can be gleaned therefrom. The diffusion tensor can be decomposed into the

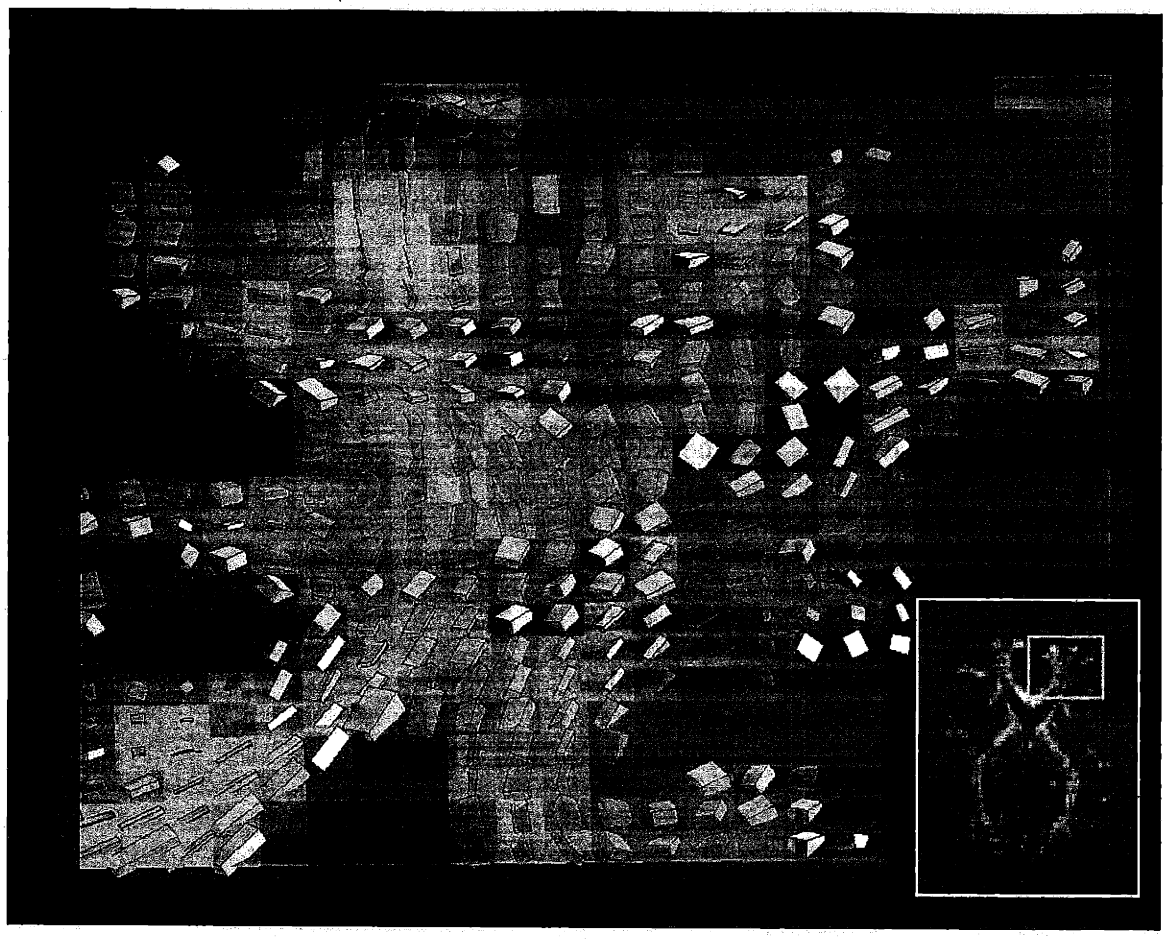

Figure 4-3: Diffusion tensor image of frontal white matter reconstructed from the Gaussian MLE. The cuboids depict the local diffusion tensor within each voxel. The axes of each cuboid are oriented in the direction of the tensor eigenvectors and are scaled by the corresponding eigenvalue. This visualization scheme is discussed in more detail in Sec. 4.4.2.3. The cuboids are also colored according to the direction of the major eigenvector with red indicating mediolateral, green anteroposterior, and blue superoinferior. The display of the cuboids was thresholded according to the FA metric in order to highlight the white matter anatomy. (21)

eigensystem

$$\mathbf{D} = \mathbf{R}\mathbf{\Lambda}\mathbf{R}^T \tag{4.34}$$

where $\mathbf{R} = (\mathbf{e}_1\ \mathbf{e}_2\ \mathbf{e}_3)$ is a column matrix of the orthonormal diffusion tensor eigenvectors $\mathbf{e}_\nu$, and $\mathbf{\Lambda} = \mathbf{diag}(\lambda_1\ \lambda_2\ \lambda_3)$ is a diagonal matrix of the diffusion tensor eigenvalues $\{\lambda_\nu\}$. The eigenvectors $\mathbf{e}_1, \mathbf{e}_2, \mathbf{e}_3$ are often refereed to, respectively, as the major, medium, and minor eigenvectors.

The diffusion tensor eigensystem can be conceptualized in terms of the diffusion isoprobability surface which represents the surface on which a spin at the origin will diffuse to with equal probability. For a Gaussian diffusion process the isoprobability surface is a three-dimensional ellipsoid. The isoprobability ellipsoid represents the surface on which the Gaussian diffusion function has a constant value, i.e., $\mathbf{x}^T\mathbf{D}\mathbf{x} = \text{const}$.

The axes of the isoprobability ellipsoid are oriented in the direction of the tensor eigenvectors and have lengths proportional to the diffusion distance along the corresponding eigenvectors (Fig. 4-4). Since the diffusion distance is proportional to the square root of the diffusion eigenvalues this is equivalent to scaling by the square root of the diffusion tensor eigenvalues. Note that in biomedical applications it is conventional to scale the ellipsoid axes not by the diffusion distance (which is proportional to the square-root of the diffusion tensor eigenvalues) but by the diffusion distance squared (which is proportional to the eigenvalues themselves). Scaling by the diffusion distance squared enhances the visual anisotropy contrast but sacrifices the convenient interpretation of the ellipsoids as isoprobability surfaces. This discrepancy is a common source of confusion.

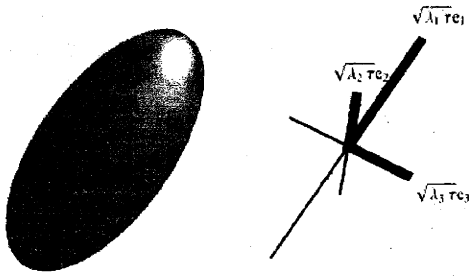

Figure 4-4: (Left) Isoprobability ellipsoid for a Gaussian diffusion function. The ellipsoid gives the surface on which the Gaussian diffusion function has constant probability. (Right) The axes of the ellipsoid are oriented in the direction of the diffusion tensor eigenvectors and have lengths proportional to the square-root of the diffusion tensor eigenvalues.

While the ellipsoidal representation has a convenient physical interpretation in terms of the isoprobability surface, for visualization purposes it is sometimes desirable to display the diffusion tensor as another geometric icon. For example, in Fig. 4-3 we displayed the tensors as rectangular cuboids in order to better emphasize the local fiber direction. Elsewhere, authors have chosen polygonal cylinders (19) in order to differentiate the major eigenvector from the medium and minor eigenvectors, or simply line segments to convey only the major eigenvector.

In general, any geometric primitive (e.g., a sphere for an ellipse, a cube for a cuboid, or a unit cylinder for a cylinder) can be mapped into the diffusion tensor coordinate system as follows. Let us define the vertex coordinate matrix $\mathbf{X}$ for the geometric primitive, where $\mathbf{X}$ is a row-matrix of the primitive's vertices. The vertex coordinate matrix then maps into the tensor eigensystem according to

$$\mathbf{X}' = \mathbf{X}\mathbf{R}^T\mathbf{\Lambda}^n \tag{4.35}$$

where $\mathbf{X}'$ is the mapped vertex coordinate matrix, $\mathbf{R}$ and $\mathbf{\Lambda}$ are as defined in Eqn. 4.34, and $n = 1$ for scaling proportional to the eigenvalues, and $n = 1/2$ for scaling proportional to the square root of the eigenvalues.

4.4.2.4 Scalar Measures

Various rotationally invariant scalar measures of the diffusion tensor can be extracted in order to summarize the geometric properties of the tensor eigensystem, facilitate visualization on a two-dimensional plane or, enable univariate statistical comparisons between subjects or groups of subjects. For intersubject comparisons the scalar maps have the additional advantage of not requiring registration of the diffusion tensors which requires some care. While many such scalar measures have been defined in the literature we will present those which we refer to in this thesis: the tensor trace, the fractional anisotropy metric, and the prolateness/oblateness metrics.

Trace

The trace T of the diffusion tensor is simply the sum of the eigenvalues

$$T = \sum_{\nu} \lambda_\nu = \sum_{\nu} D_{\nu\nu} \tag{4.36}$$

where λ_ν is the νth eigenvalue. The trace provides a measure of the total diffusion within a voxel. Curiously, the trace of the diffusion tensor is observed to be constant across normal brain tissue (22), an observation which we provide a theoretical expla-

nation for in Chap. 5.

Fractional Anisotropy

The fractional anisotropy (FA) metric is a measure of the orientational coherence of the diffusion compartments within a voxel (22). Fibers that are strongly aligned (for example, in compact white matter fascicles) exhibit high FA whereas fibers that are more weakly aligned (for example, in regions of fiber intersection) exhibit a relatively lower FA. Additionally, the FA metric can be effected by the degree of diffusion resitriction perpendicular to the fiber direction.

The FA metric is defined as

$$\mathrm{FA} = \sqrt{\frac{3}{2}}\sqrt{\frac{\sum_\nu (\lambda_\nu - \langle\lambda_\nu\rangle)^2}{\sum_\nu \lambda_\nu^2}} \tag{4.37}$$

where $\langle\lambda_\nu\rangle$ is the mean eigenvalue. The FA metric has the advantage of being automatically normalized to the unit interval and not requiring any sorting of the eigenvalues. Additionally, the FA metric is relatively insensitive to noise compared to other anisotropy metrics (22). For these reasons, the FA metric has become the most widely used measure of diffusion anisotropy in biological tissues.

Prolateness/Oblateness Metrics

Prolate geometry refers to an elongated tensor eigensystem with a high difference between the first and second eigenvalues. The prolate metric is defined as $\delta_{12} = \lambda_1 - \lambda_2$. In comparison, oblate geometry refers to a planar, sheet-like eigensystem which is captured by the oblateness metric $\delta_{23} = \lambda_2 - \lambda_3$ (19). The sheet metric is higher in regions of fiber crossing within a plane, and is helpful for identifying regions of intravoxel orientational heterogeneity (19). Examples of the various scalar images are shown in Fig. 4-5.

Figure 4-5: Examples of scalar images derived from DTI, including (a) the trace, (b) fractional anisotropy, (c) the fiber (prolateness) metric δ_{12}, and (d) the sheet (oblateness) metric δ_{23}.

4.5 Discussion

In this chapter we introduced the key Fourier relationship between the diffusion signal and the EAP for the PGSE experiment. We related the EAP measured by the q-space imaging experiment to the microgeometry functions which we introduced in the previous chapter. Upon introduction of the diffusion tensor imaging paradigm, we introduced diffusion tensor eigensystem and discussed the various scalar measures which can be derived from the tensor eigensystem.

4.6 References

[1] A. Abragam. *Principles of nuclear magnetism.* Clarendon Press, Oxford, 1961.

[2] H.C. Torrey. Bloch equations with diffusion terms. *Phys. Rev.*, 104:563–565, 1956.

[3] P.T. Callaghan. *Principles of nuclear magnetic resonance microscopy.* Oxford, Great Britain, 1993.

[4] P.J. Basser, J. Mattiello, and D. Le Bihan. MR diffusion tensor spectroscopy and imaging. *Biophys. J.*, 66:259–267, 1994.

[5] E.O. Stejskal and J.E. Tanner. Spin diffusion measurements: spin echoes in the presence of a time-dependent field gradient. *J. Chem. Phys.*, 42:288–292, 1965.

[6] D.W. McCall, D.C. Douglass, and E.W. Anderson. Self-diffusion studies by means of nuclear magnetic resonance spin-echo techniques. *Ber. Bunsenges. Physik. Chem.*, 67:336, 1963.

[7] E.T. Whittaker and G. Robinson. Normal frequency distribution. In *The calculus of observations: a treatise on numerical mathematics*, chapter 8, pages 164–208. Dover, New York, 4 edition, 1967.

[8] L.Z. Wang, A. Caprihan, and E. Fukushima. The narrow-pulse criterion for pulsed-gradient spin echo diffusion measurements. *J. Magn. Reson. A*, 117:209–219, 1995.

[9] E.O. Stejskal. Use of spin echoesd in a pulsed magnetic-field gradient to study anisotropic, restricted diffusion and flow. *J. Chem. Phys.*, 43:3597–3603, 1965.

[10] J. Kärger and W. Heink. The propagator representation of molecular transport in microporous crystallites. *J. Magn. Reson.*, 51:1–7, 1983.

[11] P.P. Mitra, L.L. Latour, R.L. Kleinberg, and C.H. Sotak. Pulsed-field gradient NMR measurements of restricted diffusion and the return-to-origin probability. *J. Magn. Reson. A*, 114:47–58, 1995.

[12] D. Le Bihan. Molecular diffusion nuclear magnetic resonance imaging. *Magn. Reson. Q.*, 7:1–30, 1991.

[13] G.G. Cleveland, D.C. Chang, and C.F. Hazlewood. Nuclear magnetic resonance measurements of skeletal muscle. Anisotropy of the diffusion coefficient of the intracellular water. *Biophys. J.*, 16:1043–1053, 1976.

[14] M. Ries, R.A. Jones, V. Dousset, and C.T. Moonen. Diffusion tensor MRI of the spinal cord. *Magn. Reson. Med.*, 44:884–892, 2000.

[15] V.J. Wedeen, T.G. Reese, V.J. Napadow, and R.J. Gilbert. Demonstration of primary and secondary muscle fiber architecture of the bovine tongue by diffusion tensor magnetic resonance imaging. *Biophys. J.*, 80:1024–1028, 2001.

[16] T.G. Reese, R.M. Weisskoff, and V.J. Wedeen. Diffusion NMR facilitated by a refocused Eddy-current EPI pulse sequence. In *Proc. Int. Soc. Magn. Reson. Med.*, volume 6, page 663, Sydney, Australia, 1998.

[17] L. Garrido, V.J. Wedeen, K.K. Kwong, U.M. Spencer, and H.L. Kantor. Anisotropy of water diffusion in the myocardium of the rat. *Circ. Res.*, 74:789–793, 1994.

[18] C. Pierpaoli, P. Jezzard, P.J. Basser, A. Barnett, and G. Di Chiro. Diffusion tensor MR imaging of human brain. *Radiology*, 201:637–648, 1996.

[19] M.R. Wiegell, H.B.W. Larsson, and V.J. Wedeen. Fiber crossing in human brain depicted with diffusion tensor MR imaging. *Radiology*, 217:897–903, 2000.

[20] P.J. Basser, J. Mattiello, and D. Le Bihan. Estimation of the effective self-diffusion tensor from the NMR spin echo. *J. Magn. Reson. B*, 103:247–254, 1994.

[21] P.J. Basser and C. Pierpaoli. Microstructural and physiological features of tissues elucidated by quantitative-diffusion-tensor MRI. *J. Magn. Reson. B*, 111:209–211, 1996.

[22] C. Pierpaoli and P.J. Basser. Toward a quantitative assessment of diffusion anisotropy. *Magn. Reson. Med.*, 36:893–906, 1996.

Chapter 5

Cross-Property Relations / Conductivity Tensor Mapping

"He will turn himself into every kind of creature that goes upon the earth, and will become also both fire and water; But you must hold him fast and grip him tighter and tighter, till he begins to talk to you and comes back to what he was when you saw him go to sleep."

Homer, *Odyssey*

5.1 Preface

In the previous chapter we showed how the diffusion tensor can be reconstructed from a set of pulsed gradient spin echo experiments, each with a different diffusion gradient direction. The eigenstructure of the diffusion tensor sheds considerable light on the microstructure of the underlying material, and hence may also provide insight into other transport phenomena which are also functions of the tissue microenvironment. Here, we describe a framework for relating disparate transport tensors through the statistics of the underlying microstructure. In particular, we focus on the relationship between the diffusion and electrical conductivity tensors, but it should be noted that the cross-property framework is readily extendible to other transport tensors.

5.2 Abstract

Knowledge of the electrical conductivity properties of excitable tissues is essential for relating the electromagnetic fields generated by the tissue to the underlying electrophysiological currents. Efforts to characterize these endogenous currents from measurements of the associated electromagnetic fields would significantly benefit from the ability to measure the electrical conductivity properties of the tissue non-invasively. Here, using an effective medium approach, we show how the electrical conductivity tensor of tissue can be quantitatively inferred from the water self-diffusion tensor as measured by diffusion tensor magnetic resonance imaging. The effective medium model indicates a strong linear relationship between the conductivity and diffusion tensor eigenvalues (respectively, σ and d) in agreement with theoretical bounds and experimental measurements presented here ($\sigma/d \sim 0.844 \pm 0.0545\text{S}\cdot\text{s/mm}^3$, $r^2 = 0.945$). The extension to other biological transport phenomena is also discussed.

5.3 Introduction

Excitable tissues such as nerve and muscle mediate communication through electrical currents. These endogenous currents are capable of generating electromagnetic fields sufficiently large to be measured outside of the body using, for example, electro/magnetoencephalography (E/MEG) in the case of the brain or electro/magnetocardiography (E/MCG) for the heart (1). The three-dimensional spatial distribution of the underlying currents can be estimated from the measured electromagnetic fields through a model-based inversion procedure which, in combination with the measuring method, is referred to as electromagnetic source imaging (ESI).

The modeling component in ESI, the so-called forward model, requires solving the quasi-static Maxwell equations in a resistor model of the anatomical region of interest, for example, the head or sternum. The underlying current distribution can then be estimated by analytical or numerical inversion of the forward model. This method has been employed to localize the electrophysiological generators associated

with cardiac and neural activity in various states of health and disease, but the accuracy of the reconstructions depends sensitively on the accuracy of the conductivity values assumed for the tissue. Modeling studies have shown for example that the external electromagnetic fields, specifically, the local field potentials measured by electroencephalography/cardiography (and, to a lesser extent, the magnetic field recorded by magnetoencephalography/cardiography), are highly sensitive to the electrical conductivity inhomogeneity and anisotropy of tissue (2–7). Hence, the lack of knowledge regarding the true electrical conductivity of the tissue can result in significant mischaracterization of the underlying currents.

Efforts to develop an imaging modality to quantitatively measure the electrical conductivity of tissue non-invasively have been largely thwarted by anatomical and biophysical barriers: the organ of interest can be shielded by highly resistive barriers such as the bony tissue of the skull, and the tissue can exhibit significant reactance, anisotropy, and microstructural heterogeneity. The difficulties associated with imaging biological conductivity *in vivo* can be appreciated by considering the limitations of electrical impedance tomography (8): the technique exhibits poor spatial resolution past resistive interfaces, particularly at the low frequencies of physiological interest; contains an ill-posed inverse problem; and requires delivering current to the tissue. Other methods suffer from additional shortcomings: magnetic resonance Hall effect imaging (9) relies on propagation of ultrasound into the tissue, and is not quantitative; and magnetic resonance current density imaging requires applying external currents sufficiently large to produce magnetic field contrast visible by MRI (10).

We have previously proposed that the electrical conductivity tensor of tissue can be quantitatively inferred from the water self-diffusion tensor as measured by diffusion tensor magnetic resonance imaging (DTI) (11–13). DTI employs an pulsed-gradient spin echo to measure the self-diffusion tensor of water in the tissue (13). The hypothesized relationship between electrical conductivity and water self-diffusion in tissue is prompted by the observation that, while there is no fundamental relationship between the two transport modes in free solution, in a structured medium such as tissue the two processes are related through mutual respect for the boundary conditions imposed

by the tissue geometry. The possibility of a connection between the conductivity and diffusion tensors can be further motivated by reports that the two tensors exhibit comparable anisotropy (on the order of 10) in cerebral white matter (14, 15).

Connections between phenomenologically distinct transport processes, so-called *cross-property* relations, have been derived, either exactly or in the form of bounds, for a broad range of transport and mechanical properties (16–18) of porous media, yet the framework has not been applied widely to biological tissues. Previously, we have studied the conductivity-diffusion cross-property in brain tissue using Monte Carlo simulations and a self-consistent effective medium approximation (11, 12, 19), but an exact formulation remained open. Here, using an effective medium framework, we derive a rigorous relationship between the conductivity and diffusion tensors without need for any assumptions on the tissue geometry, and employing a few limited assumptions on the cell membrane properties. Significantly, the model indicates a strong linear relationship between the conductivity and diffusion tensor eigenvalues, in agreement with theoretical bounds and experimental measurements reported here.

5.4 Model

The relationship between a general transport tensor, for example, the conductivity or diffusion tensor, and the underlying microstructure of the medium can be obtained from a perturbation expansion in the statistical correlations of the microstructure. Originally developed by Brown for two-phase isotropic media (20, 21) and later extended to two-phase anisotropic media by Sen and Torquato (22), the statistical correlation expansion, also referred to as a contrast moment expansion, provides a framework for relating distinct transport tensors through the statistics of the medium microstructure. The two-phase model consisting of an inclusion phase embedded in a host phase is particularly amenable to describing biological tissues as the extracellular space can be taken as the host phase and the intracellular space as the inclusion phase.

5.4.1 Cross-Property Relation

To derive the cross-property relation between the conductivity and diffusion tensors in brain tissue the approach we adopt here is to estimate the statistical moments of the microstructure from the observed diffusion tensor, and then derive the conductivity tensor from the estimated moments. We assume in the following that the cell membrane is freely permeable to water and impermeable to charge-carriers on the experimental time-scale (~50ms). Following Sen and Torquato (22), the effective transport tensor $\mathbf{\Lambda}$, denoting either the effective electrical conductivity tensor $\boldsymbol{\sigma}$ or the diffusion tensor $\mathbf{D}$, for a two-phase anisotropic medium of arbitrary topology is given by

$$(\phi_i\beta(\lambda_i,\lambda_e))^2\,\mathbf{B}^{-1}(\mathbf{\Lambda},\lambda_e\mathbf{U}) = \phi_i\beta(\lambda_i,\lambda_e) - \sum_{n=2}^{\infty}\mathbf{A}_n^{(i)}\beta^n(\lambda_i,\lambda_e) \tag{5.1}$$

where ϕ_i is the inclusion (intracellular) volume fraction, $\mathbf{U}$ is the identity tensor, and λ_i and λ_e are, respectively, the inclusion (intra-) and host medium (extracellular) transport coefficients; for example, in the case of diffusion d_i is the intracellular diffusion coefficient and d_e is the extracellular diffusion coefficient. Similarly, σ_i is the intracellular conductivity value and σ_e is the extracellular conductivity. The dimensionless contrast factors β and $\mathbf{B}$ are defined as

$$\beta(x,y) = \frac{x-y}{x+2y} \tag{5.2}$$

and

$$\mathbf{B}(\mathbf{X},\mathbf{Y}) = (\mathbf{X}+2\mathbf{Y})^{-1}(\mathbf{X}-\mathbf{Y}). \tag{5.3}$$

The rank-2 tensors $\mathbf{A}_n^{(i)}$ contain the microstructure information and are defined as integrals over the n-point probability functions S_n^i, which give the probability of finding n points within the inclusion (intracellular) phase. Exact expressions for $\mathbf{A}_n^{(i)}$ are available in Ref. 22.

By setting $\mathbf{A}_1^{(i)} = -\phi_i\mathbf{U}$, the first term on the right-hand side of Eqn. 5.1 can be

embedded in the sum to give

$$(\phi_i\beta_\lambda)^2\mathbf{B}^{-1}(\mathbf{\Lambda},\lambda_e\mathbf{U}) = -\sum_{n=1}^{\infty}\mathbf{A}_n^{(i)}\beta_\lambda^n \tag{5.4}$$

where we have defined $\beta_\lambda = \beta(\lambda_i,\lambda_e)$. The sum in the right-hand side of the above equation can be made implicit by defining the concatenation $\mathbf{C}^{(i)} = (\mathbf{A}_1^{(i)} \mid \mathbf{A}_2^{(i)} \mid \ldots)$, and, similarly, $\mathbf{G}_\lambda = (\beta_\lambda\mathbf{U} \mid \beta_\lambda^2\mathbf{U} \mid \ldots)^T$. Eqn. 5.4 then becomes

$$(\phi_i\beta_\lambda)^2\mathbf{B}^{-1}(\mathbf{\Lambda},\lambda_e\mathbf{U}) = -\mathbf{C}^{(i)}\mathbf{G}_\lambda. \tag{5.5}$$

We can obtain a least-squares estimate $\hat{\mathbf{C}}^{(i)}$ for $\mathbf{C}^{(i)}$ based on the observed diffusion tensor $\mathbf{D}$ by identifying $\mathbf{\Lambda}$ with $\mathbf{D}$ in Eqn. 5.5 and then multiplying from the right by the right-handed Moore-Penrose pseudoinverse $\mathbf{G}_d^+ = \mathbf{G}_d^T(\mathbf{G}_d\mathbf{G}_d^T)^{-1}$ [1] yielding

$$\hat{\mathbf{C}}^{(i)} = -(\phi_i\beta_d)^2\mathbf{B}^{-1}(\mathbf{D},d_e\mathbf{U})\mathbf{G}_d^+. \tag{5.6}$$

Identifying $\mathbf{\Lambda}$ in Eqn. 5.5 with $\boldsymbol{\sigma}$ and equating $\hat{\mathbf{C}}^{(i)}$ and $\mathbf{C}^{(i)}$ gives

$$\beta_\sigma^2\mathbf{B}^{-1}(\boldsymbol{\sigma},\sigma_e\mathbf{U}) = \beta_d^2\mathbf{B}^{-1}(\mathbf{D},d_e\mathbf{U})\mathbf{G}_d^+\mathbf{G}_\sigma. \tag{5.7}$$

Solving algebraically for $\mathbf{G}_d^+\mathbf{G}_\sigma$ we obtain

$$\mathbf{G}_d^+\mathbf{G}_\sigma = \frac{\beta_\sigma}{\beta_d}\left(\frac{\beta_d^2-1}{\beta_d\beta_\sigma-1}\right)\mathbf{U} \tag{5.8}$$

Finally, solving for $\boldsymbol{\sigma}$ yields

$$\boldsymbol{\sigma} = \sigma_e\mathbf{B}^{-1}(\mathbf{F},\mathbf{U}). \tag{5.9}$$

[1] The need to take the pseudo-, as opposed to the canonical, inverse highlights the point that different geometries can give rise to the same effective transport. For example, a suspension of spheres may have the same bulk diffusion as, but a different conductivity from, a matrix of randomly oriented cylinders with a different suspension volume fraction. The geometric degeneracy can be ameliorated to some degree by regularization of the pseudoinverse to respect the available theoretical bounds.

where

$$\mathbf{F} = \frac{\beta_d}{\beta_\sigma}\left(\frac{\beta_d^2 - 1}{\beta_d\beta_\sigma - 1}\right)\mathbf{B}^{-1}(\mathbf{D}, d_e\mathbf{U}). \tag{5.10}$$

The two equations above relate the conductivity and diffusion tensors solely in terms of the intra- and extracellular transport coefficients, independently of the microstructural statistics $\mathbf{A}_n^{(i)}$ and the cell volume fraction ϕ_i. We also observe that the above relationship implies that the conductivity and diffusion tensors share the same eigenvectors. Note that we have not made any assumptions yet on the type of transport tensors involved so that Eqn. 5.10 applies generally to the broader class of transport tensors including hydraulic permeability, acoustic conductivity, etc.

The equivalence between the conductivity and diffusion tensor eigenvectors allows us to express the cross-property relation solely in terms of the conductivity and diffusion tensor eigenvalues, repspectively, σ_ν and d_ν, which we do in the following. The cross-property relation can be simplified by noting that at the quasi-static frequencies of physiological interest ($<$ 1kHz) (23) the intracellular space is effectively shielded by the high resistivity of the cell membrane. The intracellular conductivity can therefore be taken as negligible. Substituting $\sigma_i = 0$ into Eqn. 10 gives

$$\sigma_\nu = \sigma_e\left[1 + \frac{3(d_\nu - d_e)(\beta_d + 2)}{d_\nu(4\beta_d^3 - 5\beta_d - 2) + d_e(8\beta_d^3 - 7\beta_d + 2)}\right]. \tag{5.11}$$

The above equation indicates a fractional linear reltionship between the conductivity and diffusion tensor eigenvalues. The relationship is highly linear however since $d_e(8\beta_d^3 - 7\beta_d + 2)$ will tend to be much larger than $d_\nu(4\beta_d^3 - 5\beta_d - 2)$, paricularly for small intracellular diffusion values. We can obtain an an explicit linear approximation to Eqn. 5.11 be taking a series expansion in the intracellular diffusion

$$\sigma_\nu = \frac{\sigma_e}{d_e}\left[d_\nu\left(\frac{d_i}{3d_e} + 1\right) + \frac{d_\nu^2 d_i}{3d_e^2} - \frac{2}{3}d_i\right] + \mathcal{O}(d_i^2). \tag{5.12}$$

Note that both the linear approximation (Eqn. 5.12) and the exact fractional linear relationship given by Eqn. 5.11 satisfy the necessary conditions $\sigma_\nu \propto \sigma_e$ and $\sigma_\nu/\sigma_e \rightarrow d_\nu/d_e$ as $d_i \rightarrow 0$, with the latter limit providing the upper-bound $\sigma_\nu/\sigma_e \leq d_\nu/d_e$. For

sake of interest, this bound can be compared to the Milton bound between the bulk elastic modulus K and conductivity $K/K_e \leq \sigma/\sigma_e$ of an isotropic material (24).

5.4.2 Bounds

We can test the feasibility of the conductivity-diffusion cross-property relation predicted by Eqn. 5.11 by comparing the relationship to the variational Hashin-Shtrikman (HS) bounds (25), which are the tightest bounds possible without taking into consideration any specific geometric properties of the tissue medium. [2] The HS bounds are specifically

$$\frac{\lambda_i\left[\lambda_e+\lambda_i+\phi_e(\lambda_e-\lambda_i)\right]}{\lambda_e\left[\lambda_e(1-\phi_e)+\lambda_i(1+\phi_e)\right]} \leq \frac{\lambda}{\lambda_e} \leq \frac{2(\lambda_e+\lambda_i)}{\lambda_e(2-\phi_e)+\lambda_i\phi_e} - 1. \tag{5.13}$$

Identifying λ with d and σ and eliminating ϕ_e we obtain the folowing greatest and least upper bounds on the conductivity eigenvalue, respectively, σ_{gu} and σ_{lu}, in terms of the diffusion eigenvalue

$$\sigma_{gu} = \frac{\sigma_e(d_i-d_\nu)(d_e+d_i)}{d_i(3d_\nu+d_i)-d_e(d_\nu+3d_i)} \tag{5.14}$$

$$\sigma_{lu} = \frac{\sigma_e d_e(d_\nu-d_i)}{d_e^2-d_\nu d_i}. \tag{5.15}$$

Comparison of the above bounds with the predictions from the cross-property relation shows that the cross-property relation holds even up to intermediate values of intracellular diffusion (Fig. 5-1). In order to experimentally test the cross-property relation, particularly the prediction of strong linearity made by Eqn. 5.12, diffusion tensor measurements were obtained and compared to reported invasive conductivity measurements in corresponding anatomical regions.

[2] It is interesting to note as an aside that the tightness of the HS bounds at low ϕ_e explains the experimentally observed conservation of the trace of the diffusion tensor in brain tissue (14).

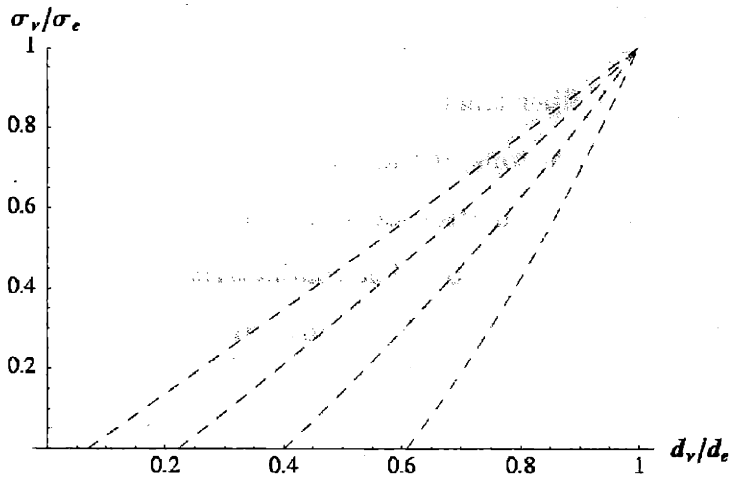

Figure 5-1: Theoretical cross-property relationship between the conductivity and diffusion tensor eigenvalues normalized by the corresponding extracellular transport coefficient. The family of dotted curves gives the cross-property relationship for values of, from left to right, $d_i/d_e = \{0.1, 0.3, 0.5, 0.7\}$. The shaded regions indicate the the greatest and least upper bounds predicted by the HS bounds (25).

5.5 Methods

5.5.1 MRI Methods

Axial, balanced echo (26) diffusion tensor measurements of 4 subjects were taken at 1.5T (GE Signa) with TR/TE/τ=3000/93/30ms, b=577.3s/mm^2, 16 averages. 38 slices were obtained with a 40×20cm^2 field-of-view (256 × 128) giving 1.56 × 1.56 × 3mm^3 voxels. The diffusion gradient (g = 14.14mT/m) was applied in the directions of the 6 non-opposed edge-centers of a cube in k-space as described elsewhere (27).

5.5.2 Comparison to Invasive Measurements

The diffusion values were sampled in cortex, the parasagital sulcus, the anterior internal capsule, subcortical white matter, and the cerebellum. The locations were selected based on the locations of reported invasive conductivity measurements (15, 28–32). The diffusion values were taken from either the laboratory frame or eigenframe de-

pending on the reference frame in which the original invasive conductivity values were measured. If the full conductivity tensor was not specified, then the directions parallel and perpendicular to the fiber tract were taken to be, respectively, the directions of the major and minor eigenvectors. If the orientation of the conductivity measurement was not specified for a gray matter location, then the average eigenvalue of the diffusion tensor was used for comparison. The conductivity values were obtained from various species but should still reflect the overall trend in the conductivity-diffusion relation.

5.6 Results

The full fractional linear relationship (Eqn. 5.11) was fit to the conductivity and diffusion data, as was a linear relationship of the form $\sigma_\nu = k(d_\nu - d_\epsilon)$ for comparison. The former yielded $\sigma_e = 1.52 \pm 0.251$S/m, $d_e = 2.04 \pm 0.506\mu$m^2/ms, and $d_i = 0.117 \pm 0.0972\mu$m^2/ms. The uncertainty in the estimates for σ_e and d_e was principally due to the strong linear behavior in σ_e/d_e. The linear fit yielded $k = 0.844 \pm 0.0545$S·s/mm^3 ($p < 10^{-9}$) and $d_\epsilon = 0.124 \pm 0.0540\mu$m^2/ms ($p < 0.05$) with $r^2 = 0.945$. The linear relation provided a good approximation to the conductivity and diffusion data and could not be distinguished from the full fractional linear model based on the present data (Fig. 5-2). The linear relationship was used to generate the conductivity tensor image of the brain shown in Fig. 5-3.

The conductivity data fell into three distinct clusters due to the sampling of the conductivity values in (i) gray matter and in white matter (ii) parallel and (iii) perpendicular to the fiber tract. In order to determine if the linear relation could describe the behavior within these individual tissue classes, the linear model was also evaluated within the individual classes. The conductivity and diffusion values were not found to be significantly correlated ($p > 0.05$) within the tissue classes, indicating that the observed linearity followed primarily from the behavior across the tissue classes. It was not clear from the limited data available if the variability within the tissue classes was due to true disagreement with the model or experimental

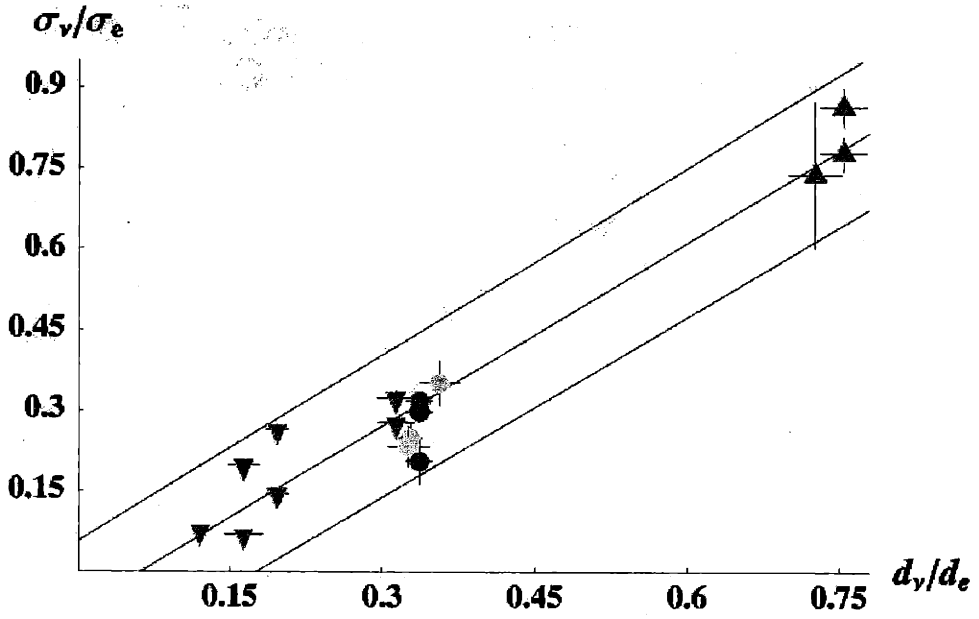

Figure 5-2: Experimental relationship between the conductivity and diffusion tensor eigenvalues (mean±SEM). The conductivity values were obtained from reported invasive measurements and the diffusion values from diffusion tensor MRI in the corresponding anatomical regions. The solid line depicts the linear fit, and the dashed lines the upper and lower confidence intervals on the linear fit. The conductivity values were taken from the average over cortex (blue circle, Ref. 28); (red circle , Ref. 31), the average subcortical white matter perpendicular to the tract (blue inverted triangle, Ref. 28), somatosensory cortex in three perpendicular directions (yellow circle, Ref. 30), the parasagital sulcus (light blue circle, Ref. 29), the subcortical white matter beneath the parasagital sulcus measured perpendicular to the tract (light blue inverted triangle, Ref. 29), the cerebellum parallel (green triangle) and perpendicular (green inverted triangle) to the dominant fiber orientation (Ref. 32), and the anterior internal capsule parallel (purple triangle) and perpendicular (inverted purple triangle) to the tract (Ref. 15).

uncertainties such as anatomical heterogeneity, trans-species variability, and possible misspecification of the measurement orientation.

5.7 Discussion

We have derived a rigorous cross-property relation between the electrical conductivity and water self-diffusion tensors in brain tissue by relating the two transport processes through the statistical moments of the tissue microstructure. The cross-property re-

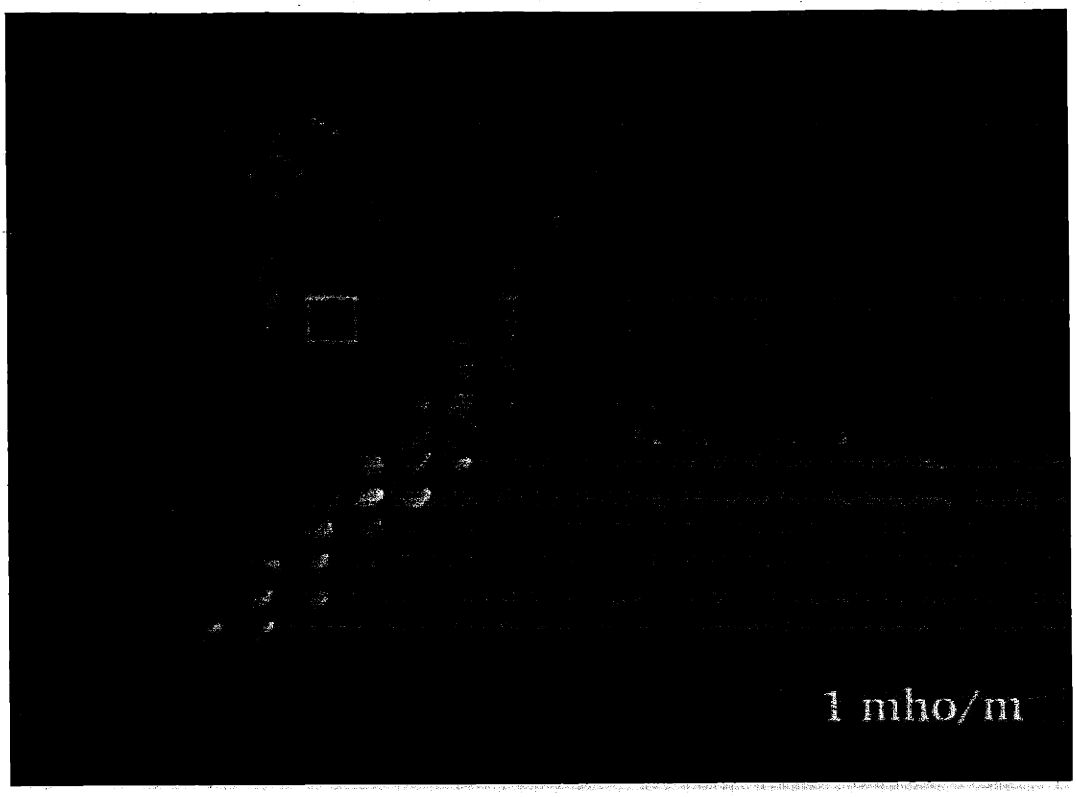

Figure 5-3: Axial electrical conductivity tensor map of the human brain derived from the linear cross-property relation. The region of interest is highlighted in the T2-weighted image shown at top left. The conductivity tensor within each voxel is represented by a three-dimensional ellipsoid. The axes of the ellipsoid are oriented in the direction of the conductivity tensor eigenvectors and are scaled by the corresponding eigenvalues. The length of the axis relative to the isotropic tensor (1S/m) (bottom right) gives the quantitative conductivity value. The color of the ellipsoid reflects the orientation of the principal eigenvector according to the red-green-blue sphere (top right) with red indicating medio-lateral, green antero-posterior, and blue supero-inferior. The brightness of the tensor is scaled by the degree of anisotropy. Note the strong anisotropy in the optical radiation (green), the tapetum (blue), and the U-fiber between the middle occipital and temporal gyri (red).

lationship was found to respect theoretical bounds for a large range of intracellular diffusion values, and successfully captured the salient experimental observations: (i) a strong linear relation between the conductivity and diffusion eigenvalues, and (ii) a signficant diffusion intercept at zero conductivity. The persistence of diffusion at zero conductivity can be understood by considering the following scenario. If the extracellular volume fraction is less than the percolation threshold (i.e., the extracel-

lular space volume fraction at which the extracellular space is no longer topologically connected) the conductivity will vanish, but the diffusion will survive in the intracellular space and the disconnected extracellular pores. The surviving diffusivity at the percolation threshold will be on the order of the diffusion values d_i and d_ϵ derived here. Interestingly, these values are consistent with the 'slow' diffusion component $d_s = 0.168\mu\text{m}^2/\text{ms}$ observed at short diffusion times (33) which has been postulated to be the intracellular diffusion component. Furthermore, the value derived here for the extracellular conductivity is consistent with reported meaurements for the conductivity of cerebrospinal fluid ($\sigma = 1.79\text{S/m}$, Ref. 34) and ($\sigma_e = 1.54\text{S/m}$, Ref. 35, 36).

The quantitative conductivity tensor maps provided by the cross-property model promise to improve the accuracy of electromagnetic field modeling in tissue with application to a range of bioelectromagnetic technologies including ESI, transcranial magnetic stimulation, and cardiac defibrillation. The cross-property framework will find particular application in the forward model for ESI, where the empirical conductivity values will benefit both the accuracy and resolution of the source estimates. In particular, the inclusion of conductivity inhomoegeneities in the forward model will provide a basis for distinguishing sources inside or outside of the inhomogeneity.

The ability to quantify the currents based on the empirical conductivity measurements will furthermore allow for fusion of data from electric and magnetic imaging modalities. As the electric and magnetic fields are sensitive to different source configurations and locations, the combination of modalities will help to further resolve the true underlying current distribution (37). Lastly, the cross-property framework is extendible to other transport and mechanical properties of tissue including thermal and acoustic conductivity, elastic stiffness, hydraulic permeability, and photon diffusion.

This chapter was published in Ref. 38, which evolved from previous work published in Refs. 11, 12, 39. We have also performed a sensitivity analysis of the effects of conductivity anisotropy on human EEG and MEG measurements (40) using methods developed in Ref. 41.

5.8 References

[1] R. Plonsey. *Bioelectric phenomena.* McGraw-Hill, New York, 1969.

[2] J. Haueisen, C. Ramon, M. Eiselt, H. Brauer, and H.J. Nowak. Influence of tissue resistivities on neuromagnetic fields and electric potentials studied with a finite element model of the head. *IEEE Trans. Biomed. Eng.*, 44:727–735, 1997.

[3] J. Haueisen, A. Bottner, H. Nowak, H. Brauer, and C. Weiller. The influence of conductivity changes in boundary element compartments on the forward and inverse problem in electroencephalography and magnetoencephalography. *Biomed. Tech. (Berlin)*, 44:150–157, 1999.

[4] M.J. Peters and J.C. De Munck. The influence of model parameters on the inverse solution based on MEGs and EEGs. *Acta. Otolaryngol. Suppl.*, 491:61–68 (discussion 69, 1991.

[5] H. Zhou and A. van Oosterom. Computation of the potential distribution in a four-layer anisotropic concentric spherical volume conductor. *IEEE Trans. Biomed. Eng.*, 39:154–158, 1992.

[6] R.N. Klepfer, C.R. Johnson, and R.S. Macleod. The effects of inhomogeneities and anisotropies on electrocardiographic fields: a 3-D finite-element study. *IEEE Trans. Biomed. Eng.*, 44:706–719, 1997.

[7] Y. Rudy, R. Plonsey, and J. Liebman. The effects of variations in conductivity and geometrical parameters on the electrocardiogram, using an eccentric spheres model. *Circ. Res.*, 44:104–111, 1979.

[8] P. Metherall, D.C. Barber, R.H. Smallwood, and B.H. Brown. Three-dimensional electrical impedance tomography. *Nature*, 380:509–512, 1996.

[9] H. Wen, J. Shah, and R.S. Balaban. Hall effect imaging. *IEEE Trans. Biomed. Eng.*, 45:119–124, 1998.

[10] M. Joy, G. Scott, and M. Henkelman. In vivo detection of applied electric currents by magnetic resonance imaging. *Magn. Reson. Imag.*, 7:89–94, 1989.

[11] D.S. Tuch, V.J. Wedeen, A.M. Dale, J.W. Belliveau, and V.J. Wedeen. Electrical conductivity tensor map of the human brain using NMR diffusion imaging: an effective medium approach. In *Proc. Int. Soc. Magn. Reson. Med.*, volume 6, page 572, Sydney, Australia, 1998.

[12] D.S. Tuch, V.J. Wedeen, A.M. Dale, J.S. George, and J.W. Belliveau. Conductivity mapping of biological tissue using diffusion MRI. *Ann. NY Acad. Sci.*, 888:314–316, 1999.

[13] P.J. Basser, J. Mattiello, and D. Le Bihan. MR diffusion tensor spectroscopy and imaging. *Biophys. J.*, 66:259–267, 1994.

[14] C. Pierpaoli and P.J. Basser. Toward a quantitative assessment of diffusion anisotropy. *Magn. Reson. Med.*, 36:893–906, 1996.

[15] P.W. Nicholson. Specific impedance of cerebral white matter. *Exp. Neurol.*, 13:386–401, 1965.

[16] M. Avellaneda and S. Torquato. Rigorous link between fluid permeability, electrical conductivity, and relaxation times for transport in porous media. *Phys. Fluids A*, 3:2529–2540, 1991.

[17] L. Gibiansky and S. Torquato. Rigorous connection between physical properties of porous rocks. *J. Geophys. Res. (Solid Earth)*, 103:23911–23923, 1998.

[18] L. V. Gibiansky and S. Torquato. Link between the conductivity and elastic moduli of composite materials. *Phys. Rev. Lett.*, 71:2927–2930, 1993.

[19] P.N. Sen, C. Scala, and M.H. Cohen. A self-similar model for sedimentary rocks with application to the dielectric constant of fused glass beads. *Geophysics*, 46:781–795, 1981.

[20] W.F. Brown. Solid mixture permittivities. *J. Chem. Phys.*, 23:1514–1517, 1955.

[21] M.J. Beran. *Statistical Continuum Theories.* Wiley, New York, 1968.

[22] A.K. Sen and S. Torquato. Effective conductivity of anisotropic two-phase composite media. *Phys. Rev. B*, 39:4504–4515, 1989.

[23] R. Plonsey and D.B. Heppner. Considerations of quasi-stationarity in electrophysiological systems. *Bull. Math. Biophys.*, 29:657–664, 1967.

[24] G.W. Milton. In D.L. Johnson and P.N. Sen, editors, *Physics and Chemistry of Porous Media.* American Institute of Physics, New York, 1984.

[25] Z. Hashin. On elastic behavior of fiber-reinforced materials of arbitrary transverse phase geometry. *J. Mech. Phys. Solids*, 13:119–134, 1965.

[26] T.G. Reese, R.M. Weisskoff, and V.J. Wedeen. Diffusion NMR facilitated by a refocused Eddy-current EPI pulse sequence. In *Proc. Int. Soc. Magn. Reson. Med.*, volume 6, page 663, Sydney, Australia, 1998.

[27] T.G. Reese, R.M. Weisskoff, R.N. Smith, B.R. Rosen, R.E. Dinsmore, and V.J. Wedeen. Imaging myocardial fiber architecture in vivo with magnetic resonance. *Magn. Reson. Med.*, 34:786–791, 1995.

[28] W.H. Freygang and W.M. Landau. Some relations between resistivity and electrical activity in the cerebral cortex of the cat. *J. Cell. Comp. Physiol.*, 45:377–391, 1955.

[29] A. van Harreveld, T. Murphy, and K.W. Nobel. Specific impedance of rabbit's cortical tissue. *Am. J. Physiol.*, 205:203–207, 1963.

[30] P.B. Hoeltzell and R.W. Dykes. Conductivity in the somatosensory cortex of the cat - evidence for cortical anisotropy. *Brain Res.*, 177:61–82, 1979.

[31] J.B. Ranck Jr. Specific impedance of rabbit cerebral cortex. *Exp. Neurol.*, 7:144–152, 1963.

[32] C. Nicholson and J.A. Freeman. Theory of current source-density analysis and determination of conductivity tensor for anuran cerebellum. *J. Neurophysiol.*, 38:356–368, 1975.

[33] T. Niendorf, R.M. Dijkhuizen, D.G. Norris, M. van Lookeren Campagne, and K. Nicolay. Biexponential diffusion attenuation in various states of brain tissue: implications for diffusion-weighted imaging. *Magn. Reson. Med.*, 36:847–857, 1996.

[34] S.B. Baumann, D.R. Wozny, S.K. Kelly, and F.M. Meno. The electrical conductivity of human cerebrospinal fluid at body temperature. *IEEE Trans. Biomed. Eng.*, 44:220–223, 1997.

[35] L.A. Geddes and L.E. Baker. The specific resistance of biological materials - a compendium of data for the biomedical engineer and physiologist. *Med. & Biol. Eng.*, 5:271–293, 1967.

[36] B.J. Roth and K.W. Altman. Steady-state point-source stimulation of a nerve containing axons with an arbitrary distribution of diameters. *Med. Biol. Eng. Comput.*, 30:103–108, 1992.

[37] A.K. Liu, A.M. Dale, and J.W. Belliveau. *Human Brain Mapping*, 2001 (in press).

[38] D.S. Tuch, V.J. Wedeen, A.M. Dale, J.S. George, and J.W. Belliveau. Conductivity tensor mapping of the human brain using diffusion tensor MRI. *Proc. Natl. Acad. Sci. USA*, 98:11697–11701, 2001.

[39] D.S. Tuch, V.J. Wedeen, O. Schwarz, A.M. Dale, J.S. George, and J.W. Belliveau. Electroencephalography forward solutions in magnetic resonance conductivity tensor maps. In *Proc. Int. Hans Berger Congress*, volume 4, page 1, Jena, Germany, 1999. Published in Neuroimage, vol. 40(.

[40] J. Haueisen, D.S. Tuch et. al. The influence of brain anisotropy on human EEG and MEG. *Neuroimage*, 2001 (in press).

[41] C.H. Wolters, U. Hartmann, M. Koch, F. Kruggel, S. Burkhardt, A. Basermann, D.S. Tuch, and J. Haueisen. New methods for improved and accelerated FE-volume conductor modeling in EEG/MEG-source reconstruction. In *Proc. 4th Int. Symp. on Computer Methods in Biomech. and Biomed. Eng.*, Lisboa, 1999.

Chapter 6

Thalamic Parcellation

"Why, cut it off, piece after piece, And throw the tough cortex away...."

Allen Tate, *Homily*

6.1 Preface

In addition to providing insight into transport processes in tissue, diffusion tensor imaging can reveal anatomical structure irresolvable by conventional MRI. Here, we show that the nuclei of the thalamus, a midbrain structure responsible for relaying signals between the periphery and higher cortex, can be resolved from the characteristic fiber orientations of the individual nuclei. The detection of secondary planar structure in the thalamus will motivate the following chapters on resolving composite fiber structure with diffusion imaging.

6.2 Abstract

The thalamic nuclei have conventionally been identified by their distinct cyto / myeloarchitecture on histology. Diffusion tensor magnetic resonance imaging (DTI) offers a non-invasive alternative to histology by measuring the fiber orientation and the orientational coherence within each imaging element. Here we show that DTI can resolve the major nuclei based on their characteristic fiber orientations. Locations for the

nuclei obtained by automatic segmentation of the DTI agreed strongly with reported histology. The ability to resolve thalamic nuclei non-invasively on a per subject basis will allow for morphometrics of specific nuclei, more accurate neurosurgical planning, and improved anatomical localization of functional activation in the thalamus.

6.3 Introduction

The thalamus is the central relay station for the brain, mediating communication between sensory, motor and associative brain regions. The functional compartmentalization of the thalamus is reflected in the division of the thalamic architecture into distinct functionally-specific nuclei. The nuclei have conventionally been delineated by their characteristic cyto- and myeloarchitectural appearance on histology (1–4). The number of thalamic nuclei reported with histological methods varies with the method employed, although most cyto/myeloarchitecture stains identify fourteen major nuclei, with several subdivisions of the individual nuclei, some established by additional chemoarchitectural stains.

Thalamic changes have been implicated in a large number of diseases, including schizophrenia (5–7), , Parkinsons disease (8–12), chronic pain syndrome (13), Multiple Sclerosis (14) and Wallarian degeneration (15)). Parkinsons disease, Multiple Sclerosis and chronic pain syndrome can also be treated by surgical ablation or electric stimulation (16) of the involved nucleus. The presurgical planning of these cases often use generic thalamic atlases to target the pertinent nucleus (17–20). Given the large degree of intersubject variability (3) in the location and size of the thalamic nuclei, such generic atlases may be highly inaccurate. Functional studies (fMRI, PET, SPECT) have also documented disease-related changes in functional activation of the thalamus (21–26). However, due to the lack of a precise anatomical reference, these studies are generally not able to localize the activation to a specific nucleus within the thalamus.

The ability to resolve thalamic nuclei by non-invasive imaging would enable quantitative morphometrics of the thalamic changes in the abovementioned diseases, provide

more accurate neurosurgical planning, and offer improved anatomical localization of functional activation. Radiological identification of individual thalamic nuclei is not currently possible, however, as present imaging methods such as CT and conventional MR do not provide the necessary image contrast to differentiate the nuclei. Magnotta et al. (27) have shown that gray matter-nulled, inversion recovery T1-weighted MRI can identify the medialdorsal (MD) nucleus and the lateral portion based on the differences in white matter content, but further substructure was difficult to resolve. Furthermore, the T1 contrast between the nuclei was relatively small, with MD lower and the lateral portion higher in T1 signal (28).

Previously, it has been proposed that the thalamic nuclei can be distinguished by their characteristic fiber orientation, (29–31) a hereto unexploited distinction between the thalamic nuclei. This approach was motivated by the hypothesis that fiber orientations are relatively aligned within a nucleus due to fact that the cerebrocortical striations within a given nucleus all target the same region of cortex. Conventional MRI provides no information on the fiber orientation. However, diffusion tensor magnetic resonance imaging (DTI) can resolve the dominant fiber orientation within each image element (32–38) by measuring the self-diffusion (i.e., Brownian motion) properties of the water molecules within the tissue. In tissues with strongly aligned microstructure such as brain or muscle (39–43), diffusion is observed to be anisotropic (i.e., orientationally dependent) which is due to the diffusion barriers presented by cell membranes and/or macromolecules.

The direction of greatest diffusion measured by DTI parallels the dominant orientation of the tissue microstructure within each voxel. For example, the direction of greatest diffusion in cerebral white matter correlates strongly with the mean longitudinal direction of the axons. Diffusion anisotropy of white matter has furthermore been observed to depend on fiber heterogeneity (38,44) and to increase with myelination (32,45–49). In contrast, the diffusion tensor in cortical gray matter45 has been shown to be isotropic and the same was thought to be true for subcortical gray matter structures. However, unlike other subcortical gray matter structures the thalamus contains both unmyelinated nerves and myelinated nerves. The unmyelinated nerves

consist of intrathalamic relay and connections between the basal ganglia and the brain stem nuclei. The myelinated nerves are the thalamocortical striations, which provide sufficient diffusion restriction to be visible by DTI. Hence, we sought to test whether fiber orientation maps measured by DTI could distinguish the thalamic nuclei.

Using DTI we observed significant clusters of common fiber orientation in regions corresponding to the anatomical locations of the nuclei. Visual comparison with histological atlases (3, 50) showed correspondence between the location of the orientation clusters and the classically defined nuclei locations. In order to more accurately assess the diffusion tensor results we segmented the diffusion tensor data using a modified k-means algorithm (51), and compared the center-of-mass coordinates of the segmented nuclei with previously reported center-of-mass coordinates obtained from a Talairached histological atlas (31). The diffusion tensor segmentation showed strong agreement with the histological data, providing support for the accuracy and robustness of the diffusion tensor method and the segmentation.

6.4 Methods

6.4.1 Data Acquisition

Diffusion tensor MRI was obtained in healthy normal volunteers on a 1.5 T Siemens Vision Scanner at the Danish Research Center for Magnetic Resonance, Hvidovre Hospital, Denmark. The volunteers consented in accordance with the procedures of the Danish Ethical Committee. For each subject, data were acquired for 12 contiguous slices covering the whole thalamus and oriented either axially or coronally. We used a single-shot SE-DWI-EPI sequence, with TE=101ms, TR=4s, Matrix size=128×128, FOV=230mm, slice thickness=3mm. The diffusion-encoding parameters were δ = 28.9 ms, Δ = 51.9 ms and diffusion time 42.6ms, gradient strength 12 mT/m, which gave an approximate b-factor of 550 s/mm^2, calculated analytically taking preparation and imaging gradients into account (52). One null image and six diffusion weighted images were obtained with the diffusion-encoding gradients directed along

the following axes (±1,1,0), (±1,0,1) and (0,±1,1). The SNR obtained in the non-averaged unattenuated diffusion weighted image was about 15, resulting in a SNR for the 36 times averaged DW images of approximately 90. The images were realigned to compensate for eddy-current induced morphing in the phase and readout directions, although eddy-currents were only detected in the phase direction. Images with motion artifacts were excluded. The eigensystem of the diffusion tensor was calculated on a voxel by voxel basis (52).

6.4.2 Automatic Segmentation Procedure

The thalamic nuclei were clustered separately for each hemisphere using the k-means clustering algorithm(52). In general, the k-means algorithm requires four specifications: (i) the number of clusters, (ii) a distance metric, (iii) initialization of the cluster centroids, and (iv) a convergence criterion.

Number of clusters. The number of nuclei (clusters) was set a priori to $n = 14$ per hemisphere based on preliminary visual inspection (29).

Distance Metric. The distance between voxels was defined as a linear combination of the Mahalanobis voxel distance and the Frobenius tensor distance. More specifically, the position-diffusion-tensor distance E_{jk} between a voxel j and a centroid k was taken as a linear combination of the voxel position distance and the diffusion tensor distance, i.e.,

$$E_{jk} = ||\mathbf{x}_j - \mathbf{m}_k||_{\mathbf{W}_k} + \gamma||\mathbf{D}_j - \mathbf{T}_k|| \tag{6.1}$$

where $\mathbf{x}_j$ is the location of voxel j, $\mathbf{m}_k$ is the mean voxel location for cluster k, $\mathbf{W}$ is the covariance matrix for the voxels in cluster k, γ is a weighting factor to specify the trade-off between the diffusion tensor distance and the voxel distance, $\mathbf{D}_j$ is the diffusion tensor for voxel$j$, and $\mathbf{T}_k$ is the mean diffusion tensor for cluster k. The norm on the voxel location is the Mahalanobis norm defined as $||\mathbf{x}||_{\mathbf{W}} = (\mathbf{x}^T\mathbf{W}^{-1}\mathbf{x})^{1/2}$ and the norm on the diffusion tensor is the Frobenius norm defined as $||\mathbf{F}|| = [\mathrm{Tr}(\mathbf{F}^T\mathbf{F})]^{1/2}$, where Tr is the trace of tensor $\mathbf{F}$. The Mahalanobis distance was used, as opposed to

an unadjusted Euclidean norm, in order to prevent geometric bias towards spherical clusters. The covariance matrices $\mathbf{W}_k$ were recalculated at every iteration. The weighting factor γ was chosen a priori for each subject using the formula

$$\gamma = \alpha \sum_j ||\mathbf{x}_j||/||\mathbf{D}_j|| \tag{6.2}$$

with the factor α set to $1/4$.

Initialization of the cluster centroids. The n centroid locations were initialized along each side of a line segment passing from the posterior tip of the thalamic hemisphere through the center-of-mass to the anterior tip within the plane spanned by the first and second eigenvectors of the voxel location covariance matrix.

Convergence criterion. The clustering routine was iterated until no centroid moved more than 0.1mm.

Nuclei identification. Following Niemann (31), 12 nuclei (17 in total including subdivisions) were assigned to the clusters. The nuclei, including the subdivisions in square brackets, were AV, MD, LD, LP, VA, VL [VLa, VLp], VPM, VPL, CM, Pu [PuA, PuM, PuL], LGN, MGN, respectively. The nuclei were assigned to the 14 clusters per hemisphere based on the location, shape, size and orientation of the segmentation cluster. If a cluster was assigned to a nucleus, which contained subdivisions but the assignment to a particular subdivision could not be made, then the cluster was assigned to the undifferentiated nucleus. For example, if a cluster belonged to VL but could not be assigned definitely to VLa or VLp it was assigned to VL. If a cluster subsumed 2 anatomical nuclei then the cluster was assigned to both nuclei, and the center-of-mass and volume statistics were attributed to both nuclei. If multiple clusters were consistent with the same nucleus, then all of the clusters were assigned to that nucleus. In that case, the center-of-mass (COM) and volume statistics were taken from the cluster which agreed most strongly in morphometry and location with the nucleus used by Niemann (AV, CM, LP, MDmc MGN, PuA, VLa and VPLa, respectively).

6.4.3 Center-of-Mass Comparison

Eight nuclei (AV, CM, LP, MDmc, MGN, PuA, VLa and VPLa) of the thirteen reported nuclei COM coordinates from Niemann (31) were used for the center-of-mass comparison. Of the five remaining nuclei, the red nucleus and the subthalmic nucleus were outside the area considered in this paper; the habenular nucleus and the ventromedial nucleus were deemed too small for detection with our present spatial image resolution, and the parafascicular nucleus was considered as part of the centromedian-parafascicular nuclei complex. The center-of-mass (COM) coordinates for the segmented nuclei were registered to Talairach space using the AC-PC plane as a landmark and then scaled in the Talairach frame to account for AC-PC distance variability as was done in Niemann (31). The corrected Talairach coordinates were then pooled over the subjects ($N = 4$). The corrected COM coordinates reported by Niemann were obtained by digitally scanning the published data (31) and likewise pooling over the subjects ($N = 2$). The agreement between the segmentation and the Niemann COM coordinates was assessed with a multivariate anova test at a significance level of 0.05.

6.5 Results

The mean volume of the thalamus determined from the structural images was $7108 \pm 918\text{mm}^3$ (per hemisphere), and the mean distance from the anterior commisure to the posterior commisure (ACPC) was 28.4 ± 3.3mm. The volume of the left thalamic hemisphere was $7141 \pm 530\text{mm}^3$ and the right hemisphere $7073 \pm 457\text{mm}^3$. The diffusion tensor data were visualized as cylindrical icon fields against a background color-coded according to the direction of the sheet-normal vector (the third eigenvector) (44) (Fig. 6-1). The mean fractional anisotropy (FA) (39) over the thalamic volume was 0.364 ± 0.007.

The diffusion tensor images showed clusters of common fiber orientation corresponding to the direction of the corticothalamic and thalamocortical striations within each nucleus. The sheet-normal direction also exhibited clustering that did not always

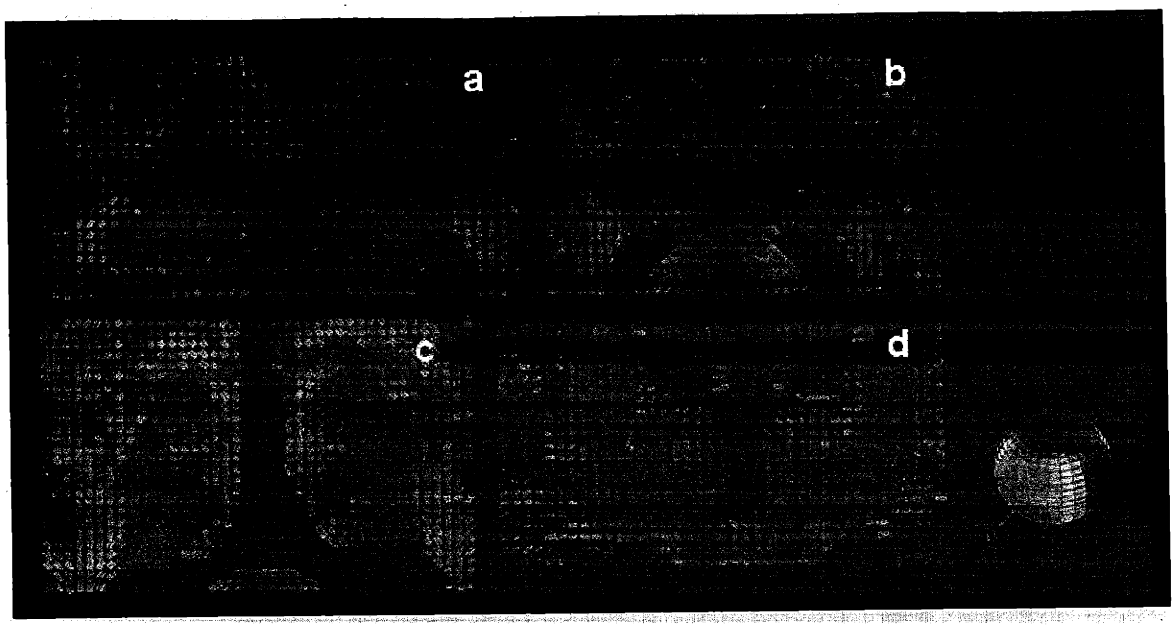

Figure 6-1: Mid-thalamic diffusion tensor images of 4 subjects (a,b,c,d). Images a-c are axial slices and image d is a coronal slice at approximately mid-thalamic level. The cylinders depict the diffusion tensor within each voxel. The axes of each cylinder are oriented in the direction of the principal eigenvector of the local diffusion tensor. The length of the axes are scaled by the product of the corresponding eigenvalue and the square-root of the fractional anisotropy metric (39). The cylinders are colored by the direction of the principal eigenvector according to the red-green-blue sphere shown at bottom right with red indicating mediolateral, green anteroposterior, and blue superoinferior direction. The background slice is colored by the direction of the third eigenvector, an indicator of the sheet-normal direction, which describes the intra-voxel spread of fiber orientations in terms of planar architecture (44). Note that the clustering of the mean fiber direction (32,33,53,54) does not completely coincide with the clustering of the sheet direction.

coincide with the clustering suggested by the mean fiber direction. The location of the fiber orientation clusters defined by both the fiber and sheet directions corresponded generally with the location of the nuclei provided by histological atlases (Fig. 6-2).

Each of the 14 segmentation clusters (Figs. 6-3 and 6-4) was assigned to anatomical nuclei according to the criteria described in the Methods section (Fig. 6-5). The location, size, and shape of the segmented nuclei were consistent with Morel's stereotactic atlas (2). The relative location of the clusters within an individual thalamus was consistent between subjects, but the cluster locations and morphometry varied between subjects. The mean orientation of fibers within each nucleus showed high correlation between subjects (Table 6.1). The agreement between the segmentation

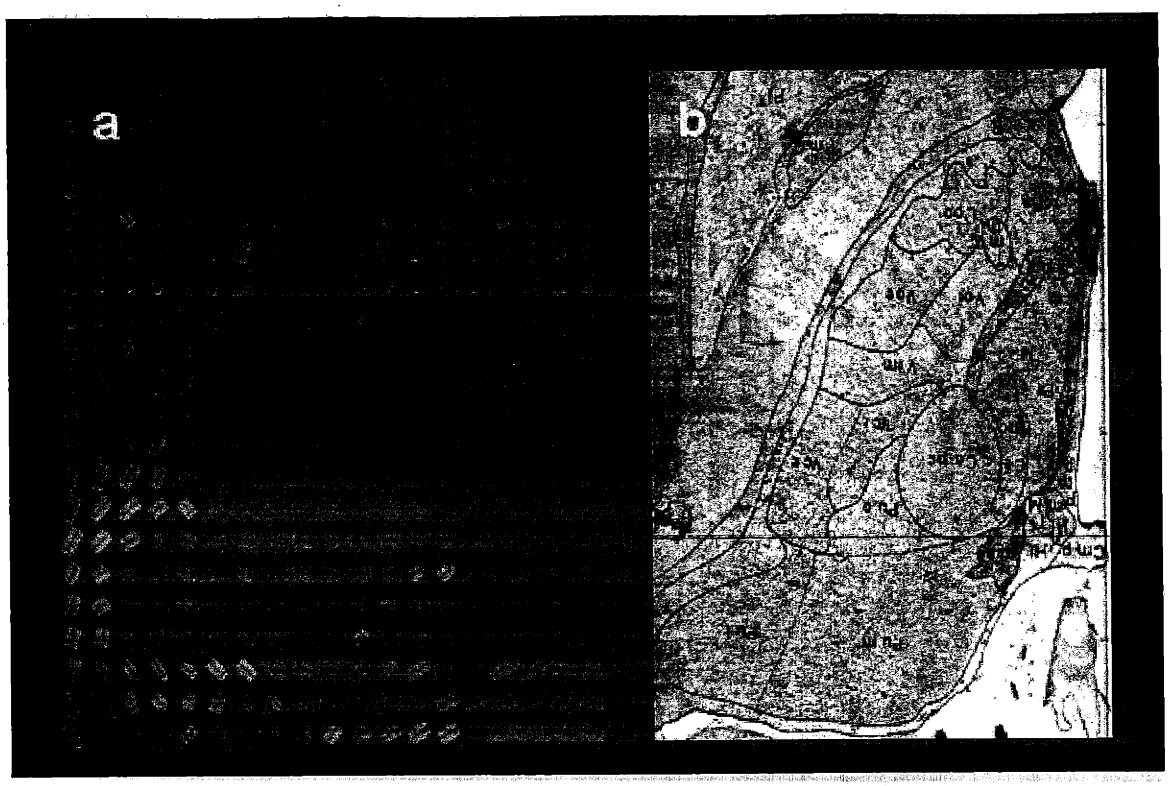

Figure 6-2: Histological comparison. (a) Diffusion tensor image (Fig. 6-1a) compared with a histological slice (b) from Van Buren et al (3) at a similar anatomical level. Note the correspondence between diffusion orientation clusters and histologically defined nuclei borders.

and the Niemann (31) center-of-mass (COM) coordinates was assessed with a multivariate anova test (Fig. 6-6). For six (AV, CM, LP, MGN, PuA and VPLa) out of the 8 nuclei (AV, CM, LP, MD, VLa, MGN, PuA and VPLa) specified by Niemann we were not able to reject the null hypothesis (at a 0.05 significance level) that the COM coordinates were the same in the DTI and histological segmentations. For the nuclei that successfully agreed with Niemann's segmentation, the p-values were AV ($p = 0.526$), CM ($p = 0.623$), LP ($p = 0.481$), MGN ($p = 0.357$), PuA ($p = 0.436$) and VPLa ($p = 0.433$).

From Table 6.1 it can be appreciated that the diffusion orientations of the individual nuclei correspond to their respective corticothalamic and thalamocortical striations (Table 6.2). For example the medial dorsal (MD) nuclei has an anteroposterior direction corresponding to the direction of its projections to the frontal

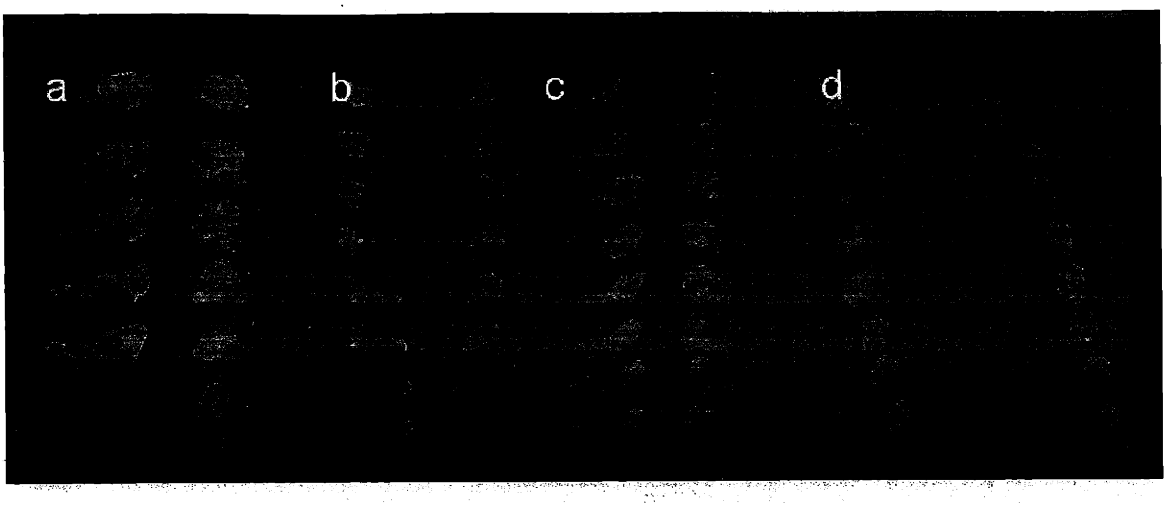

Figure 6-3: Automatic segmentation results (a-d) for the left and right thalamic hemispheres of the 4 subjects respectively. The clusters are color-coded by the principal eigenvector of the mean diffusion tensor within each cluster (colorsphere in the lower right corner). The slices are artificially expanded by 11 mm for the axial data sets (a-c) and 19 mm for the coronal data set (d) in order to facilitate visualization.

association cortices through the anterior limb of the internal capsule. Likewise the ventrolateral (VL) nucleus exhibit anteroposterior direction although with a superoinferior tendency (more blue color), corresponding to the direction of the striations to the premotor and primary motor cortices through the anterior limb of the internal capsule.

The ventroposterior nucleus, often subdivided into two nuclei - the ventral posterolateral (VPL) and ventral posteromedial (VPM), exhibited almost the same orientation. Both nuclei receive input from the spinal cord, the brain stem and the medial lemniscus and project to primary somatic sensory cortex. The two nuclei differ, however, in their target areas, body and head respectively, in addition to projections to the insula cortex from VPM. This is reflected in the orientations of the two nuclei with both nuclei showing superoinferior and mediolateral orientation corresponding to the striations through the posterior limb of the internal capsule. Where VPM was identified, the nucleus showed orientations more mediolateral than those of VPL confirming the additional projection to the insula cortex.

Of the intralaminar nuclei, the centro median (CM) and the parafascilus nuclei

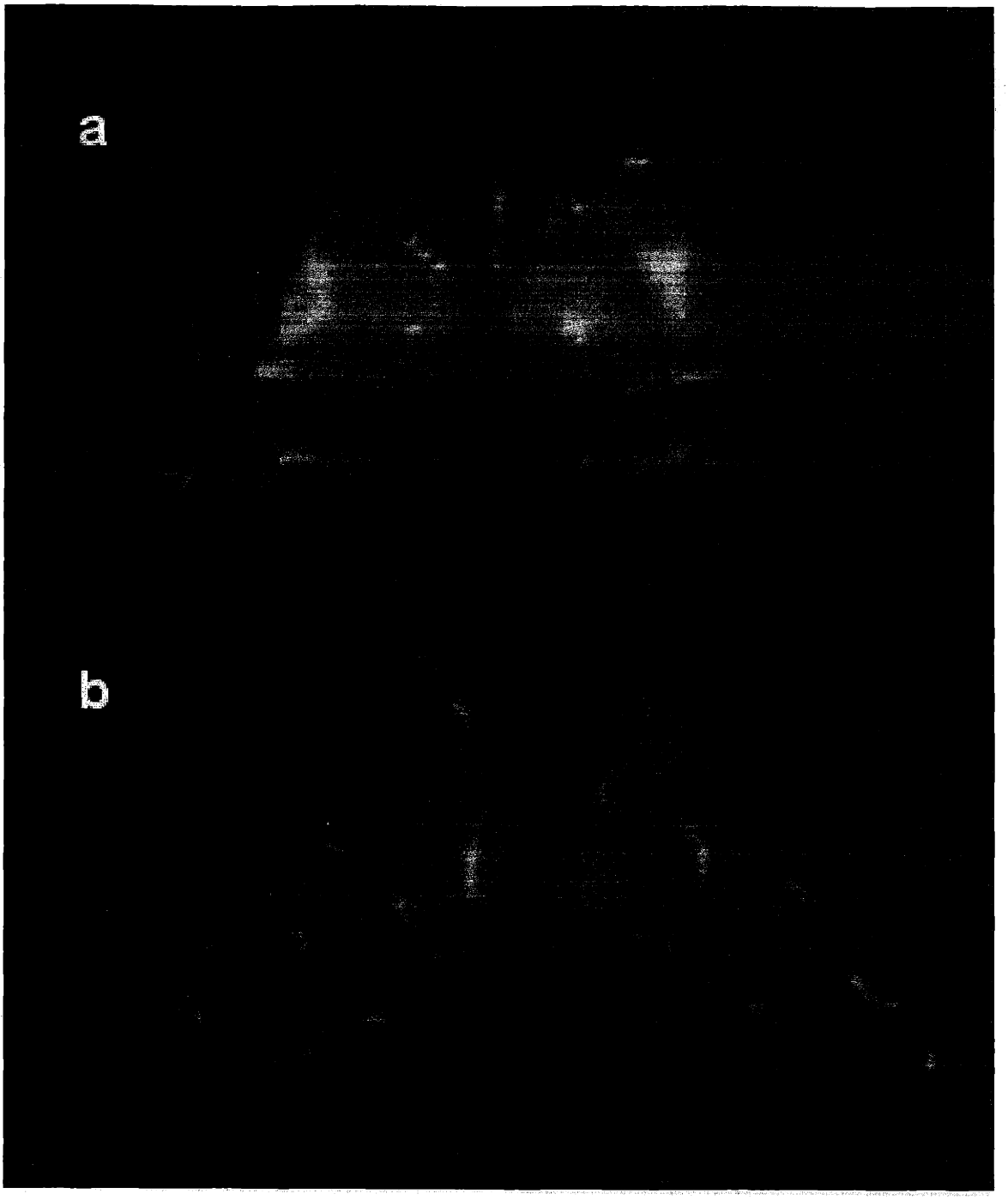

Figure 6-4: Surface renderings of the automatic segmentation result from Fig. 6-3(a). The clusters are color-coded by the principal eigenvector of the mean diffusion tensor within each cluster. The two renderings show a superior view (a) and an inferior view (b), respectively.

(PF) complex was identified. The nuclei which belong to the class of diffuse projecting nuclei regulate the cortical activity by accommodating input from the brain

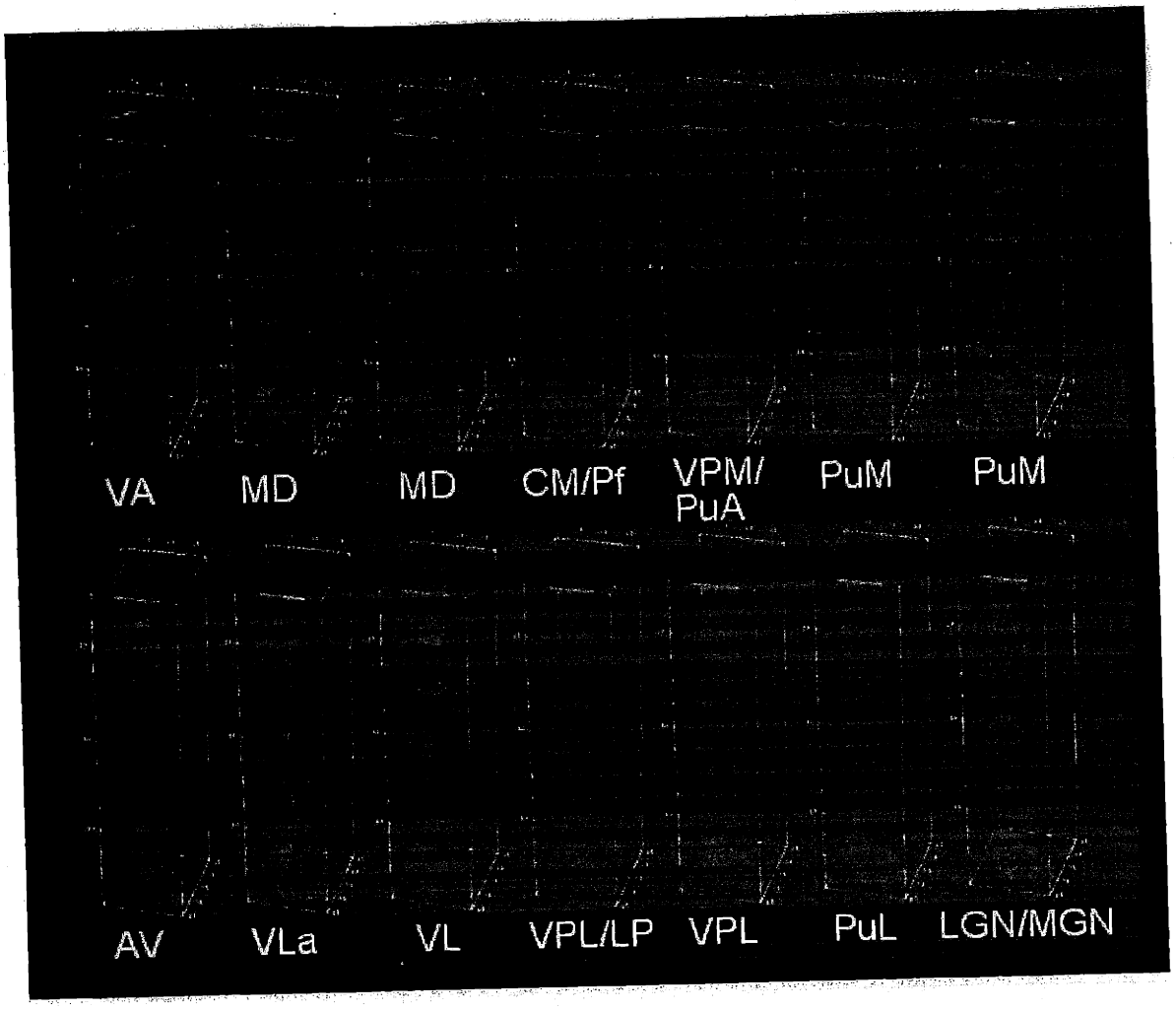

Figure 6-5: Fourteen segmented nuclei for left thalamic hemisphere of subject a. The segmented nucleus is colored by the principal eigenvector and the remainder of the thalamus is colored gray. As for Fig. 6-3, the slices are artificially expanded to facilitate visualization.

stem, basal ganglia, and spinal cord to respectively, the motor cortex and putamen (CM), and the prefrontal cortex and the caudate nucleus (PF). Both nuclei displayed orientations in the superoinferior and slightly anterior direction.

The largest thalamic nuclei, the pulvinar nucleus, facilitates bidirectional connections to the parietal, temporal and occipital association cortex. These projections occur lateral to the optic radiation and spread out to the cortical areas via the posterior thalamic peduncle. In accordance with these projections, the observed primary orientation of the pulvinar was mediolateral, which distinguished it from all other thalamic nuclei.

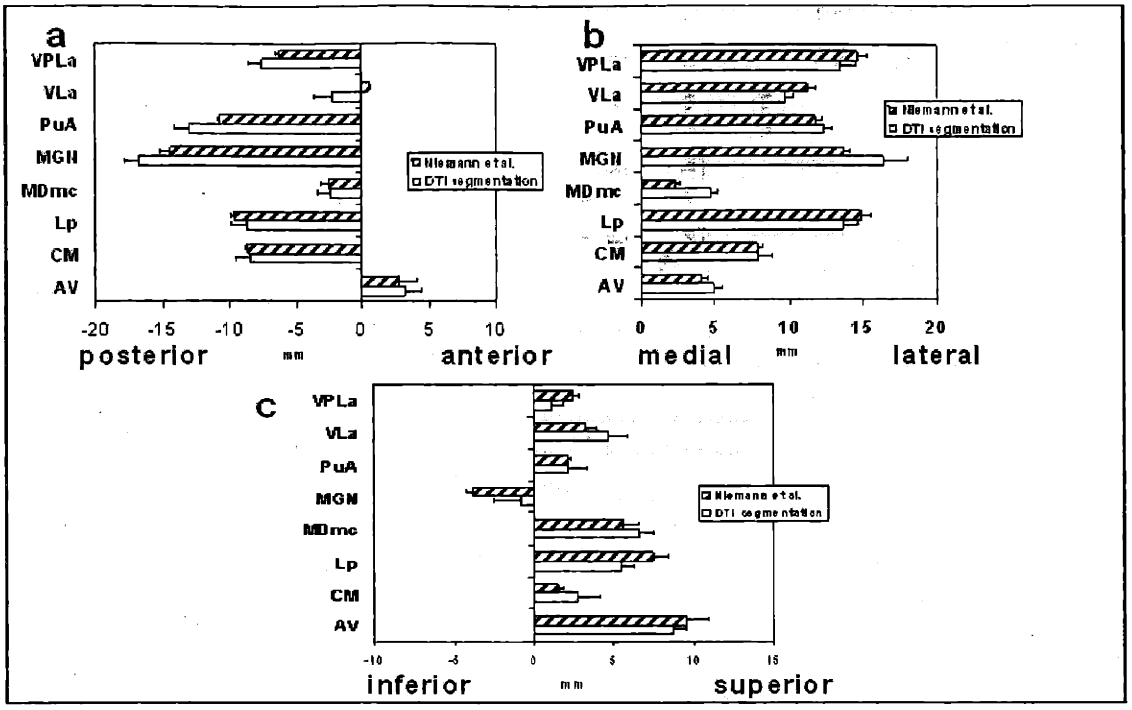

Figure 6-6: Comparison between COM coordinates obtained from Niemann (open bar) and the DTI segmentation (shaded bar). (a) Anteroposterior direction, (b) mediolateral direction and (c) superoinferior direction, respectively.

	Subject 1		Subject 2		Subject 3		Subject 4	
Hemisphere	Right	Left	Right	Left	Right	Left	Right	Left
AV								
MD								
LD								
LP								
VA								
VL								
VLa								
VLp								
VPL								
VPM								
MGN								
LGN								
CM								
Pu								
PuM								
PuA								
PuL								

Table 6.1: Mean fiber orientations of the individually segmented nuclei from each subject. Color representation red mediolateral, green anteroposterior and blue superoinferior. If several classes were assigned to one nucleus, the nucleus box shows multiple colors.

Principal Nucleus/nuclei	*Functional class*	*Major cerebral outputs*	*Cerebral pathway*	*Functions*
Anterior (A)	Relay	Cingulate gyrus, limbic association cortex	Anterior limb of internal capsule, anterior thalamic peduncle	Learning, memory and emotions
Medialdorsal (MD)	Association	Prefrontal association cortex	Anterior limb of internal capsule, anterior thalamic peduncle	Emotions, cognition, learning and memory, affect and foresight
Lateral dorsal (LD)	Relay	Cingulate gyrus	Anterior limb of internal capsule, anterior thalamic peduncle	
Lateral posterior (LP)	Association	Posterior parietal association cortex	Superior thalamic peduncle	Sensory integration
Pulvinar (Pu)	Association	Parietal, temporal, occipital association cortex	Along optic radiation, posterior thalamic peduncle	Sensor integration, perception, language, visual orientation and attention
Ventral anterior (VA)	Relay	Supplementary motor cortex	Genu and Posterior limb of internal capsule, superior thalamic peduncle	Movement planning
Ventrolateral (VL)	Relay	Premotor and primary motor cortex	Genu and Posterior limb of internal capsule, superior thalamic peduncle	Movement planning and control
Ventral posterolateral (VPL)	Relay	Primary somatic sensory cortex	Posterior limb of internal capsule, superior thalamic peduncle	In the body: Touch, limb position sense, pain and temperature sense
Ventral posteromedial (VPM)	Relay	Primary somatosensory cortex, Insula	Posterior limb of internal capsule, superior thalamic peduncle	In the head: Touch, limb position sense, pain and temperature sense
Medial geniculate (MGN)	Relay	Primary auditory cortex, superior temporal gyrus	Sublenticular part of the internal capsule (temporopontine tract), auditory radiation	Hearing
Lateral geniculate (LGN)	Relay	Primary visual cortex, calcarine sulcus	Retrolenticular part of the internal capsule (occipitopontine tract), optic radiation	Vision
Centromedian (CM)	Diffuse projecting	Motor cortex, putamen		Regulation of cortical activity
Parafascicular (PF)	Diffuse projecting	Prefrontal cortex, caudate nucleus		Regulation of cortical activity
Central lateral	Diffuse projecting	Cerebral cortex, basal ganglia		Regulation of cortical activity
Midline nuclei	Diffuse projecting	Cerebral cortex, basal forebrain, allocortex		Regulation of forebrain neuronal excitability
Reticular nucleus		Thalamus	Inhibitory	Regulation of thalamic neuronal activity

Table 6.2: Known thalamic output pathways. Thalamic nuclei with their specific output projections and cortical target areas.

6.6 Discussion

Using DTI we were able to identify and automatically segment the major nuclei of the thalamus. The diffusion tensor segmentation results agreed strongly with a previously published histological study conducted by Niemann et al. (31) for the AV, CM/Pf and LP nuclei. For example, the COM coordinates for the AV nucleus obtained from the automatic segmentation procedure agreed with those of the Niemann study at a 0.05 significance level with a p-value of 0.5261. However, the MD and VLa nuclei showed non-significant correlation at the 0.05 significance level. The relatively weaker agreement for these nuclei is most likely due the following factors. The nuclei mentioned above are nuclear complexes which contain the subnuclei reported by Niemann. The COM comparison was performed between these nuclear complexes and the Niemann subnuclei which represents an anatomical discrepancy. For example, Niemann specified the COM for VLa which we compared to the COM for the full VL complex which consists of both VLa and VLp. This is further borne out by the fact that the COM locations for VL and VLa agreed more strongly in the superoinferior direction than in the anteroposterior and mediolateral directions.

The discrepancy may also be due to intersubject variability in the location of the nuclei (3). Moreover, intersubject variability in the overall volume and morphometry of the thalamus may introduce a bias in the scaling correction. Following Niemann the COM coordinates were scaled in all Talairach dimensions by the AC-PC distance in order to reduce the intersubject variability. However, scaling all dimensions by the AC-PC distance will not in general account for the full variability of the thalami. This is reflected, for example, in the stronger agreement in the AP dimension for the COM locations. The error due to intersubject variability can also be appreciated by considering that nuclei closer to the AC-PC plane were more strongly validated than nuclei further from the plane (55).

The difference between the segmented and histological COM coordinates may also be due to the material distortions introduced by extraction and fixation of the tissue for the histology. This point is supported by the stronger agreement between the

thalamic volumes measured here ($7108 \pm 918 mm^3$) and the reported volumes obtained from MRI in living subjects ($8.65 \pm 0.95 cm^3$, (Collins, D.L. et al. Proceedings of Human Brain Mapping pg. 702 (1998))) as opposed to fixed ($6625 mm^3$, Ref. 56) tissue specimens.

Despite the above differences, we were able to reliably segment and validate many of the major nuclei. For example, in all subjects we identified the AV, MD, LP, VA, VL [VLa, VLp], VPL, CM, Pu [PuA, PuM, PuL], LGN, and MGN nuclei from the 14 segmented classes and in three of four subjects the LD and VPM nuclei were also identified. Of these, the nuclei chosen by Niemann et al. for COM analysis (AV, CM, LP, MDmc MGN, PuA, VLa and VPLa, respectively) were successfully validated for all but the MDmc and VLa nuclei. All the segmented nuclei exhibited mean fiber orientations, which were consistent between subjects and correlated with the orientation of their known corticothalamic and thalamocortical projections. In general the anterosuperior portion of the thalamus showed anteroposterior directed fiber populations, the lateral portion showed superoinferior and mediolateral directions and the posterior portion of the thalamus showed mediolateral directions. The orientation of each segmented nucleus varied as a function of the specific cortical target of the nucleus.

To our knowledge, this is the first report of anatomically significant diffusion anisotropy in a human gray matter structure. The observed anisotropy in the thalamus is most likely due to the thalamocortical and corticothalamic projections which are myelinated, and not the shorter, mostly unmyelinated interthalamic, striatal, and brainstem projections. The attribution of the observed anisotropy to the thalamocortical/corticothalamic projections is motivated by the agreement between the observed fiber directions and the directions of these projections. These projections pass through the internal capsule and the corona radiata, from which they detach into the thalamic peduncles in an orderly fashion. Most of the projections connect to the thalamus at the rostral and caudal poles as well as along the dorsal surface. However, based on the present data we cannot rule out the possibility that unmyelinated structures contributed to the observed diffusion anisotropy.

The ability to identify the thalamic nuclei could be of importance for the diagnosis of diseases with thalamic involvement. Of special interest would be long-term effects and possible subsequent reorganizations of the thalamic nuclei in order to adapt to novel environments, as was recently shown to occur in monkeys (57). A combination of diffusion tensor imaging and functional MRI could help elucidate the functional relations within and between the thalamic nuclei.

6.7 Acknowledgments

The authors would like to thank Katja Krabbe for help during the data acquisition and Bruce Fischl for helpful input on the segmentation algorithm. This work was supported partly through NIH grant number 5RO1 NS 38477-02.

This chapter is based on a submitted paper (58) which was written jointly by myself and Dr. Mette Wiegell of the Athinoula A. Martinos Center, Massachusetts General Hospital. Dr. Mette Wiegell made the initial discovery of diffusion anisotropy in the thalamus, formulated the project, collected the data, performed the literature research, and provided the anatomical descriptions. I wrote the clustering algorithm, performed the clustering analysis, conducted all of the statistical tests, and provided all of the visualization.

6.8 References

[1] W.J.A.J. Smeets, K. de Vos, C.W. Pool, K. Zilles, and H.B.M Uylings. 3-D cytoarchitectonic parcellation of the human thalamus: correlation with postmortem MRI. In *Proc. Int. Conf. Functional Mapping of the Human Brain*, page 239, Düsseldorf, Germany, 1999.

[2] A. Morel, M. Magnin, and D. Jeanmonod. Multiarchitectonic and stereotactic atlas fo the human thalamus. *J. Comp. Neurol.*, 387:588–630, 1997.

[3] J.M. Van Buren and R.C. Borke. *Variations and connections of the human thalamus 2.* Springer-Verlag, New York Heidelberg Berlin, 1972.

[4] J.W. Scannell, G.A.P.C. Burns, C.C. Hilgetag, M. A. O'Neil, and M.P. Young. The connectional organization of the cortico-thalamic system of the cat. *Cereb. Cortex*, 9:277–299, 1999.

[5] C.M. Portas, J.M. Goldstein, M.E. Shenton, H.H. Hokama, C.G. Wible, I. Fischer, R. Kikinis, R. Donnino, F.A. Jolesz, and R.W. McCarly. Volumetric evaluation of the thalamus in schizophrenic male patients using magnetic resonance imaging. *Biol. Psych.*, 43:649–659, 1998.

[6] W.G. Stall, H.E. Hulshoff, H. Schnack, A.C. van der Schot, and R.S. Kahn. Partial volume decrease of the thalamus in relatives of patients with schizophrenia. *Am. J. Psych.*, 155:1784–1786, 1998.

[7] M.S. Buchsbaum, W. Byne, E.A. Hazlett, L. Shihabuddin, C.Y. Tang, T-C Wei, M. Haznedar, and L.J. Siever. PET, MRI, and postmortem studies of the thalamus in schizophrenia. In *Proc. Int. Conf. Functional Mapping of the Human Brain*, page 639, Düsseldorf, Germany, 1999.

[8] M.L. Giroux, S.T. Grafton, J.R. Votaw, M.L. DeLong, and J.M Hoffman. Medication related changes in cerebral glucose metabolism in Parkinsons disease. In *Proc. Int. Conf. Functional Mapping of the Human Brain*, page 237, Montreal, Canada, 1998.

[9] S.M. de la Monte, S.E. Wells, E.T. Hedley-Whyte, and J.H. Growdon. Neuropathological distinction between Parkinsons's Dementia and Parkinson's plus Alzheimer's disease. *Ann. Neurol.*, 26:309–320, 1989.

[10] K. Samra, M. Riklan, E. Levita, and I.S. Cooper. Psychological correlates of anatomically verified thalamic lesions in Parkinsonians. *J. Nerv. Ment. Dis.*, 152:96–105, 1971.

[11] T.H. McNeill, S.A. Brown, J.A. Rafols, and I. Shoulson. Atrophy of medium spiny 1 striatal dentrites in advanced Parkinson's disease. *Brain Res.*, 455:148–152, 1988.

[12] J.H. Xuereb, R.H. Perry, J.M Candy, E.K. Perry, E. Marshall, and J.R. Bonham. Nerve cell loss in the thalamus in Alzheimer's disease and Parkinson's disease. *Brain*, 114:1363–1379, 1991.

[13] K.D. Davis, C.L. Kwan, A.P. Crawley, and D.J. Mikulis. Functional MRI study of the thalamic and cortical activations evoked by cutatenous heat, cold and tactile stimuli. *J. Neurophys.*, 80:1533–1546, 1998.

[14] O. Combarros, J. Miró, and J. Berciano. Ageusia associated with thalamic plaque in multiple sclerosis. *Eur. Neurol.*, 34:344–346, 1994.

[15] T. Ogawa, Y. Yoshida nd T. Okudera, K. Noguchi, H. Kado, and K. Uemura. Secondary thalamic degeneration after cerebral infarction in the middle cerebral artery distribution: Evaluation with MRI imaging. *Radiology*, 204:255–262, 1997.

[16] A.L. Tornqvist. Neurosurgery for movement disorders. *J. Neurosci. Nurs.*, 33:79–82, 2001.

[17] W.L. Nowinski. Anatomical targeting in functional neurosurgery by the simultaneous use of multiple Schaltenbrand-Wahren brain atlas microseries. *Stereotact. Funct. Neurosurg.*, 71:103–116, 1998.

[18] T. Otsuki, H. Jokura, K. Takahashi, S. Ishikawa, T. Yoshimoto, M. Kimura, and R. Yoshida nd T. Miyazawa. Stereotactic gamma-thalamotomy with a computerized brain atlas: technical case report. *Neurosurg.*, 35:764–767, 1994.

[19] T.L. Hardy, J.R. Smith, L.R. Brynildson, H.F. Flanigan, J.G. Gray, and D. Spurlock. Magnetic resonance imaging and anatomical atlas mapping for thalamotomy. *Stereotact. Funct. Neurosurg.*, 58:30–32, 1992.

[20] R.R. Tasker, J.O. Dostrovsky, and E.J. Dolan. Computerized tomography (CT) is just as accuarte as ventriculography for functional sterotactic thalamotomy. *Stereotact. Funct. Neurosurg.*, 57:157–166, 1991.

[21] K. Rubia, T. Russell, E.T. Bullmore, W. Soni, M.J. Brammer, A. Simmons, E. Taylor, C. Andrew, V. Giampietro, and T. Sharma. An fMRI study of reduced left prefrontal activation in schizophrenia during normal inhibitory function. *Schizophr. Res.*, 52:47–55, 2001.

[22] S.L. Rauch, P.J. Whalen, T. Curran, L.M. Shin, B.J. Coffey, C.R. Savage, S.C. McInerney, L. Baer, and M.A. Jenike. Probing striato-thalamic function in obsessive-compulsive disorder and Tourette's syndrome using neuroimaging methods. *Adv. Neurol.*, 85:207–224, 2001.

[23] S. Heckers, T. Curran, D. Goff, S.L. Rauch, A.J. Fischman, N.M Alpert, and D.L. Schacter. Abnormalities in the thalamus and prefrontal cortex during episodic object recognition in schizophrenia. *Biol. Psychiatry*, 48:651–657, 2000.

[24] P. Vuilleumier, C. Chicherio, F. Assal, S. Schwartz, D. Slosman, and T. Landis. Functional neuroanatomical correlates of husterical sensorimotor loss. *Brain*, 124:1077–1090, 2001.

[25] M. Blinkenberg, K. Rune, C.V. Jensen, M. Ranvnborg, S. Kyllingsbaek, S. Holm, O.B. Paulson, and P.S. Sorensen. Cortical cerebral metabolism correlates with MRI lesion load and cognitive dysfunction in MS. *Neurology*, 54:558–564, 2000.

[26] H. Volz, C. Gaser, F. Hager, R. Rzanny, J. Ponisch, H. Mentzel, W. A. Kaiser, and H. Sauer. Decreased frontal activation in schizophrenics during stimulation with the continuous performance test–a functional magnetic resonance imaging study. *Eur. Psychiatry*, 14:17–24, 1999.

[27] V.A. Magnotta, S. Godl, N.C. Andreasen, J.C. Ehrhardt, and W.T. Yuh. Visualization of subthalamic nuclei with cortex attenuated inversion recovery MR imaging. *Neuroimage*, 11:341–346, 2000.

[28] C.J. Holmes, R. Hoge, L. Collins, R. Woods, A. W. Toga, and A. C. Evans. Enhancement of MR images using registration for signal averaging. *J. Comput. Assist. Tomogr.*, 22:324–333, 1998.

[29] M.R. Wiegell, H.B.W. Larsson, and V.J. Wedeen. Diffusion tensor MRI of the thalamus: differentiation of nuclei by their projections. In *Proc. Int. Soc. Magn. Reson. Med.*, volume 7, page 934, Philadelphia, Pennsylvania, 1999.

[30] M.R. Wiegell, D.S Tuch, H.B.W. Larsson, and V.J. Wedeen. Automatic identification of thalamic nuclei from DTI. In *Proc. Int. Conf. Functional Mapping of the Human Brain*, volume 6, Paris, France, 2000.

[31] K. Niemann, V.R. Mennicken, D. Jeanmonod, and A. Morel. The Morel stereotactic atlas of the human thalamus: atlas-to-MR registration of internally consistent canonical model. *Neuroimage*, 12:601–616, 2000.

[32] J.J. Neil, S.I. Shiran, R. C. McKinstry, G.L. Schefft, A.Z. Snyder, C. R. Almli, E. Akbudak, J. A. Aronovitz, J.P. Miller, B.C.P. Lee, and T. E. Conturo. Normal brain in human newborns: apparent diffusion coefficient and diffusion anisotropy measured by using diffusion tensor MR imaging. *Radiology*, 209:57–66, 1998.

[33] P.S. Hüppi, S.E. Maier, S. Peled, G.P. Zientara, P.D. Barnes, F. A. Jolesz, and J.J. Volpe. Mircrostructural development of human newborn cerebral white matter assessed in vivo by diffusion tensor magnetic resonance imaging. *Pediatr. Res.*, 44:584–590, 1998.

[34] P.J. Basser and C. Pierpaoli. Microstructural and physiological features of tissues elucidated by quantitative-diffusion-tensor MRI. *J. Magn. Reson. B*, 111:209–211, 1996.

[35] K.O. Lim, M. Hedehus, M. Moseley, A. de Crespigny, E.V. Sullivan, and A. Pfefferbaum. Compromised white matter tract integrity in schizophrenia inferred from diffusion tensor imaging. *Arch. Gen. Psych.*, 56:367–374, 1999.

[36] J.S. Shimony, R.C. McKinstry, E. Akbudak, J.A. Aornovitz, A. Z. Snyder, N. F. Lori, and T. E Conturo. Quantitative diffusion-tensor anisotropy brain MR imaging: Normative human data and anatomic analysis. *Radiology*, 212:770–784, 1999.

[37] D.K. Jones, A. Simmons, S.C.R. Williams, and M. A. Horsfield. Non-invasive assessment of axonal fiber connectivity in the human brain via diffusion tensor MRI. *Magn. Reson. Med.*, 42:37–41, 1999.

[38] A. Virta, A. Barnett, and C. Pierpaoli. Visualizing and characterizing white matter fiber structure and architecture in the human pyramidal tract using diffusion tensor MRI. *Magn. Resom. Imag.*, 17:1121–1133, 1999.

[39] C. Pierpaoli and P.J. Basser. Toward a quantitative assessment of diffusion anisotropy. *Magn. Reson. Med.*, 36:893–906, 1996.

[40] G.G. Cleveland, D.C. Chang, and C.F. Hazlewood. Nuclear magnetic resonance measurements of skeletal muscle. Anisotropy of the diffusion coefficient of the intracellular water. *Biophys. J.*, 16:1043–1053, 1976.

[41] P.J. Basser, J. Mattiello, and D. Le Bihan. MR diffusion tensor spectroscopy and imaging. *Biophys. J.*, 66:259–267, 1994.

[42] T.G. Reese, R.M. Weisskoff, R.N. Smith, B.R. Rosen, R.E. Dinsmore, and V.J. Wedeen. Imaging myocardial fiber architecture in vivo with magnetic resonance. *Magn. Reson. Med.*, 34:786–791, 1995.

[43] L. Garrido, V.J. Wedeen, K.K. Kwong, U.M. Spencer, and H.L. Kantor. Anisotropy of water diffusion in the myocardium of the rat. *Circ. Res.*, 74:789–793, 1994.

[44] M.R. Wiegell, H.B.W. Larsson, and V.J. Wedeen. Fiber crossing in human brain depicted with diffusion tensor MR imaging. *Radiology*, 217:897–903, 2000.

[45] I. Vorísek and E. Syková. Evolution of anisotropic diffusion in the developing rat corpus callosum. *J. Neurophys.*, 78:912–919, 1997.

[46] D.M. Wimberger, T.P. Roberts, A.J. Barkovich, L. M. Prayer, M.E. Moseley, and J. Kucharczyk. Identification of "premyelination" by diffusion weighted MRI. *J. Comput. Assist. Tomogr.*, 19:28–33, 1995.

[47] H. Sakuma, Y. Nomura, K. Takeda, T. Tagami, T. Nakagawa, Y. Tamagawa, Y. Ishii, and T. Tsukamoto. Adult and neonatal human brain: diffusional anisotropy and myelination with diffusion-weighted MR imaging. *Radiology*, 180:229–233, 1991.

[48] M.A. Rutherford, F.M. Cowan, A.Y. Manzur, L.M.S. Dubowitz, J.M. Pennock, J.V. Hajnal, I. R. Young, and G.M. Bydder. MR imaging of anisotropically restricted diffusion in the brain of neonates and infants. *J. Comput. Assist. Tomogr.*, 15:188–198, 1991.

[49] K. Takeda, Y. Nomura, H. Sakuma, T. Tagami, Y. Okuda, and T. Nakagawa. MR assessments of normal brain development in neonates and infants: comparative study of T1- and diffusion-weighted images. *J. Comput. Assist. Tomogr.*, 21:1–7, 1997.

[50] H. Duvernoy. *The human brain. Surface, three-dimensional sectional anatomy and MRI.* Springer-Verlag, Wien New York, 1991.

[51] C.M. Bishop. *Neural networks for pattern recognition.* Clarendon, Oxford, 1995.

[52] J. Mattiello, P.J. Basser, and D. Le Bihan. The b matrix in diffusion tensor echo-planar imaging. *Magn. Reson. Med.*, 37:292–300, 1997.

[53] S. Peled, H. Gudbjartsson, C-F. Westin, R. Kikinis, and F.A. Jolesz. Magnetic resonance imaging shows orientation and asymmetry of white matter fiber tracts. *Brain Res.*, 780:27–33, 1998.

[54] N. Makris, A. J. Worth, A. G. Sorensen, G. M. Papadimitriou, O. Wu, T. G. Reese, V. Wedeen, T. Davis, J. W. Stakes, V. S. Caviness, E. Kaplan, B. Rosen, D. N. Pandya, and D. N. Kennedy. Morphometry of in vivo human white matter association pathways with diffusion-weighted magnetic resonance imaging. *Ann. Neurol.*, 42:951–962, 1997.

[55] J. Talairach, M. David, P. Tournoux, H. Corredor, and T. Kvasina. *Atlas d'anatomie stéréotaxique. Repérage radiologique indirect des noyaux gris centraux, des régions mésencéphalo-sous-optique et hypothalamique de l'homme.* Masson & Cie, Paris, 1957.

[56] K. Niemann and I. van Nieuwenhofen. One atlas - three anatomies: Relationships of the Schaltenbrand and Wahren microscopic data. *Acta Neurchir. (Wien)*, 141:1025–1038, 1999.

[57] E.G. Jones and T.P. Pons. Thalamic and brainstem contributions to large-scale plasticity of primate somatosensory cortex. *Science*, 282:1121–1125, 1998.

[58] M.R. Wiegell, D.S. Tuch, H.B.W. Larsson, and V.J. Wedeen. Automatic segmentation of thalamic nuclei from diffusion tensor MRI. 2001 (submitted).

Chapter 7

Multi-Tensor Imaging

"Enter several strange shapes, bringing in a banquet; and dance about it with gentle actions of salutation; and, inviting the King, etc., to eat, they depart."

William Shakespeare, *The Tempest*

7.1 Preface

Magnetic resonance diffusion tensor imaging (DTI) can resolve the dominant white matter fiber orientation within a voxel provided that the fibers are strongly aligned. However, a given voxel may contain a distribution of fiber orientations due to, for example, fiber crossing, splaying, or twisting within the voxel. Such intravoxel orientational heterogeneity is irresolvable by DTI due to the assumption implicit to the tensor model of a single diffusion maximum per voxel. Here, we sought to test whether a geodesic, high b-value diffusion gradient sampling scheme employing on the order of a hundred gradient directions could resolve multiple fiber orientations within a voxel. In regions of fiber crossing the diffusion signal exhibited multiple significant local maxima/minima as a function of diffusion gradient orientation, indicating the presence of multiple intravoxel fiber orientations. The standard tensor reconstruction was unsuitable given the apparent multi-modal character of the diffusion signal, so rather the signal was modeled by a discrete mixture of Gaussian diffusion processes in slow exchange, and the underlying tensors were solved for using a gradient

descent scheme. The multi-tensor reconstruction resolved multiple intravoxel fiber populations corresponding to known fiber anatomy.

The present chapter and the chapters following represent a transition from the tensor model which we employed in Chaps. 5 and 6 to a more general diffusion paradigm. This transition will be fully realized in the next chapter (Chap. 8) where we introduce the diffusion spectrum imaging method, a completely model-independent approach to diffusion imaging. Given that the two previous chapters were based on the tensor model which we now seek to dismantle it is reasonable to ask what the domain of validity of the tensor model truly is.

Recall from Chap. 3 that the tensor model, which is synonymous with the Gaussian model, represents a low-spatial frequency approximation to the true diffusion function. Specifically, the tensor model is exact up to third cumulant level in spatial frequency. However, when we wish to describe more complex phenomena such as intra-voxel fiber crossing it is necessary to image the entire diffusion function and not simply its Gaussian best-fit. The tensor results from the previous chapters should thus be viewed as based on a coarse spatial frequency approximation to the true diffusion function which we seek to resolve more fully in the following two chapters.

7.2 Introduction

Tissues with regularly ordered microstructure such as skeletal muscle, spine, tongue, heart, and cerebral white matter exhibit anisotropic (that is, directionally-dependent) water diffusion due to the preferred orientation of the diffusion compartments in the tissue (1–7). The direction of preferred diffusion, and hence the direction of preferred orientation in the tissue, can be resolved with a method called magnetic resonance diffusion tensor imaging (DTI) (2) which measures the apparent water self-diffusion tensor under the assumption of Gaussian diffusion. Based on the eigenstructure of the measured diffusion tensor it is possible to infer the orientation of the diffusion compartments within the voxel so that, for example, the major eigenvector of the diffusion tensor parallels the mean fiber orientation (2), and the minor eigenvector

the normal to the mean plane of fiber dispersion (8).

Notwithstanding the success of DTI for resolving the mean fiber orientation in tissue, the tensor model is incapable of resolving multiple fiber orientations within an individual voxel. This shortcoming of the tensor model stems from the fact that the tensor possesses only a single orientational maximum, i.e., the major eigenvalue of the diffusion tensor (9,10). At the millimeter-scale resolution typical of DTI the volume of cerebral white matter containing such intravoxel orientational heterogeneity (IVOH) may be considerable given the widespread divergence and convergence of fascicles (11, 12). The abundance of IVOH at the millimeter scale can be further appreciated by considering the ubiquity of oblate (pancake-shaped) diffusion tensors in DTI, a hypothesized indicator of IVOH (7, 8).

Given the obstacle IVOH, particularly fiber crossing, poses to white matter tractography algorithms (13–15) we sought to determine whether high angular resolution, high b-value diffusion gradient sampling could resolve such heterogeneity (9). High b-values were employed because at the lower b-values conventionally employed by DTI there is insufficient contrast between the fast diffusion component of one fiber and the slow diffusion component of another fiber to effectively resolve the two fibers (10). Using high angular resolution, high b-value diffusion gradient sampling we were able to detect diffusion signals with multiple, discrete maxima/minima as a function of gradient orientation, indicating the presence of multiple underlying fiber populations. In order to resolve the underlying fiber orientations, the diffusion signal was modeled as arising from a discrete mixture of Gaussian diffusion processes in slow exchange (a mixture of tensors). The distribution of tensors within each voxel was solved for using a gradient descent algorithm, revealing multiple intravoxel fiber orientations corresponding to known fiber anatomy, and consistent with the neighboring fiber anatomy.

7.3 Model

Assuming Gaussian diffusion, the diffusion signal from a single compartment is given by the tensorial Stejskal-Tanner relation

$$E(\mathbf{q}_k) = \exp\left(-\mathbf{q}_k^T \mathbf{D} \mathbf{q}_k \tau\right) \tag{7.1}$$

where $E(\mathbf{q}_k)$ is the normalized diffusion signal magnitude for the diffusion gradient wave-vector $\mathbf{q}_k = \gamma\delta\mathbf{g}_k$, γ is the gyromagnetic ratio, δ is the diffusion gradient duration, $\mathbf{g}_k$ is the kth diffusion gradient, τ is the effective diffusion time, and $\mathbf{D}$ is the apparent diffusion tensor (16). To model multiple compartments, if we assume that (i) the inhomogeneity consists of a discrete number of homogeneous regions, (ii) the regions are in slow exchange, i.e., separated by a distance much greater than the diffusion mixing length, and (iii) the diffusion within each region is Gaussian, i.e., fully described by a tensor, then we can express the diffusion function as a finite mixture of Gaussians

$$E(\mathbf{q}_k) = \sum_j f_j \exp\left(-\mathbf{q}_k^T \mathbf{D}_j \mathbf{q}_k \tau\right) \tag{7.2}$$

where f_j is the apparent volume fraction of the voxel with diffusion tensor $\mathbf{D}_j$. The objective then is to find a a set of n tensors $\{\mathbf{D}_j\}$ and corresponding volume fractions $\{f_j\}$ which best explain the observed diffusion signal. The Gaussian mixture formulation is convenient because it is capable of describing IVOH and retains much of the economy of the tensor model.

The traditional method for solving Gaussian mixture problems of this type is the expectation maximization (EM) algorithm (17, 18). However, the EM algorithm is highly sensitive to local minima and requires a model of the probability that an observed signal arose from a given tensor. Given the limitations of the EM algorithm we employed a gradient descent scheme with multiple restarts to solve the mixture model. The gradient descent algorithm solves for the eigenvectors and volume fractions which give the highest correlation between the predicted and observed diffusion signals. The eigenvalues of the individual tensors can be specified a priori or restricted

to a particular range in order to prevent the algorithm from overfitting with unphysiological (e.g., negative) eigenvalues. The details of the mixture model decomposition algorithm employed in this study are described in the Appendix.

7.4 Experimental Methods

7.4.1 MRI Methods

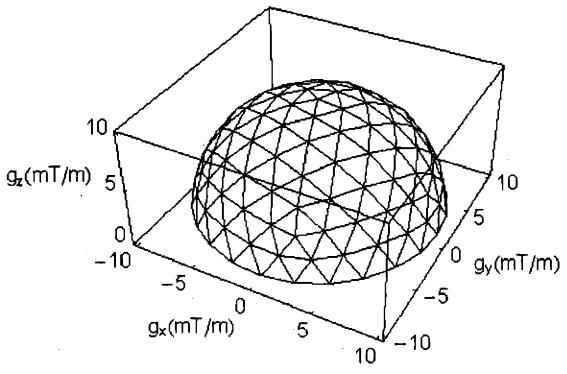

Figure 7-1: Gradient directions for the high angular resolution diffusion experiment. The directions were obtained from the 126 vertices of a 5-fold tessellated icosahedral hemisphere.

Axial diffusion images of a healthy adult male were taken at 3T (GE Signa) with TR/TE/τ = 2200/140/50ms, b = 1.077ms/μ^2, 8 averages, and 3.125 × 3.125 × 3.1mm^3 voxels. The diffusion pulse sequence consisted of a twice-refocused balanced echo with a pair of 180's, the pair situated to minimize Eddy current distortions (5). The gradient ampltidue was g = 10mT/m, and the gradient directions were obtained from the 126 vertices of a 5-fold tessellated icosahedral hemisphere (Fig. 7-1). For each experiment, images with no diffusion weighting were also obtained in order to normalize for non-diffusion signal attenuation. The SNR was ~65 in the unattenuated image and ~35 in the attenuated image.

7.4.2 Multi-Tensor Reconstruction

The data were decomposed with the mixture model described in the Appendix. The mixture model was solved with the conjugate gradient descent algorithm (19) and multiple restarts to prevent the algorithm from settling on local minima. The eigenvalues were specified at $(\lambda_1, \lambda_2, \lambda_3) = (1.5, 0.4, 0.4)\mu^2$/ms. If the predicted diffusion signal from a single tensor agreed with the observed diffusion signal with a Pearson

correlation coefficient of $\rho > 0.95$ then the number of fibers was set to $N = 1$ and $N = 2$ otherwise. The fits for $N = 3$ fiber populations were found to be unstable and hence are not reported. For comparison, single tensor fits were also obtained without the gradient descent algorithm by pseudoinverting the b-matrix as described in Ref. 20.

7.5 Results

7.5.1 Raw Data

Diffusion signals exhibiting multiple maxima/minima as a function of gradient orientation were observed in anatomical regions containing fiber crossing and divergence. Specifically, referring to Fig. 7-2, multi-modal diffusion signals were observed where the callosal fibers, turning into the forceps minor, pass the anterior extension of the anterior limb of the internal capsule. Similarly, multi-modal diffusion was seen where the fibers diverge into the superior temporal gyrus.

7.5.2 Multi-Tensor Reconstruction

The multi-tensor decomposition revealed fiber population mixtures which could not be visualized in the original major eigenvector map (Fig. 7-3) nor in the ADC function polar plots (Fig. 7-2). For example, from the anterior limb, the fibers are shown to curve medially to reach the cingulate gyrus, and, with the callosal radiation, diverge laterally into the inferior frontal gyrus, antero-laterally into the middle frontal gyrus, and anteriorly into the superior frontal gyrus (Fig. 7-3). Additionally, relative to the tensor model, the mixture estimates gave a stronger antero-posterior course to the anterior limb fibers. The reorientation followed from the ability of the mixture model to account for the medio-lateral fiber component in the callosal striations to the inferior frontal gyrus.

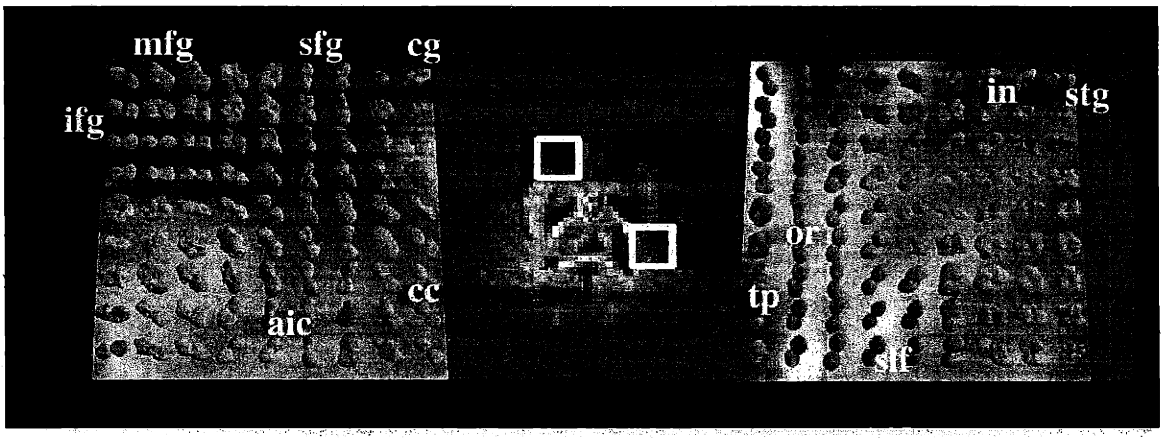

Figure 7-2: Spherical polar plots of the ADC (negative log of the normalized diffusion signal) in the fascicle base of the frontal gyri (left), and the divergence of the optic radiation into the superior temporal gyrus (right). The ADC function was rescaled to $\{0, 1\}$ per voxel in order to maximize the visual angular contrast. *Note that the the peaks of the ADC functions do not give the orientation of the underlying fibers in voxels containing heterogeneity. Multiple peaks simply indicate the* presence *of IVOH.* The color indicates the normalized ADC value according to the scale shown at top-right. In the image at left, note the homogeneous diffusion in the corpus callosum (cc), the anterior extension of the anterior limb of the internal capsule (aic), and the projections to the inferior frontal gyrus (ifg). In contrast, multi-modal behavior is observed where the fibers diverge into the superior (sfg), middle, and inferior (ifg) frontal gyri, where the fibers curve into the cingulum (cg), and where the fibers from the corpus callosum intersect those from the anterior internal capsule. At right, homogeneous diffusion is observed in the optic radiation (or), tapetum (tp), and superior longitudinal fascicle (slf), but heterogeneous diffusion is seen where the fibers diverge into the projections to the superior temporal gyrus (stg) and the insula (in).

Figure 7-3: Comparison of the major eigenvector fields from the single-tensor (a) and two-tensor (b) fits to diffusion signal from the forceps minor (ROI from anterior ROI depicted in Fig. 7-2). The ROI is taken from the same ROI shown in Fig. 7-2. The vectors are oriented in the direction of the major eigenvector of the diffusion tensor within each voxel and are color-coded according to the RGB sphere shown at right with red indicating mediolateral, green anteroposterior and blue superior-inferior. The multi-tensor decomposition (b) shows the intersections of the lateral and callosal striations with the anterior extension of the anterior limb of the internal capsule; and the divergence of fibers to the superior (bright green), middle (drab green), and inferior (red) frontal gyri. Note also the intersection between the antero-lateral directed fibers from the external capsule (bright green), and the superior-inferior directed fibers from the uncinate fascicle (blue)

7.5.3 Comparison to Tensor Model

Recently, it has been proposed that IVOH manifests in DTI in the form of oblate diffusion tensors (4,8), that is, diffusion tensors with the first eigenvalue comparable to the second and both the first and second significantly larger than the third. In order to test this hypothesis we compared the non-Gaussianity of the observed diffusion signal (a measure of disagreement with the tensor model) to the oblateness of the measured diffusion tensor. The diffusion tensor was obtained by pseudo-inverting the b-matrix as described in Ref. 20, and the oblateness of the diffusion tensor was expressed as the difference between the second and third eigenvalues, i.e., $\lambda_2 - \lambda_3$ (8). The non-Gaussianity W was defined as the normalized root-mean-square difference between the experimentally observed diffusion signals $\mathbf{s}_e$ and the signals $\mathbf{s}_D$ predicted from the tensor fit

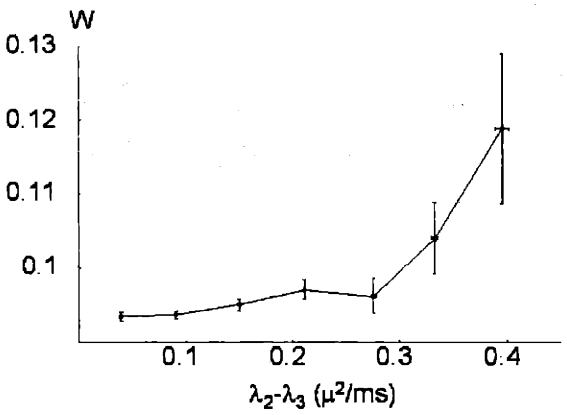

Figure 7-4: Experimental relationship between the error W of the tensor model as defined by Eqn. 7.3 and the oblateness $(\lambda_2 - \lambda_3)$ of the best-fit diffusion tensor. The errors bars are SEM.

$$W = \sqrt{\frac{(\mathbf{s}_D - \mathbf{s}_e)^T(\mathbf{s}_D - \mathbf{s}_e)}{\mathbf{s}_e^T \mathbf{s}_e}}. \tag{7.3}$$

The non-Gaussianity of the diffusion signal was found to increase significantly with the oblateness of the diffusion tensor (Fig. 7-4), providing support for the hypothesis that oblate diffusion tensors in DTI arise from IVOH.

7.6 Discussion

Using high angular resolution, high b-value diffusion imaging we detected diffusion signals with multiple local extrema as a function of diffusion gradient orientation.

The multi-modality was apparent primarily in regions of fiber crossing and splay such as at the divergence of fibers to the frontal gyri. Mixture model decomposition of the diffusion signal using a gradient descent algorithm was able to resolve the underlying fiber populations which corresponded to known anatomy. Moreover, the mixture decomposition gave fiber angle estimates significantly different from those provided by the tensor model, presumably due to the confounding of the latter by partial volume summation of the multiple underlying fiber directions

The observation of multi-modal diffusion in regions of fiber heterogeneity should raise questions about the general validity of the tensor model. The tensor model is adequate to describe the principal fiber direction in well-organized white matter bundles but may give highly misleading results in regions of fiber heterogeneity. For example, two fibers separated by some angle will give rise to a major eigenvector oriented in between the two underlying fiber orientations, a direction inconsistent with either of the underlying fiber orientations. In regions of IVOH, simply taking the negative log of the diffusion signal to obtain the ADC as a function of orientation will not, in general, give a meaningful estimate of the underlying fiber distribution. For example, in Fig. 7-5, the disagreement between the ADC function polar plot and the fiber directions can be readily appreciated.

High b-values were employed in the present experiment in order to provide sufficient IVOH contrast, a requirement recently described in a theoretical report (10). In practice, the discrimination power of the mixture model will depend on the b-values employed for the diffusion experiment. In particular, the sensitivity to IVOH will be low at the relatively low b-values ($b < 0.7\text{ms}/\mu^2$) conventionally employed by DTI because there is insufficient contrast between the low diffusion component from one fiber and the high diffusion component from another fiber with a different orientation (10). The sensitivity to IVOH will increase with increasing b-value but eventually decrease with the associated decrease in SNR. Preliminary data and numerical simulations (unpublished data) suggest that a b-value on the order of $1\text{ms}/\mu^2$) is sufficient for resolving at least two fiber populations, but higher b-values will provide greater heterogeneity sensitivity. In general, the optimal sampling scheme will depend on

the underlying diffusion function and the details of the reconstruction algorithm. A recent study by Frank (21) used spherical harmonics to interpret the diffusion signal obtained by high angular resolution sampling, but did not provide any details on how to invert the signal to obtain the underlying fiber orientations.

The white matter fascicles comprise approximately a quarter of the total human cerebral white matter volume (11, 12). The high angular resolution diffusion imaging method provides a tool for resolving the remaining volume of white matter volume (presumably more by fiber number) characterized by complex arrangements of fibers. The technique promises to directly benefit the white matter tractography problem (15, 22–25) where fiber crossing presents a substantial obstacle (13–15). Specifically, the ability to resolve fiber heterogeneity will allow the tract solutions to navigate through fiber intersections in deep white matter and at the subcortical margin. Further, tract solutions can be initiated in heterogeneous regions as opposed to the current requirement to initiate the tracts in well-organized fascicles with high anisotropy. Lastly, the approach may help characterize selective fiber loss in diseases associated with white matter degeneration.

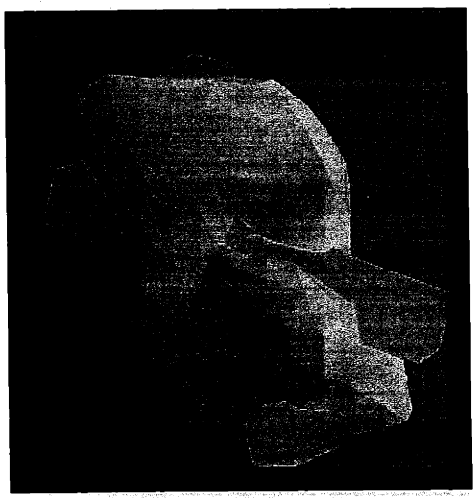

Figure 7-5: Single voxel taken from Figs. 7-2 and 7-3 at the crossing of the callosal striations with the projections to the superior frontal gyrus. The grayscale polar plot shows the negative log of the diffusion signal as function of diffusion gradient orientation (the ADC function) and the cuboids the principal eigenvectors of the two tensors which best fit the diffusion signal. Note the disagreement between the direction of the ADC function and the eigenvector estimates.

7.7 Appendix

The objective of the mixture model decomposition is to find a set of n tensors $\{\mathbf{D}_j\}$ and corresponding volume fractions $\{f_j\}$ (where $j \in [1, n]$) which best fit the ob-

served diffusion signal $E(\mathbf{q}_k)$ which has been sampled over $\{\mathbf{q}_k\}$. In order to encourage physiological solutions, we fix the diffusion tensor eigenvalues to specified values $(\lambda_1, \lambda_2, \lambda_3)$. The error function to be minimized is

$$\chi = \sum_k \left(\hat{E}(\mathbf{q}_k) - E(\mathbf{q}_k)\right)^2 \tag{7.4}$$

$$= \sum_k \left(\sum_j f_j \hat{E}_j(\mathbf{q}_k) - E(\mathbf{q}_k)\right)^2 \tag{7.5}$$

where $\hat{E}(.)$ is the predicted diffusion signal based on the multi-tensor model, $\hat{E}_j(.) = \exp\left(-\mathbf{q}_k^T \mathbf{D}_j \mathbf{q}_k \tau\right)$ (Eqn. 7.2) is the predicted diffusion signal from compartment j, and $E(.)$ is the observed diffusion signal. In order to insure that the volume fractions are properly bounded ($f_j \in [0,1]$) and normalized ($\sum_j f_j = 1$) the volume fractions are calculated through the softmax transformation

$$f_j = \frac{\exp \eta_j}{\sum_i \exp \eta_i}. \tag{7.6}$$

The tensors $\mathbf{D}_j$ are parameterized in terms of the Euler angles α_j^i where $i \in \{1,2,3\}$.

The gradient in the Euler angles is

$$\frac{\partial \chi}{\partial \alpha_j^i} = -\sum_k \left(\hat{E}(\mathbf{q}_k) - E(\mathbf{q}_k)\right) f_j \hat{E}_j(\mathbf{q}_k) \mathbf{q}_k^T \left(\frac{\partial \mathbf{R}_j}{\partial \alpha_j^i} \mathbf{\Lambda}_j \mathbf{R}_j^T + \mathbf{R}_j \mathbf{\Lambda}_j \frac{\partial \mathbf{R}_j^T}{\partial \alpha_j^i}\right) \mathbf{q}_k \tau \tag{7.7}$$

where $\mathbf{R}_j$ is the column matrix of eigenvectors and $\mathbf{\Lambda}_j$ is the diagonal matrix of eigenvalues for diffusion tensor $\mathbf{D}_j$. The gradient in the volume fraction parameters is

$$\frac{\partial \chi}{\partial \eta_j} = \frac{\exp \eta_j}{\left(\sum_i \exp \eta_i\right)^2} \sum_k \left[\left(\hat{E}(\mathbf{q}_k) - E(\mathbf{q}_k)\right) \sum_i (1 - \delta_{ij}) \left(\hat{E}_j(\mathbf{q}_k) - \hat{E}_i(\mathbf{q}_k)\right) \exp \eta_i\right] \tag{7.8}$$

where $\delta_{ij} = 1$ if $i = j$ and 0 if $i \neq j$. The mixture model can then be solved by conventional gradient descent algorithms (19) using the gradients described above.

This chapter is in press (26) and is based on a published abstract (9).

7.8 References

[1] G.G. Cleveland, D.C. Chang, and C.F. Hazlewood. Nuclear magnetic resonance measurements of skeletal muscle. Anisotropy of the diffusion coefficient of the intracellular water. *Biophys. J.*, 16:1043–1053, 1976.

[2] P.J. Basser, J. Mattiello, and D. Le Bihan. MR diffusion tensor spectroscopy and imaging. *Biophys. J.*, 66:259–267, 1994.

[3] M. Ries, R.A. Jones, V. Dousset, and C.T. Moonen. Diffusion tensor MRI of the spinal cord. *Magn. Reson. Med.*, 44:884–892, 2000.

[4] V.J. Wedeen, T.G. Reese, V.J. Napadow, and R.J. Gilbert. Demonstration of primary and secondary muscle fiber architecture of the bovine tongue by diffusion tensor magnetic resonance imaging. *Biophys. J.*, 80:1024–1028, 2001.

[5] T.G. Reese, R.M. Weisskoff, and V.J. Wedeen. Diffusion NMR facilitated by a refocused Eddy-current EPI pulse sequence. In *Proc. Int. Soc. Magn. Reson. Med.*, volume 6, page 663, Sydney, Australia, 1998.

[6] L. Garrido, V.J. Wedeen, K.K. Kwong, U.M. Spencer, and H.L. Kantor. Anisotropy of water diffusion in the myocardium of the rat. *Circ. Res.*, 74:789–793, 1994.

[7] C. Pierpaoli, P. Jezzard, P.J. Basser, A. Barnett, and G. Di Chiro. Diffusion tensor MR imaging of human brain. *Radiology*, 201:637–648, 1996.

[8] M.R. Wiegell, H.B.W. Larsson, and V.J. Wedeen. Fiber crossing in human brain depicted with diffusion tensor MR imaging. *Radiology*, 217:897–903, 2000.

[9] D.S. Tuch, R.M. Weisskoff, J.W. Belliveau, and V.J. Wedeen. High angular resolution diffusion imaging of the human brain. In *Proc. Int. Soc. Magn. Reson. Med.*, volume 7, page 321, Philadelphia, Pennsylvania, 1999.

[10] A.L. Alexander, K.M. Hasan, M. Lazar, J.S. Tsuruda, and D.L. Parker. Analysis of partial volume effects in diffusion-tensor MRI. *Magn. Reson. Med.*, 45:770–780, 2001.

[11] N. Makris, A. J. Worth, A. G. Sorensen, G. M. Papadimitriou, O. Wu, T. G. Reese, V. Wedeen, T. Davis, J. W. Stakes, V. S. Caviness, E. Kaplan, B. Rosen, D. N. Pandya, and D. N. Kennedy. Morphometry of in vivo human white matter association pathways with diffusion-weighted magnetic resonance imaging. *Ann. Neurol.*, 42:951–962, 1997.

[12] N. Makris, J.W. Meyer, J.F. Bates, E.H. Yeterian, D.N. Kennedy, and V. S. Caviness. MRI-based topographic parcellation of human cerebral white matter and nuclei II. Rationale and applications with systematics of cerebral connectivity. *Neuroimage*, 9:18–45, 1999.

[13] C. Poupon, C.A. Clark, V. Frouin, J. Regis, I. Bloch, D. Le Bihan, and J. Mangin. Regularization of diffusion-based direction maps for the tracking of brain white matter fascicles. *Neuroimage*, 12:184–195, 2000.

[14] C. Pierpaoli, A. Barnett, S. Pajevic, R. Chen, L. Penix, A. Virta, and P. Basser. Water diffusion changes in Wallerian degeneration and their dependence on white matter architecture. *Neuroimage*, 13:1174–1185, 2001.

[15] P.J. Basser, D. Pajevic, C. Pierpaoli, J. Duda, and A. Aldroubi. In vivo fiber tractography using DT-MRI data. *Magn. Reson. Med.*, 44:625–632, 2000.

[16] J. Mattiello, P.J. Basser, and D. Le Bihan. The b matrix in diffusion tensor echo-planar imaging. *Magn. Reson. Med.*, 37:292–300, 1997.

[17] A.P. Dempster, N.M. Laird, and D.B. Rubin. Maximum likelihood from incomplete data via the EM algorithm. *J. Royal. Stat. Soc. B*, 39:1–38, 1977.

[18] D.M. Titterington, A.F.M. Smith, and U.E. Makov. *Statistical analysis of finite mixture distributions.* John Wiley, 1985.

[19] W.H. Press, S.A. Teukolsky, W.T. Vetterling, and B.P. Flannery. *Numerical recipes in C: the art of scientific computing.* Cambridge, 1995.

[20] P.J. Basser, J. Mattiello, and D. Le Bihan. Estimation of the effective self-diffusion tensor from the NMR spin echo. *J. Magn. Reson. B*, 103:247–254, 1994.

[21] L. R. Frank. Anisotropy in high angular resolution diffusion-weighted MRI. *Magn. Reson. Med.*, 34:935–939, 2001.

[22] S. Mori, B.J. Crain, V.P. Chacko, and P.C. van Zijl. Three-dimensional tracking of axonal projections in the brain by magnetic resonance imaging. *Ann. Neurol.*, 45:265–269, 1999.

[23] R. Xüe, P.C. van Zijl, B.J. Crain, M. Solaiyappan, and S. Mori. In vivo three-dimensional reconstruction of rat brain axonal projections by diffusion tensor imaging. *Magn. Reson. Med.*, 42:1123–1127, 1999.

[24] V.J. Wedeen, T.L. Davis, R.M. Weisskoff, R. Tootell, B.R. Rosen, and J.W. Belliveau. White matter connectivity explored by MRI. In *Proc. Int. Conf. Functional Mapping of the Human Brain*, volume 1, page 69, Paris, France, 1995.

[25] T.E. Conturo, N.F. Lori, T.S. Cull, E. Akbudak, A.Z. Snyder, J.S. Shimony, R.C. McKinstry, H. Burton, and M.E. Raichle. Tracking neuronal fiber pathways in the living human brain. *Proc. Natl. Acad. Sci. USA*, 96:10422–10427, 1999.

[26] D.S. Tuch, T.G. Reese, M.R. Wiegell, N.G. Makris, J.W. Belliveau, and V.J. Wedeen. High angular resolution diffusion imaging reveals intravoxel white matter fiber heterogeneity. *Magn. Reson. Med.*, 2002 (in press).

Chapter 8

Diffusion Spectrum Imaging

"O place! O form!"

William Shakespeare, *Measure for Measure*

8.1 Preface

In the previous chapter we showed that high angular resolution diffusion imaging was capable of resolving multimodal diffusion behavior in regions of intravoxel fiber crossing. In voxels containing significant non-Gaussianity, we modeled the observed diffusion signal as arising from a finite mixture of Gaussian diffusion processes in slow-exchange. However, as described in the previous chapter, the Gaussian mixture model approach has a number of significant shortcomings including the need for an iterative reconstruction scheme, the possibility of model misspecification, the ability to describe only a discrete distribution of fiber orientations, and the inability to capture non-Gaussian behavior such as may arise from restricted diffusion, diffusion heterogeneity, finite membrane permeability, or surface relaxation.

Here, we present a more general diffusion imaging method termed diffusion spectrum imaging (DSI). DSI is related to the q-space imaging approach which we introduced in Chap. 4 but differs in a number of key respects. As with q-space imaging, DSI does not assume an analytical form for the diffusion process, such as Gaussianity as was assumed by diffusion tensor imaging (DTI) (Chap. 3) or multi-Gaussianity as

was assumed by the tensor mixture modeling approach (Chap. 7). However, the DSI method differs from q-space imaging in a number of experimental and interpretive respects which we explain in detail.

8.2 Abstract

Magnetic resonance imaging of the endogenous water in cerebral white matter can resolve subvoxel histological structure. The water diffusion function is measured with a novel magnetic resonance method called diffusion spectrum imaging. The water displacements are encoded with a set of conventional diffusion-weighted images, and the microscopic three-dimensional diffusion function within each voxel is then reconstructed by Fourier transformation of the modulus of the diffusion signals within each voxel. Diffusion spectrum images of the human brain show correspondence between the directions of enhanced diffusion and the directions of the underlying fiber populations. The diffusion spectrum imaging method allows for resolution of complex fiber structure, such as intravoxel fiber crossing and divergence, previously irresolvable by magnetic resonance imaging.

8.3 Introduction

Magnetic resonance diffusion imaging provides an exquisitely sensitive probe of tissue microstructure. Owing to the microscopic length scale of diffusion in biological tissue, diffusion imaging can reveal histological architecture irresolvable by conventional magnetic resonance imaging methods. However, diffusion imaging methods to date have assumed a simple analytical form for the underlying diffusion process. For example, apparent diffusion coefficient mapping and diffusion tensor imaging (DTI) assume homogeneous, Gaussian diffusion within each voxel. Similarly, finite mixture models such as intra/extracellular exchange models and multi-tensor models assume a discrete mixture of Gaussian diffusion processes in slow exchange. The ability to measure diffusion without recourse to an analytical model would open a broad range

of phenomena for study by diffusion imaging, including intravoxel fiber crossing, restricted diffusion, diffusion compartment morphology, and wall relaxation to name but a few examples.

Model-independent diffusion imaging can be achieved with a technique variously called spin displacement imaging, dynamic NMR microscopy, diffusion displacement imaging, or q-space imaging (1). Q-space imaging, the term used here, measures the microscopic, three-dimensional spin displacement probability density function within each macroscopic volume element (voxel). While q-space imaging has been applied to the study of inanimate materials such as liquid crystals and polymer melts, the technique has not been applied widely *in vivo* due to a number of formidable experimental barriers. The obstacles include contamination to the phase of the echo signal from biological motion, eddy current distortions caused by the high gradients required to obtain sufficiently high spatial resolution of the diffusion function, and the relatively weak gradients available on clinical scanners.

Here, we describe a novel diffusion imaging method termed diffusion spectrum imaging (DSI) which eliminates or minimizes all of the abovementioned barriers to q-space imaging *invivo*. By measuring the microscopic diffusion function within each voxel in a model-independent fashion, DSI can efficiently resolve multiple fiber orientations within a voxel. By contrast, DTI which assumes Gaussian diffusion is only capable of resolving the mean fiber orientation with a voxel. The ability to resolve complex intravoxel fiber structure with DSI opens a whole new domain of microscopic brain anatomy for investigation by magnetic resonance imaging.

8.3.1 Q-Space Imaging

In his seminal paper on the nuclear magnetic resonance (NMR) spin echo, Hahn noted that molecular diffusion in the presence of a magnetic field gradient would reduce the magnitude of the observed echo signal (2). Quantitative measurement of a molecular diffusion coefficient was not made possible however until the introduction of the pulsed gradient spin echo (PGSE) experiment by Stejskal and Tanner (3). Stejskal and Tanner showed that the spin echo magnitude $E(\mathbf{q}, \tau)$ from a PGSE experiment is

directly related to the spin displacement probability density function (PDF) $P(\mathbf{R},\tau)$ by a Fourier relation

$$\begin{aligned} E(\mathbf{q},\tau) &= E_0 \int P(\mathbf{R},\tau) e^{i\mathbf{q}^T\mathbf{R}}\, d\mathbf{R} \\ &= E_0 \mathcal{F}[P(\Delta\mathbf{r})] \end{aligned} \tag{8.1}$$

where $E_0 = E(0,\tau)$ is the signal in the absence of the applied diffusion gradient, $\mathbf{R} = \mathbf{r} - \mathbf{r}'$ is the relative spin displacement from the initial position $\mathbf{r}'$ of the spin at the time of the first gradient to the position $\mathbf{r}$ of the spin at diffusion time τ, $\mathbf{q} = \gamma\delta\mathbf{g}$ is the spin displacement wave vector with γ the gyromagnetic ratio, δ the diffusion gradient duration, and $\mathbf{g}$ the diffusion gradient wave vector (see Chap. 4). The PDF $P(\mathbf{R},\tau)$, which is also referred to as the ensemble-average diffusion propagator (4), expresses the mean probability over the voxel of a relative spin displacement $\mathbf{R}$ in the experimental diffusion time τ. The Fourier relationship between the spin echo magnitude and the PDF allows for direct reconstruction of the PDF by inverse Fourier transform of the diffusion signal with respect to the displacement wave vector

$$\begin{aligned} P(\mathbf{R},\tau) &= E_0^{-1} \int E(\mathbf{q},\tau) e^{-i\mathbf{q}^T\mathbf{R}}\, d\mathbf{q} \\ &= E_0^{-1} \mathcal{F}^{-1}[E(\mathbf{q},\tau)]. \end{aligned} \tag{8.2}$$

The spatial resolution of the diffusion function is given by $2/q_{\max}$, and the field-of-view by $2/\Delta q$ where Δq is the spacing of the reciprocal space sampling grid. From the above relation one can easily derive the return-to-origin (RTO) probability (5,6)

$$P(0,\tau) = \int E(\mathbf{q},\tau)\, d\mathbf{q} \tag{8.3}$$

which reflects the degree of diffusion restriction (Chap. 4). At short diffusion times the RTO probability can be used to derive the surface-to-volume ratio of the pore space (5,6, Chap. 3).

Q-space imaging employs the Fourier relation above to reconstruct the PDF from the diffusion signal. The q-space imaging method has been employed to measure the

characteristic restriction sizes, pore morphology, surface-to-volume ratios, and surface relaxation properties of a broad range of inanimate materials, yet the approach has not been extensively applied to biological tissue *in vivo* because of three significant barriers: the contamination of the phase of the echo by biological motion, the eddy currents induced by large magnetic field gradients, and the relatively weak pulses available on scanners large enough for living animals. In the following, we describe the experimental and conceptual modifications to the q-space imaging experiment which we implemented in order to make q-space imaging feasible *in vivo*.

8.3.2 Modifications to Q-Space Imaging Experiment

Here, we describe how the q-space imaging experiment can be modified to overcome the obstacles previously encountered in implementing the method *in vivo*. The modifications include both experimental changes and interpretive shifts which taken as a whole constitute the method which we refer to as DSI. The following sections specifically describe the necessary modifications and the resulting effects on the observed diffusion function.

8.3.2.1 Twice-Refocused Balanced Echo Sequence

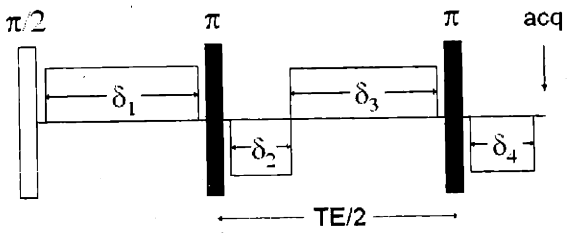

Figure 8-1: Pulse sequence diagram for the effectively constant gradient twice-refocused balanced echo (cgTRBE) experiment. The π-pulse pair can be situated to optimally refocus the eddy currents at acquisition.

Q-space imaging is conventionally performed with a PGSE pulse sequence which consists of a narrow diffusion gradient on each side of the refocusing π-pulse (Fig. 4-1). The diffusion gradients tend however to induce eddy currents in the bore which in turn produce magnetic field gradients which interfere with the imaging gradients (7–10). The interaction of these gradients with the imaging gradients produces deleterious image distortions.

The eddy current distortions are particularly problematic for the strong diffusion gradients required to spatially resolve composite diffusion signals which is the principal aim of this endeavor. The eddy current artifact can be effectively canceled with a twice-refocused balanced echo sequence which consists of a pair of π-pulses separated by TE/2 (Fig. 8-1) (11). Assuming that the eddy current decay is characterized by a single time constant, the π-pulse pair can be positioned to refocus the eddy currents at readout, effectively eliminating the eddy current distortions (11).

The PGSE experiment was further modified by applying an effectively constant gradient ($\Delta \approx \delta$) as opposed to the pulsed gradients more typically used by PGSE experiments. By 'effectively constant' we do not mean that the gradient is held constant, but rather that the gradient is effectively equivalent to a constant gradient when the phase inversions from the π-pulses are taken into account. We refer to this sequence as the constant gradient twice-refocused balanced echo (cgTRBE) experiment (Fig. 8-1). The benefit of the effectively constant gradient is, of course, the ability to achieve significantly stronger wave vectors, and consequently higher spatial resolution of the diffusion function. The effect of the constant gradient on the observed diffusion function is discussed in the following section.

8.3.2.2 Effectively Constant Gradient

The effectively constant gradients employed by the cgTRBE experiment (Fig. 8-1) violate the so-called narrow pulse condition typically cited as a requirement for spin displacement imaging (13). Specifically, it is commonly stated that the diffusion gradients must be sufficiently narrow so that the diffusion during the application of the gradients is negligible. The condition is usually formulated as requiring that the diffusion mixing length associated with the diffusion gradient time must be small relative to a characteristic pore size (1) although much more stringent conditions have been proposed (13).

How does the effectively constant gradient employed the cgTRBE sequence affect the observed diffusion function? For sake of comparison, under narrow pulse condi-

tions the PGSE experiment measures the probability of a spin displacing $\mathbf{R}$ in time Δ. The constant gradient experiment, on the other hand, measures the probability of a spin displacing from its *mean* position over time 0 to TE/2 to its *mean* position over time TE/2 to TE (12) (Fig. 8-2). Following Mitra (12), we will refer to this function as the center-of-mass (COM) propagator. This effect can be spelled out in more detail as follows.

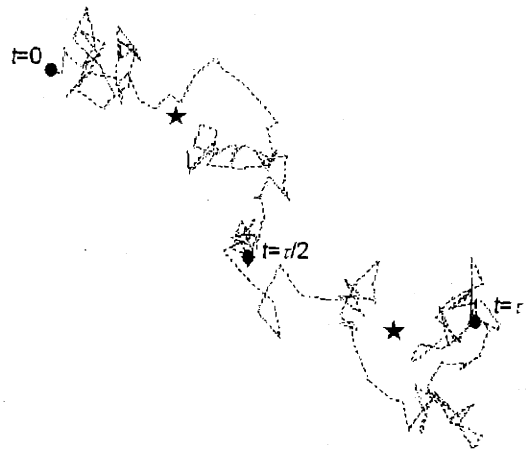

Figure 8-2: Diffusion in a constant magnetic field gradient. The dashed line depicts a sample diffusion path between times $t = 0$ and $t = \tau$ where τ is the diffusion time. A conventional pulsed gradient (Stejskal-Tanner) spin echo experiment with infinitely sharp pulses measures the diffusion from the location of the spin at time $t = 0$ (solid dot) to the location of the spin at time $t = \tau$ (solid dot). The constant gradient experiment measures the diffusion from the mean location (star) between times $t = 0$ and $t = \tau/2$ to the mean location between times $t = \tau/2$ and $t = \tau$. Adopted from Ref. 12.

The COM spin position around a time-point t is

$$\mathbf{r}_{\mathrm{cm}}(t) = \frac{2}{\mathrm{TE}} \int_{t-\mathrm{TE}/4}^{t+\mathrm{TE}/4} \mathbf{r}(t')dt' \qquad (8.4)$$

where $\mathbf{r}(t)$ is the spin position as a function of time. The COM propagator is then simply $P(\mathbf{R}_{\mathrm{cm}}, \tau)$ where

$$\mathbf{R}_{\mathrm{cm}} = \mathbf{r}_{\mathrm{cm}}(\mathrm{TE}/4) - \mathbf{r}_{\mathrm{cm}}(3\mathrm{TE}/4) \qquad (8.5)$$

is the COM relative spin displacement. Note that for Gaussian diffusion, the COM effect is appropriately accounted for by the $\delta/3$ correction to the effective diffusion time (Sec. 4.29). For restricted diffusion, the net effect of the finite pulse width is to produce an apparent diffusion function which is artificially constricted in the direction perpendicular to the restriction barriers (12). If the diffusion is restricted, this might have the beneficial effect of *sharpening* the peaks of the propagator although we do not test this hypothesis here. The principal disadvantage of the finite pulse duration however is that it precludes quantitative, model-independent morphometry of the diffusion space. However, while the effec-

tively constant gradients potentially constrict the diffusion function, they do not produce any rotation of the diffusion function. Hence, the COM propagator can still be characterized accurately in terms of its *orientational* structure. The orientational structure is described by the spin displacement orientation distribution function (ODF) which we define in Sec. 8.3.2.4.

8.3.2.3 Modulus Fourier Transform

Spin displacement imaging of the brain has proven problematic in the past due to the contamination of the phase of the diffusion signal by biological motion which in the brain is principally due to cardiac pulsation (14). Taking the Fourier transform of the *modulus* of the signal, as opposed to that of the full complex signal, removes the phase error, but we need to ask what, if any, information is lost in doing so. We show that for a pure diffusion process the modulus Fourier transform and the complex Fourier transform are equivalent and hence no information is lost in taking the modulus, as opposed to the full complex, Fourier transform. This striking result entails that any ensemble-averaged diffusion function can be perfectly reconstructed from its power spectrum.

We can prove that the modulus Fourier transform and the complex Fourier transform are equivalent by showing that the diffusion signal is real and positive or all wave vectors. That is, in order to show that $E_0^{-1}\mathcal{F}^{-1}[E(\mathbf{q})] = |E_0^{-1}|\mathcal{F}^{-1}[|E(\mathbf{q})|]$ it is sufficient to show that $E(\mathbf{q}) = |E(\mathbf{q})|$ for all $\mathbf{q}$. The reality of the diffusion signal follows easily from the symmetry of the diffusion propagator ($P(\mathbf{R},\tau) = P(-\mathbf{R},\tau)$). We now wish to show that the diffusion signal is positive as well.

While the Bochner theorem informs us that if the charateristic function (equivalent here to the Fourier transform due to symmetry) is positive everywhere then the direct space function is a distribution, the goal here is, conversely, to determine if all ensembley-averaged distributions arising from the diffusion equation have a positive Fourier transform. We begin by noting that the propagator has the spectral

decomposition

$$P(\mathbf{r}, \mathbf{r}', \tau) = \sum_n u_n(\mathbf{r}) u_n(\mathbf{r}') e^{-E_n \tau} \tag{8.6}$$

where the eigenfunctions $\{u_n\}$ are an orthonormal set of solutions to the Helmholtz equation parameterized by the eigenvalues E_n (15, 16). Substituting the spectral decomposition into the diffusion equation

$$\left[\frac{\partial}{\partial \tau} - \nabla(\mathbf{D}(\mathbf{r})\nabla) + \rho(\mathbf{r})\right] P(\mathbf{r}, \mathbf{r}', \tau) = \delta(\mathbf{r} - \mathbf{r}')\delta(\tau) \tag{8.7}$$

gives the eigenvalue equation

$$\left[\nabla(\mathbf{D}(\mathbf{r})\nabla) + E_n\right] u_n(\mathbf{r}) = 0. \tag{8.8}$$

From the above equation we see that since all of the eigenfunctions are real all of the eigenvalues E_n are real as well and hence the propagator is positive definite. The diffusion signal is

$$E(\mathbf{q}, \tau) = E_0 \sum_n |\mathcal{F}[u_n(\mathbf{r}])|^2 e^{-E_n \tau}. \tag{8.9}$$

which is real since all of the eigenvalues E_n are real. Hence, the diffusion signal is equal to its modulus ($E(\mathbf{q}, \tau) = |E(\mathbf{q}, \tau)|$) for all wave vectors. Consequently, *no* information is lost in taking the modulus, as opposed to the full complex, Fourier transform.

It is important to note that the positivity and reality of the echo signal only holds for the *ensemble-average* diffusion function but not generally for the unaveraged diffusion function. For example, let us consider the simple case of a one-dimensional compartment with impermeable walls. At long times, the diffusion function is a boxcar, the Fourier transform of which is a sinc function which is not positive everywhere. However, if we consider the average over all starting positions the diffusion function is a triangle, the auto-correlation of the boxcar, the Fourier transform of which is the sinc-squared function which is positive everywhere. Hence, the averaging of the diffusion signal over the voxel is required to ensure that the echo signal is positive.

The positivity and reality of the echo signal for any pure diffusion process entails that any non-zero phase observed in the signal has a source other than diffusion, and so the diffusion function can be accurately reconstructed as the Fourier transform of the modulus of the echo signal. Using the modulus Fourier transform has additional practical significance since it eliminates phase shifts due to changing eddy current or frequency shifts during the encoding process.

8.3.2.4 Radial Projection Transform

The DSI experiment ultimately yields a six-dimensional image resulting from the three spatial dimensions of the anatomical image plus the three spatial dimensions of the diffusion function. In order to visualize the diffusion function within each voxel, we project the diffusion function on to the sphere by integrating over the radial coordinate of the diffusion function. The transformation is referred to as the radial projection transform and to the resulting function as the spin displacement orientation distribution function (ODF).[1] The ODF representation sacrifices all of the radial information but retains the relevant directional information.

The ODF expresses the probability of a spin displacing into a differential solid angle about a fiber direction $\mathbf{u}$. In the complex materials literature $\mathbf{u}$ is sometimes referred to as the microscopic director, or simply the director. For a given propagator $P(\mathbf{R}, \tau)$ the ODF is obtained via the radial projection

$$\psi(\mathbf{u}) = \int_0^\infty P(\rho\mathbf{u}, \tau)\, d\rho \tag{8.10}$$

where $\mathbf{u}$ is a unit normal vector, ρ is the radial coordinate in the diffusion space coordinate system, and we have dropped the time argument. In practice the integral cannot be taken out to infinity and is rather taken to the linear field-of-view ρ_{max} of the PDF. Note that the COM effect from the constant gradients will change the height and width, but not the position of the peaks on the sphere.

[1]The projection of a Cartesian probability distribution, in this case the diffusion function, on to the sphere is a construction which is commonly encountered in the field of directional statistics (17,18).

The experimental and interpretive modifications described above enable imaging of the ODF within each voxel. We show that such images of the human brain demonstrate correspondence between the orientational maxima of the ODFs and those of the underlying fiber orientation density at each voxel location. In regions of intravoxel orientational heterogeneity, such as regions of fiber crossing or fiber divergence, the ODFs show clear multimodal structur consistent with the underlyin anatomy.

8.4 Methods

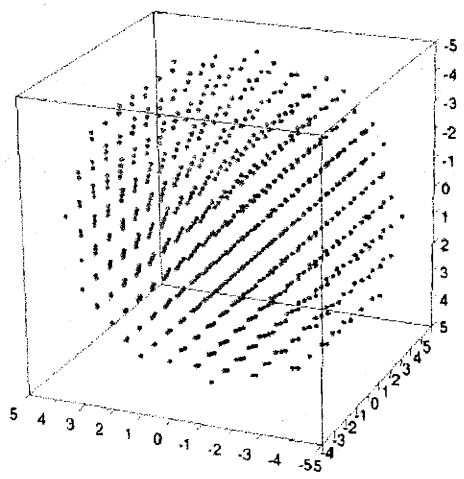

Figure 8-3: Keyhole Cartesian sampling scheme for a $11 \times 11 \times 11$ grid. The scheme contains 691 points. All of the experiments presented here used all of or a subset of the sampling grid shown here.

Diffusion spectrum images were acquired on 3 healthy volunteers (Subjects A-C) and 5 patients (Subjects D-H). The data were acquired at 3T using a single-shot echo-planar MRI acquisition and the cgTRBE sequence describe above. For each experiment, the π-pulse pair was positioned to minimize the eddy currents at readout. The diffusion gradient sampling points were obtained from a three-dimensional keyhole Cartesian grid. The keyhole grid consisted of the points in reciprocal space on a $n \times n \times n$ Cartesian grid which lay within a sphere of diameter n. Fig. 8-3 shows the keyhole sampling scheme for a $11 \times 11 \times 11$ grid. All of the experiments used all of or a subset of the sampling scheme shown in Fig. 8-3. To achieve a desired $q_{\max}$ the grid was scaled linearly in g so that the outermost point had a magnitude of $g_{\max} = 40\text{mT/m}$. The specific sequence parameters and slice prescriptions for each subject are summarized in Table 8.1.

Subject	slice orientation	voxel resolution (mm)	slices	TR/TE/Δ/δ(ms)	$b_{\max}$ (s/mm^2)	$q_{\max}/\Delta q$ (μm^{-1})	q-space grid dimensions	N
A	sagittal	$4 \times 4 \times 4$	8	gated/140/65/60	2.0×10^4	0.67/0.17	$9 \times 9 \times 9$	258
B	coronal	$4 \times 4 \times 4$	3	gated/140/65/60	2.0×10^4	0.67/0.17	$9 \times 9 \times 9$	258
C	axial	$3 \times 3 \times 3$	1	gated/120/55/50	1.7×10^4	0.67/0.13	$11 \times 11 \times 11$	437
D	sagittal	$4 \times 4 \times 4$	9	2700/144/67/62	1.7×10^4	0.66/0.13	$11 \times 11 \times 11$	437
E	coronal	$3.5 \times 3.5 \times 3$	6	2000/144/67/62	1.7×10^4	0.66/0.13	$11 \times 11 \times 11$	587
F	coronal	$3 \times 3 \times 3$	3	1500/144/67/62	1.7×10^4	0.66/0.13	$11 \times 11 \times 11$	691
G	axial	$3 \times 3 \times 3$	3	gated/144/67/62	1.6×10^4	0.66/0.13	$11 \times 11 \times 11$	500
H	axial	$3 \times 3 \times 3$	3	gated/144/67/62	1.6×10^4	0.66/0.13	$11 \times 11 \times 11$	500

Table 8.1: Protocols for DSI experiments. Subjects A-C are healthy volunteers, and D-H are patients. For TR=gated, the acquisition was triggered to 2 R-R cardiac cycles. N is the number of sampling points in the keyhole sampling scheme.

The 5 patient subjects were as follows.

Subject D: 27 year old male scanned 1 year post anterior cingulotomy for obsessive

compulsive disorder (OCD). The patient was successfully treated for OCD by the cingulotomy.

Subject E: 42 year old female scanned one month post resection of a left frontal lobe oligodendroglioma. Patient had recurrent or residual tumor in the contralateral hemisphere.

Subject F: imaged for a temporal lobe tumor.

Subject G: 35 year old female with a right chronic thalamic infarct.

Subject H: 64 year old female with chronic left occipital stroke. Remaining long term symptoms of visual motion perceptual errors.

For subjects A-C,G, and H, the acquisitions were synchronized with late-diastole by ECG trigger to minimize effects of brain motion (14).

For each voxel the diffusion signal values were placed on a $n \times n \times n$ grid according to the points from which the values were sampled. The corners of the grid where no values were obtained due to the keyhole truncation were set to zero. For each voxel the PDF was then reconstructed by taking the three-dimensional fast Fourier transform of the the data grid for that voxel. The ODF for each voxel was calculated by integrating over the radial coordinate (using cubic interpolation) of the PDF. The ODF was evaluated for the $m = 752$ vertices of a 5-fold tesellated dodecahedron. For visualization purposes the ODFs were scaled to $[0, 1]$ within each voxel and displayed as spherical polar plots. The ODF reconstruction scheme is outlined schematically in Fig. 8-4. For sake of comparison we also calculated the diffusion tensor for each voxel using a least-squares fit to the diffusion data (19). For each subject we also calculated the return-to-origin (RTO) probability image as the sum over all the diffusion-weighted images (5, 6).

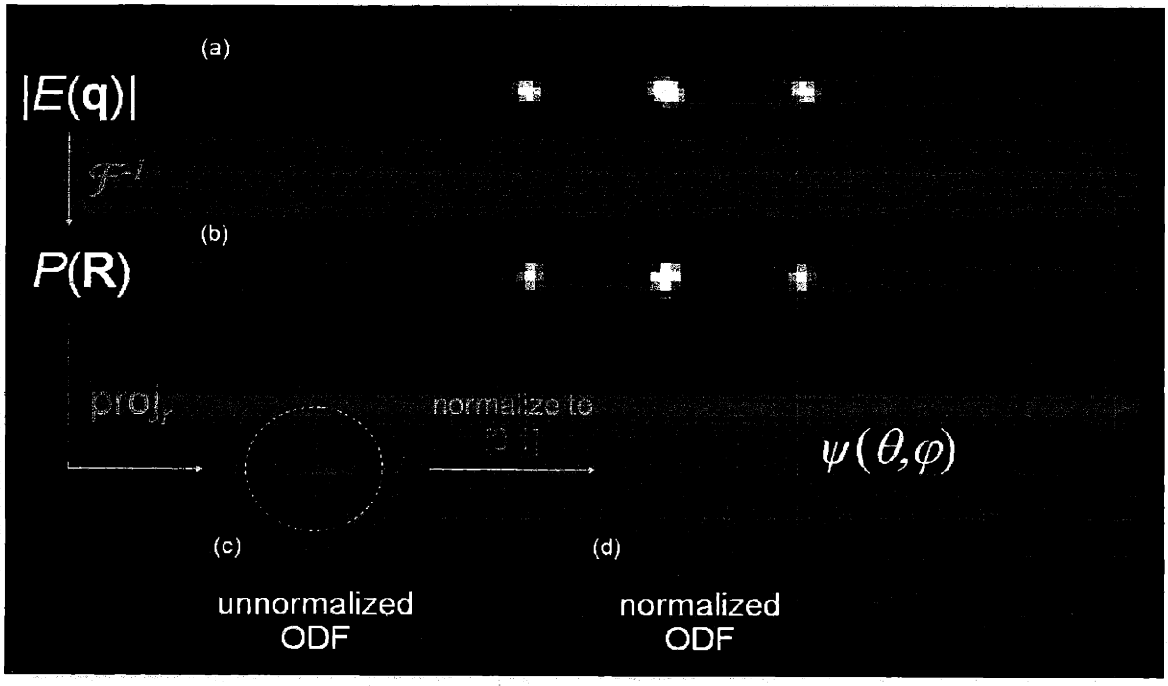

Figure 8-4: Schematic diagram of the ODF reconstruction scheme for a single voxel. Row (a) shows the 'raw' data depicted as two-dimensional sections through the three-dimensional data volume. Three-dimensional fast Fourier transform of the modulus of the the raw data leads to the three-dimensional PDF (b), similarly depicted as two-dimensional sections through the three-dimensional volume. Integrating over the radial coordinate of the PDF (denoted proj_r) gives the unnormalized ODF (c). The color-coding reflects the orientation of the peaks in the lab frame as described in the Results section. Lastly, in order to increase the visual contrast the ODF is normalized to $[0, 1]$ (d).

8.5 Results

8.5.1 Healthy Volunteers

Diffusion spectrum images of the brainstem of a normal volunteer are shown in Figs. 8-5, and 8-6. Fig. 8-5 shows the intersection of cerebellar pontine fibers (cpf) with the corticospinal tract (cst) at the level of the pontine decussation. The cpf are seen to pass through various points of the cst with variable density. In Fig. 8-5, we can also resolve the intersection of the superior cerebellar peduncle (scp) with the cst as the scp fibers join the cst. Fig. 8-6 shows the diffusion propagator from a single voxel at the intersection of the cpf and the cst. The propagator is clearly bimodal, reflecting the diffusion peak from the cst and the diffusion peak from the cpf.

The composite structure of the brainstem can also be seen in Fig. 8-7 which compares a coronal DSI and a DTI from a normal volunteer. In the DSI, bimodal diffusion is clearly seen where the cpf intersect the cst. By comparison the directional estimates provided by DTI are heavily confounded due to the the partial volume averaging of these fiber directions.

The diffusion spectrum images were also able to resolve crossings of more than two fiber populations. For example, Fig. 8-8 shows the intersection of the diverging striations from the corpus callosum (ccs), the corona radiata (cr), and the superior longitudinal fasciculus. We observe a clear three-way crossing where these populations intersect. In comparison, the tensor reconstructions in this region are heavily confounded.

In addition to complex structure in deep white matter intersections, we also observed composite fiber structure at the subcortical margin. Figs. 8-9 and 8-10 show two sagittal slice diffusion spectrum images from motor cortex. In Fig. 8-9 we see the intersection of the superior longitudinal fasciculus (slf) with the ascending corona radiata (cr). The voxels at the subcortical margin also show multimodal behavior consistent with a projection to the cortical surface and a population parallel to the cortical surface, possibly intracortical connections. This multimodal structure can be visualized clearly in Fig. 8-10.

Figure 8-5: Subject A: Two sagittal diffusion spectrum images of the brainstem at the level of the pontine decussation. The two sagittal slices were taken from the ROIs (yellow rectangles) shown in the anatomical images at left. The closest slice is lateral relative to the further slice. The anatomical images and the grayscale background show the RTO probability. The spherical polar plot within each voxel depicts the normalized ODF (the radially projected PDF) within that voxel. The ODFs are colored according to the red-green-blue sphere shown at bottom-left with red indicating mediolateral, green anteroposterior, and blue superoinferior. The brightness of the peaks is also scaled by the height of the peaks. The red fiber population consists of cerebellar pontine fibers (cpf). The blue population is the corticospinal tract (cst), and the bluish-green population is the superior cerebellar peduncle (scp). Note the bimodal diffusion behavior where the cst intersects the cpf, and where the scp joins the cst.

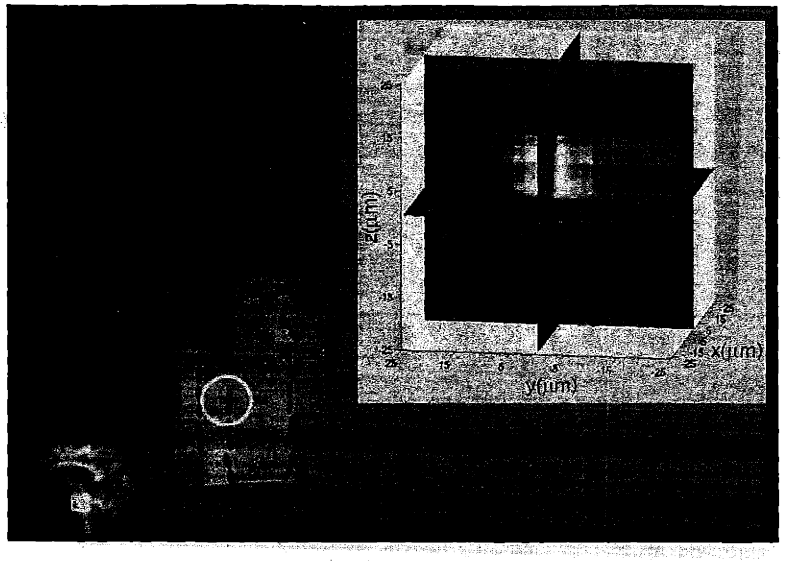

Figure 8-6: Diffusion propagator (top-right) from a single voxel (yellow circle) containing the intersection of the cpf with the cst. The three-dimensional propagator is visualized as three transparent orthogonal cross-sections.

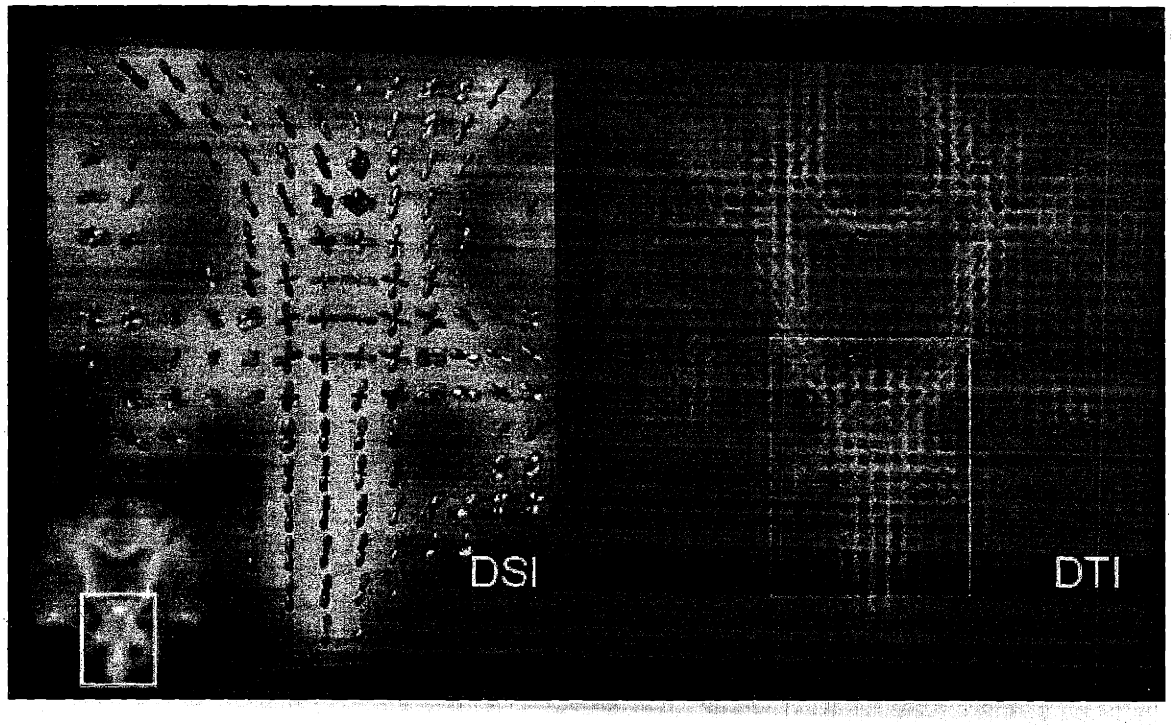

Figure 8-7: Subject B: Comparison of DSI and DTI of the brainstem. The DTI is depicted as a cuboid icon field, with each cuboid scaled and oriented according to the local diffusion tensor eigensystem. The anatomical image at far left is a RTO probability image. The ROI (yellow square from anatomical image and white square from DTI) of the DSI shows the intersection of the cst (blue) with the cpf (red). In comparison the DTI is heavily confounded.

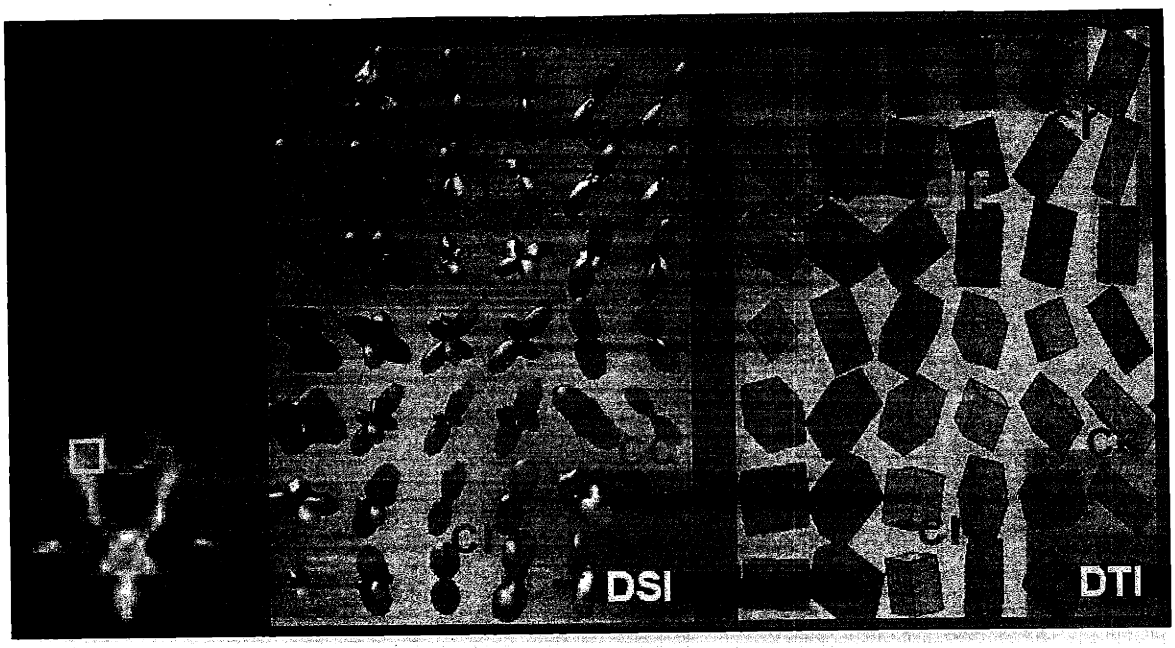

Figure 8-8: Subject B: Comparison of DSI (left) and DTI (right) at the three-way crossing of the striations from the corpus callosum (ccs), the corona radiata (cr), and the superior longitudinal fasciculus (slf). The images were taken from the ROI (yellow square) shown in the RTO probability map at left. Note the strongly confounded fiber estimates from the diffusion tensor reconstruction.

Composite fiber structure at the subcortical margin can also be seen in Fig. 8-11 which shows an axial slice of the occipital pole at 3mm resolution. The green curves demarcate an intermediate zone between the unidirectional deep white matter and the complex subcortical white matter. Peri-sulcal white matter shows bimodal diffusion consistent with intersection of corticofugal fibers and U-fibers transverse to the sulcus, or possibly intracortical connections.

8.5.2 Patients

The DSI of the clinical subjects are shown in Figs. 8-12 through 8-16. In Fig. 8-12 we see selective degeneration of the cingulum in the region of the cingulotomy burn (T2 bright region). The intersecting corpus callosum and corona radiata fibers, by comparison, are relatively intact. Moreover, we observe residually intact cingulum fibers in the region of the burn.

Fig. 8-13 shows DSI of a patient with a resected fronal lobe oligodendroglioma.

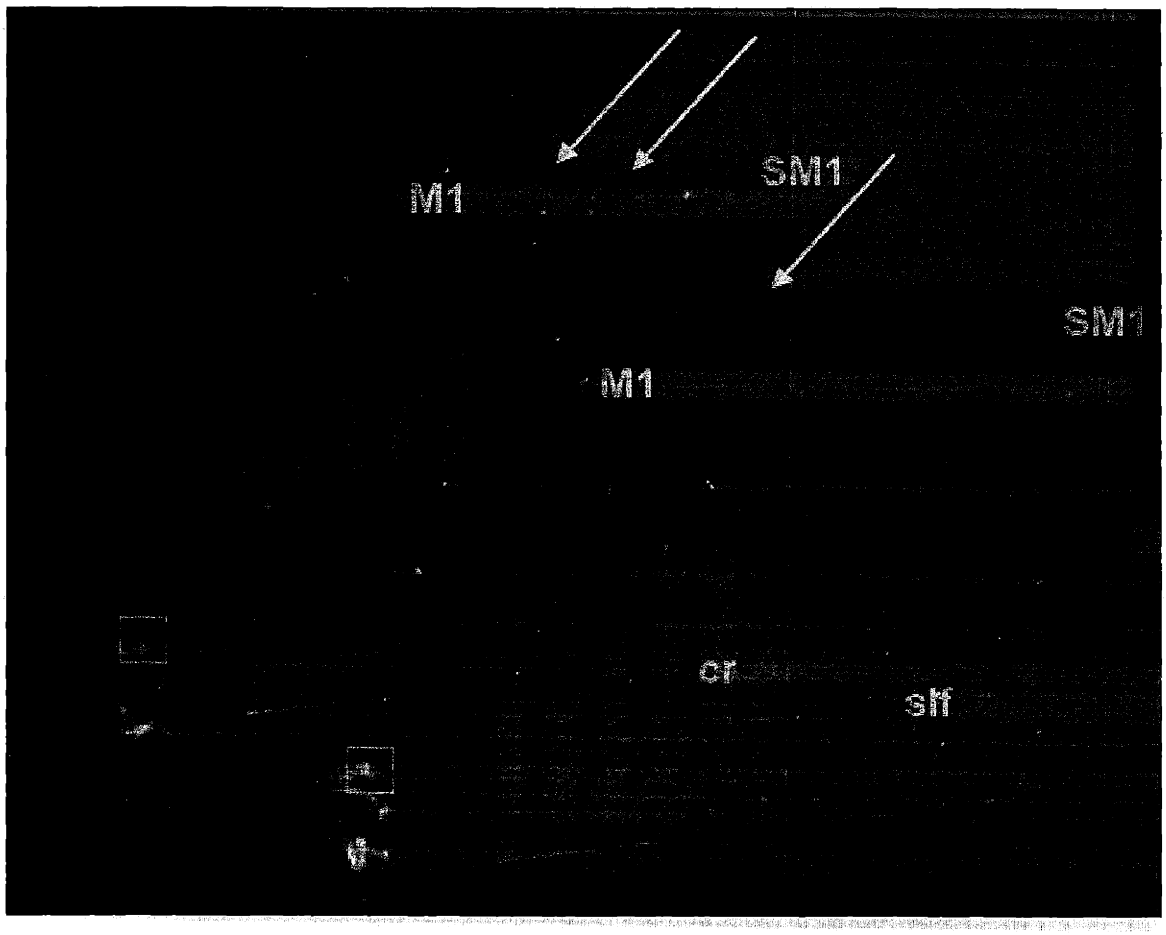

Figure 8-9: Subject A: The closest slice is lateral relative to the further slice. The anatomical images and the grayscale background show the RTO probability. The green fiber population at bottom-right is the superior longitudinal fasciculus (slf) and the blue population is the corona radiata (cr). The cr can be seen to project to primary motor (M1) and primary somatosensory (SM1) cortex. Note the intersection of the slf with the cr at bottom-right. Also note the bimodal diffusion at the cortical surface (yellow arrows).

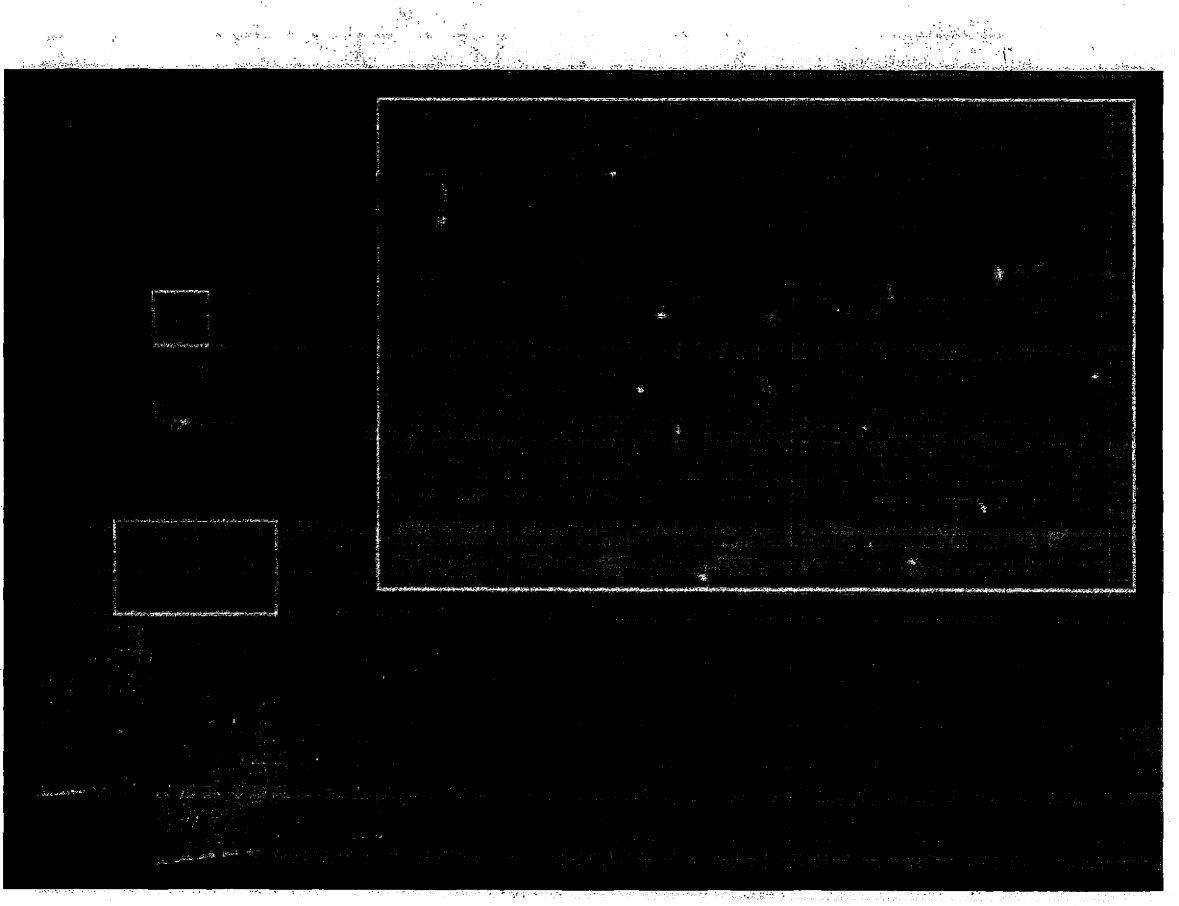

Figure 8-10: Subject A: Zoomed view of a single slice from Fig. 8-9. Note the multimodal diffusion at the cortical surface. The ODFs show a fiber population (blue) consistent with the projections from the cr, and a fiber population (green) oriented approximately parallel to the surface.

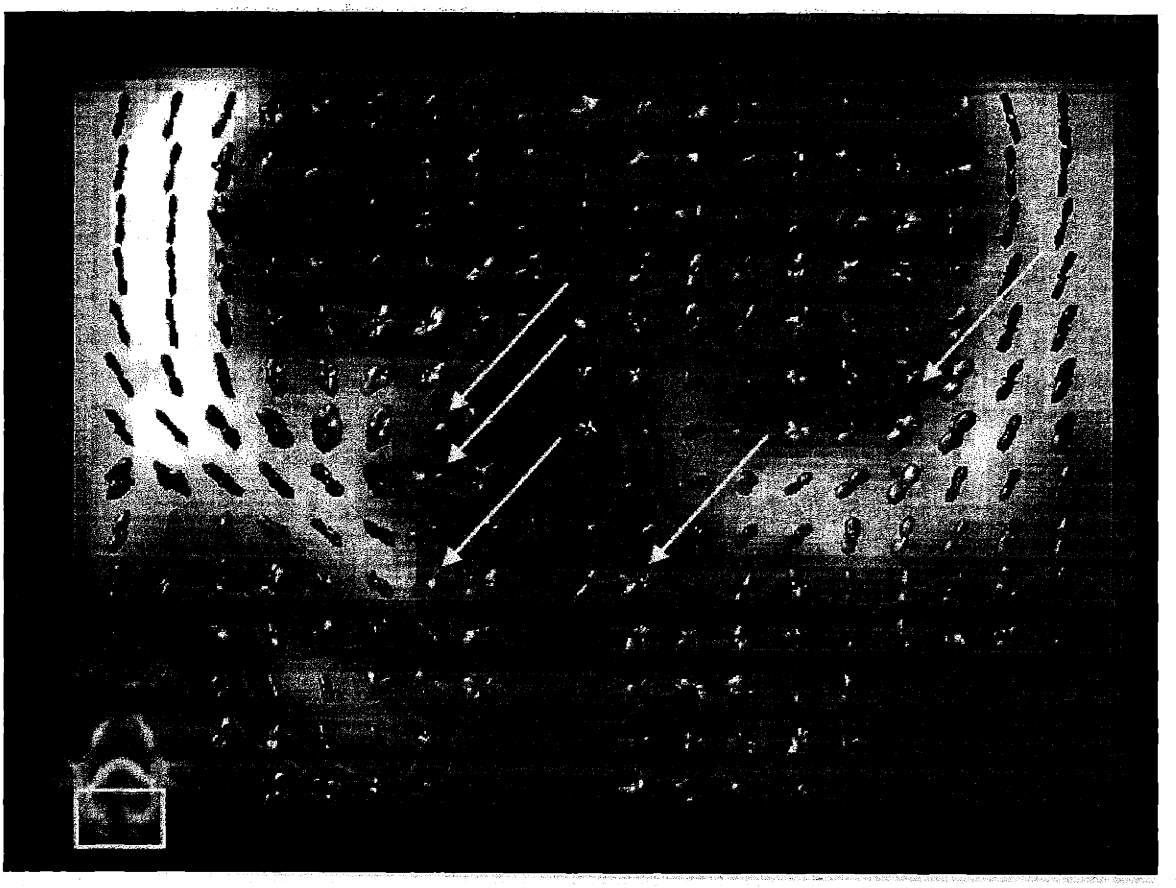

Figure 8-11: Subject C: Axial DSI of the occipital pole. The green curves demarcate an intermediate zone between the unidirectional deep white matter and the complex subcortical white matter. Peri-sulcal white matter show bimodal diffusion (yellow arrows).

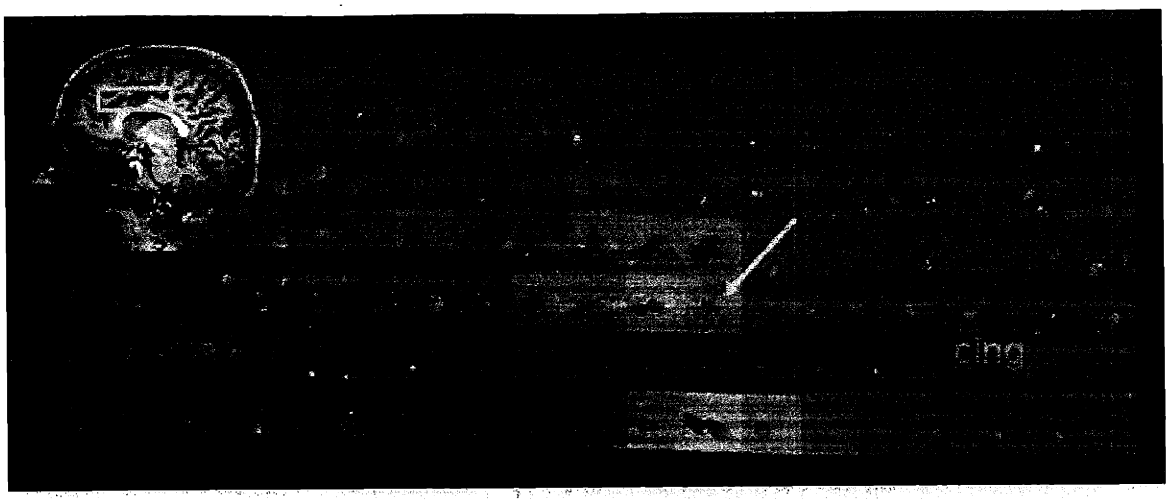

Figure 8-12: Sagittal DSI of patient one year post cingulotomy for OCD. The anatomical image is shown at top-left. The background grayscale image is the T2 image. The cingulum fibers (cing, green) are absent in some voxels (yellow arrow) within the burn (T2 bright region) and also anterior to the burn. The intersecting corpus callosum fibers (cc, red) and corona radiata (cr, blue) are seen to be intact. Residual cingulum fibers are also observed within the cingulotomy burn.

In comparison to the unaffected side which shows a clear intersection of the corpus callosal striations with the corona radiata, the side with the tumor shows atrophy of the callosal striations with some residual fiber structure from the corona radiata. Additionally, the edematous tissue shows increased diffusivity and a lateral fiber direction which is not apparent on the unaffected side. This fiber structure may be due to selective enhancement caused by the edema, or possibly a mass effect in which the tumor has displaced the callosal striations into a more purely lateral course. A similar lateral fiber enhancement is seen in Fig. 8-14.

Fig. 8-15 shows an axial DSI from a patient with a chronic thalamic infarct. The healthy side of the thalamus shows clear bimodal diffusion. The largest peak corresponds to the thalamocortical striations and the weaker peak is most likely due to intrathalamic connections or partial voluming with other striations. By contrast, the side with the infarct shows marked loss of the weaker diffusion peak. Loss of fiber structure in stroke is also seen in Fig. 8-16 which shows a DSI of a patient with a chronic stroke in the left occipital lobe. Whereas the optic radiation in the unaffected side is intact, the optic radiation in the side containing the stroke shows

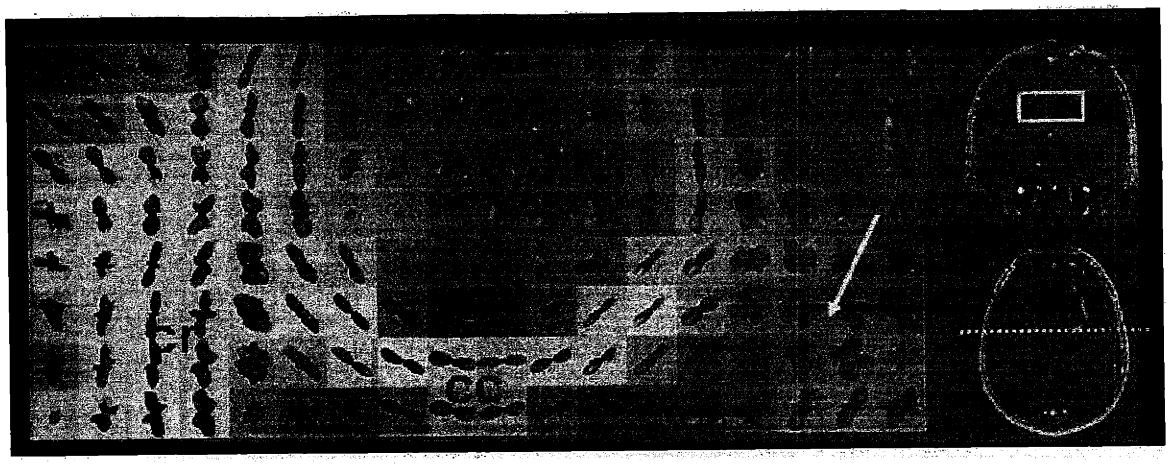

Figure 8-13: Subject E: Coronal DSI of patient with a resected oligodendroglioma. The image is posterior to the resection site. The side contralateral to the resection shows the intersection of the striations from the corpus callosum (cc, red) with the corona radiata (cr, blue). On the ipsilateral side, the callosal striations are absent although the cr fibers are partially intact. Enhanced lateral fiber structure (red, yellow arrow), most likely due to either selective edema enhancement or mass effect, is also observed.

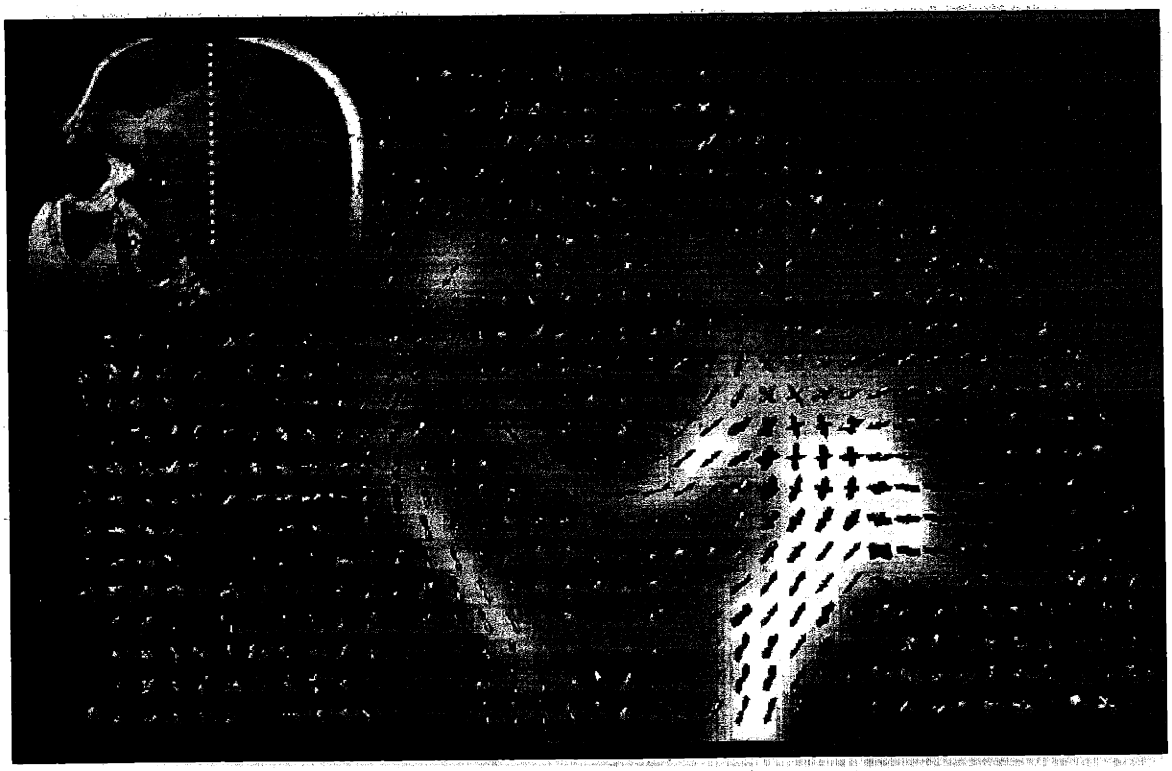

Figure 8-14: Subject F: Sagittal DSI of patient with temporal lobe tumor. The increased diffusion in the edema is seen to enhance the apparent fiber structure of the corona radiata and corpus callosum. There is also selectively oriented mediolateral diffusion seen within the edematous tissue.

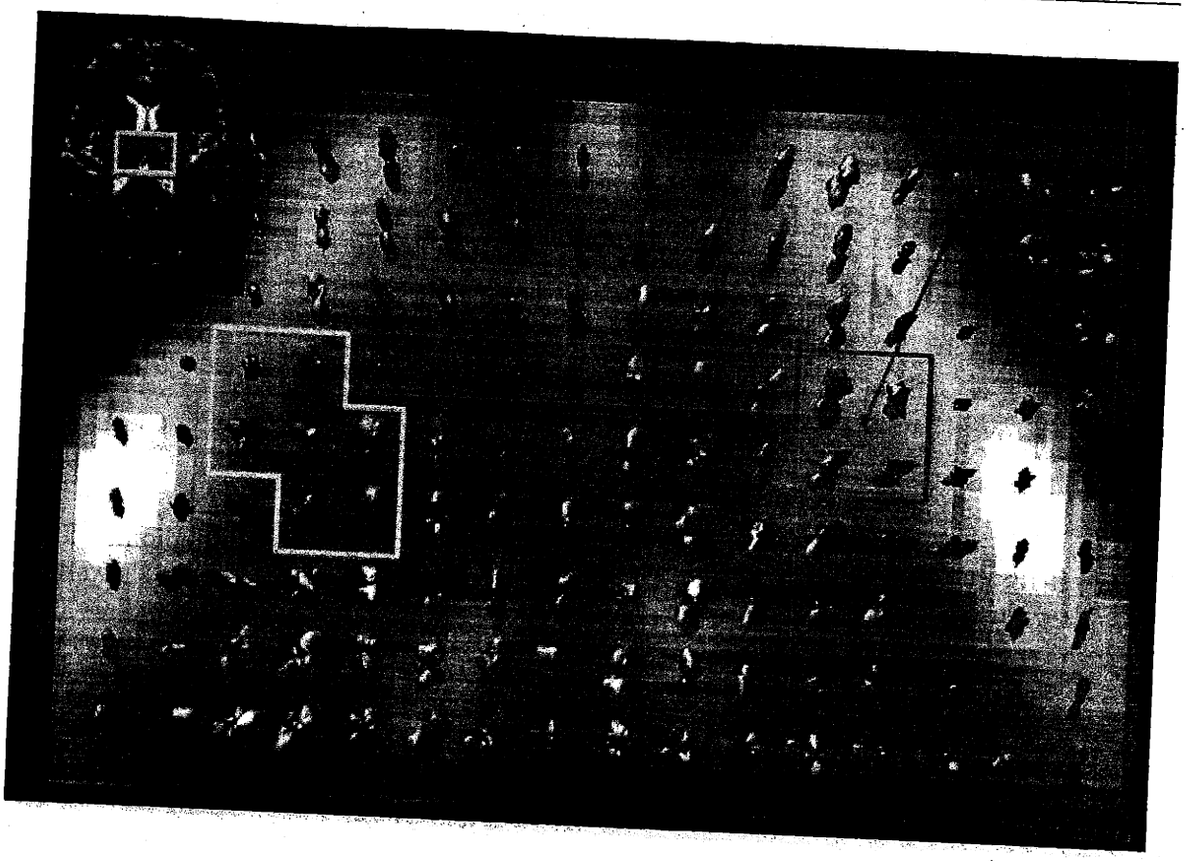

Figure 8-15: Subject G: Axial DSI of patient with a chronic thalamic infarct. Loss of complex fiber structure is seen in the area of infarction (red box) as compared to the normal contralateral side (white box).

massive Wallerian degeneration of the optic radiation and a lateral deflection of the fiber bundle.

8.6 Discussion

By measuring the microscopic three-dimensional diffusion function within each macroscopic voxel, DSI can resolve complex intravoxel tissue structure such as fiber crossing or fiber divergence within a single voxel. Histologically, such complex fiber structure can consist of interdigitating multicellular fascicles of tens to hundreds of microns in diameter. While DTI of such architectures would need to resolve individual fascicles, DSI overcomes this limitation by defining orientational coherence without individually resolving constituent fascicles.

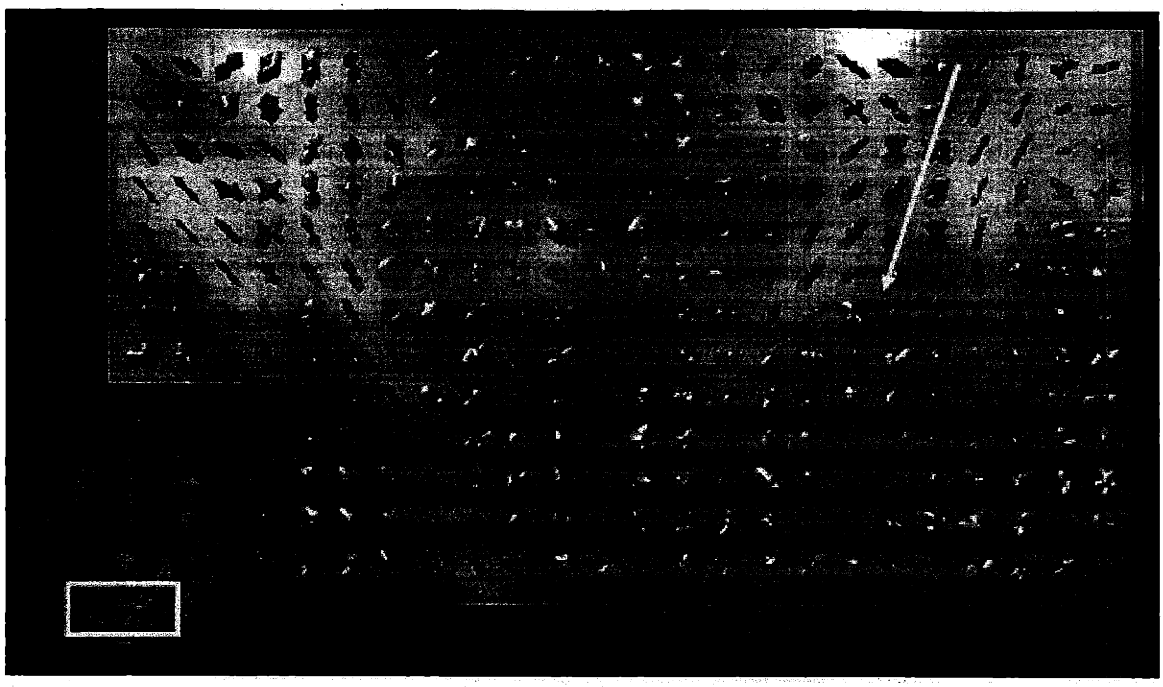

Figure 8-16: Subject H: Axial DSI of patient with chronic left occipital stroke (Subject H). Image shows Wallerian degeneration of the left optical radiation (yellow arrow).

Practical implementation of the DSI method required a number of experimental and conceptual modifications to the conventional spin displacement imaging experiment. Specifically, the diffusion function was reconstructed by taking the Fourier transform of the modulus of the diffusion signal as opposed to that of the full complex signal. We showed that the two transforms are equivalent for any ensemble-averaged diffusion process.

Moreover, in order to obtain sufficient spatial resolution of the diffusion function we employed effectively constant gradients as opposed to the pulsed gradients more conventionally employed by spin displacement imaging. The constant gradients yields an apparent center-of-mass diffusion function which artificially constricts, but does not reorient, the diffusion function. Lastly, in order to capture and visualize the salient orientational contrast the diffusion functions were analyzed and visualized in terms of the radial projection of the diffusion function on to the sphere. The resulting spin displacement ODF provides an object which should be possible to directly validate with tracer measurements.

In regions of intravoxel fiber crossing and divergence we observed multimodal diffusion functions consistent with the underlying heterogeneous fiber anatomy. In addition to observing multimodal diffusion in deep white matter intersections, we observed multimodal diffusion at the subcortical margin. The composite diffusion seen at the subcortical margin may be due to contributions from both white matter projections oriented normal to the cortical surface and intracortical connections oriented parallel to the cortical surface.

The conjecture that the observed surface-parallel component is due to intracortical connections is consistent with previous reports that gray matter appears anisotropic on DTI in kittens (20), but the anisotropy disappears later developmentally, putatively due to the formation of intracortical connections. Hence, it may be possible that subcortical anatomy appears relatively isotropic on diffusion tensor imaging, not due to the lack of any inherent diffusion restriction, but because of the orientational partial voluming. Results presented here suggest that DSI may be able to resolve such structure.

Clinical applications of DSI in stroke, surgical ablation, and cancer demonstrated the ability of DSI to resolve selective fiber loss. Hence, DSI of neurodegeneration may provide a tool for ascertaining the specific fiber populations affected in regions of neurodegeneration identified by conventional imaging contrast. Moreover, these results may help explain the changes in diffusion anisotropy observed in DTI in terms of the loss of selectively oriented fiber populations as opposed to changes in the diffusion properties. Interestingly, in the tumor cases we also observed increased angular contrast in regions of edematous tissue, most likely due to the enhanced diffusion from the increased water content. The increase in angular contrast with increased diffusivity suggests that it may be possible to increase the angular contrast in normal tissue by increasing the experimental diffusion time.

Recently, investigators have proposed computational reconstruction of white matter pathways from diffusion images as a method for mapping white matter connectivity (21–25), a project referred to as white matter tractography. However, tractography solutions based on the tensor paradigm tend to be confounded by intravoxel fiber

crossing and divergence (21, 26, 27). The ability to efficiently resolve such composite structure with DSI should render the the tractography problem significantly more tractable. Particularly, the spin displacement ODF provided by the DSI method may be used to provide a continuous fiber ODF as opposed to the single fiber orientation estimate provided by the diffusion tensor model. The continuous fiber ODF should facilitate statistical solutions of the tractography problem, a much needed construction if tractography solutions are ever to be used for hypothesis testing of white matter connectivity.

In conclusion, DSI affords the capacity to resolve distinct components of fiber architecture in white matter without recourse to a model of the underlying diffusion process. For example, whereas DTI measures the diffusion tensor within each voxel under he model assumption of Gaussian diffusion, DSI posits no such model. The model-independence and orientational resolution of the DSI method should extend the feasibility of noninvasive cerebral tractography and provide a general-purpose tool for noninvasive analysis of tissue architecture on the microscopic scale.

8.7 References

[1] P.T. Callaghan. *Principles of nuclear magnetic resonance microscopy.* Oxford, Great Britain, 1993.

[2] E.L. Hahn. Spin echoes. *Phys. Rev.*, 80:580–594, 1950.

[3] E.O. Stejskal and J.E. Tanner. Spin diffusion measurements: spin echoes in the presence of a time-dependent field gradient. *J. Chem. Phys.*, 42:288–292, 1965.

[4] J. Kärger and W. Heink. The propagator representation of molecular transport in microporous crystallites. *J. Magn. Reson.*, 51:1–7, 1983.

[5] M.D. Hürlimann and L.M. Schwartz amd P.N. Sen. Probability of return to origin at short times: a probe of microstructure in porous media. *Phys. Rev. B*, 51:14936–14940, 1995.

[6] P.P. Mitra, L.L. Latour, R.L. Kleinberg, and C.H. Sotak. Pulsed-field gradient NMR measurements of restricted diffusion and the return-to-origin probability. *J. Magn. Reson. A*, 114:47–58, 1995.

[7] M.E. Bastin. Correction of eddy current-induced artefacts in diffusion tensor imaging using iterative cross-correlation. *Magn. Reson. Imag.*, 17:1011–1024, 1999.

[8] P. Jezzard, A.S. Barnett, and C. Pierpaoli. Characterization of and correction for eddy current artifacts in echo planar diffusion imaging. *Magn. Reson. Med.*, 39:801–812, 1998.

[9] M.A. Horsfield. Mapping eddy current induced fields for the correction of diffusion-weighted echo planar images. *Magn. Res. Imag.*, 17:1335–1345, 1999.

[10] M. Koch and D.G. Norris. An assessment of eddy current sensitivity and correction in seingle-shot diffusion weighted imaging. *Phys. Med. Biol.*, 45:3821–3832, 2000.

[11] T.G. Reese, R.M. Weisskoff, and V.J. Wedeen. Diffusion NMR facilitated by a refocused Eddy-current EPI pulse sequence. In *Proc. Int. Soc. Magn. Reson. Med.*, volume 6, page 663, Sydney, Australia, 1998.

[12] P.P. Mitra and I. Halperin. Effects of finite gradient-pulse widths in pulsed-field-gradient diffusion measurements. *J. Magn. Reson. A*, 113:94–101, 1995.

[13] L.Z. Wang, A. Caprihan, and E. Fukushima. The narrow-pulse criterion for pulsed-gradient spin echo diffusion measurements. *J. Magn. Reson. A*, 117:209–219, 1995.

[14] B.P. Poncelet, V.J. Wedeen, R.M. Weisskoff, and M.S. Cohen. Brain parenchyma motion: measurement with cine echo-planar MR imaging. *Radiology*, 185:645–651, 1992.

[15] P.P. Mitra, P.N. Sen, L.M. Schwartz, and P.L. Doussal. Diffusion propagator as probe of the structure of porous media. *Phys. Rev. Lett.*, 68:3555–3558, 1992.

[16] R.F. Bass and K. Burdzy. Eigenvalue expansions for Brownian motion with an application to occupation times. *Electr. J. Prob.*, 1:1–19, 1996.

[17] N.I. Fisher, T. Lewis, and B.J.J. Embleton. *Statistical analysis of spherical data.* Cambridge, Great Britain, 1987.

[18] K.V. Mardia and P.E. Jupp. *Directional Statistics.* John Wiley & Sons, Ontario, 2000.

[19] P.J. Basser, J. Mattiello, and D. Le Bihan. Estimation of the effective self-diffusion tensor from the NMR spin echo. *J. Magn. Reson. B*, 103:247–254, 1994.

[20] C. Baratti, A.S. Barnett, and C. Pierpaoli. Comparative MR imaging study of brain maturation in kittens with t1, 2, and the trace of the diffusion tensor. *Radiology*, 210:133–142, 1999.

[21] P.J. Basser, D. Pajevic, C. Pierpaoli, J. Duda, and A. Aldroubi. In vivo fiber tractography using DT-MRI data. *Magn. Reson. Med.*, 44:625–632, 2000.

[22] S. Mori, B.J. Crain, V.P. Chacko, and P.C. van Zijl. Three-dimensional tracking of axonal projections in the brain by magnetic resonance imaging. *Ann. Neurol.*, 45:265–269, 1999.

[23] R. Xue, P.C. van Zijl, B.J. Crain, M. Solaiyappan, and S. Mori. In vivo three-dimensional reconstruction of rat brain axonal projections by diffusion tensor imaging. *Magn. Reson. Med.*, 42:1123–1127, 1999.

[24] V.J. Wedeen, T.L. Davis, R.M. Weisskoff, R. Tootell, B.R. Rosen, and J.W. Belliveau. White matter connectivity explored by MRI. In *Proc. Int. Conf. Functional Mapping of the Human Brain*, volume 1, page 69, Paris, France, 1995.

[25] T.E. Conturo, N.F. Lori, T.S. Cull, E. Akbudak, A.Z. Snyder, J.S. Shimony, R.C. McKinstry, H. Burton, and M.E. Raichle. Tracking neuronal fiber pathways in the living human brain. *Proc. Natl. Acad. Sci. USA*, 96:10422–10427, 1999.

[26] C. Poupon, C.A. Clark, V. Frouin, J. Regis, I. Bloch, D. Le Bihan, and J. Mangin. Regularization of diffusion-based direction maps for the tracking of brain white matter fascicles. *Neuroimage*, 12:184–195, 2000.

[27] C. Pierpaoli, A. Barnett, S. Pajevic, R. Chen, L. Penix, A. Virta, and P. Basser. Water diffusion changes in Wallerian degeneration and their dependence on white matter architecture. *Neuroimage*, 13:1174–1185, 2001.

Chapter 9

Connectivity Mapping

"At its best, it does celebrate a flow..."

Thomas Pynchon, *Gravity's Rainbow*

9.1 Preface

In the previous chapter we experimentally demonstrated the ability of diffusion spectrum imaging (DSI) to resolve complex intravoxel tissue structure including fiber crossing and fiber divergence within a single voxel. By taking the radial projection of the diffusion function within each voxel we arrived at a spin displacement orientation density function map. Here, we show how such maps can be used to map the anatomical connectivity of the brain. In particular, we introduce three algorithms which enable us to, respectively, (i) trace white matter pathways through complex anatomic regions, (ii) segment white matter bundles, and (iii) generate a structural connectivity matrix. The connectivity matrix formalism provides a robust framework for describing the degree of anatomical connectivity between any two points in the brain, a long-sought goal of magnetic resonance imaging.

9.2 Introduction

Two principles which govern the organization of the human brain are compartmentalization and connectivity. The human brain, according to the connectionist view, is organized into distinct processing regions interconnected by a network of anatomical relays. The processing units are responsible for executing primary cognitive functions, and higher cognitive functions arise from the coordination between the processing units.

The processing units are located in cerebral cortex. The cerebral cortex is as a highly convoluted sheet of gray matter which resides on the cortical surface, and is composed predominately of the neuronal cell boides. The term 'gray matter' is used to describe the unmyelinated portion of the neurons due to its gray appearance to the naked eye. Neural signals are processed in cortical gray matter and subsequently transmitted to various regions of the brain by white matter, so-called due to the white appearance of the myelinated axons. The white matter pathways are generally categorized into association fibers which convey information between gray matter regions within the same hemisphere, commisural fibers which project to corresponding gray matter regions on the opposite hemisphere, and projectional fibers which carry signals between cortex and lower brain regions.

While functional magnetic resonance imaging, positron emission tomography, and electromagnetic source imaging have shed considerable light on the anatomic location of the specialized processing regions within gray matter, there is currently no non-invasive imaging method capable of resolving the white matter connections between these regions. Crick cited this methodological impasse which Crick cited as a factor in the 'backwardness of human neuroanatomy' (1). Compared to our understanding of neural circuitry in lower animals where invasive tracer methods are technically and ethically feasible (2–4), our knowledge of the connectivity of the human brain is relatively impoverished. The ability to non-invasively image the architecture of white matter pathways would greatly elucidate how neural signals in the human brain are coordinated and processed as part of a distributed network.

9.2.1 Tractography

Recently, investigators have proposed using magnetic resonance diffusion tensor imaging (DTI) to map the geometry of white matter pathways (5–9), and therefrom infer the white matter connectivity of the brain. The so-called white matter tractography approach employed by these investigations draws on the correspondence between the measured diffusion tensor and the underlying microstructure of the tissue. Specifically, DTI measures the apparent water self-diffusion tensor within each voxel under the assumption of voxel-wise homogeneous Gaussian diffusion (10). The eigenstructure of the observed diffusion tensor then reflects the microstructure of the underlying tissue so that, for example, the major eigenvector of the diffusion tensor in a voxel parallels the mean fiber orientation in that voxel.

Drawing on a hydrodynamic analogy, the white matter tractography program treats the diffusion tensor major eigenvector field as a flow field and takes the streamlines of the flow field as the white matter pathways. More formally, the local tangent vector to the white matter path is identified with the local diffusion tensor major eigenvector

$$\dot{\mathbf{x}}(s) = \mathbf{e}_1(\mathbf{x}(s)) \tag{9.1}$$

where $\mathbf{x}(s)$ is the location of the path at a curvilinear coordinate s along the path, and $\mathbf{e}_1$ is the major eigenvector of the diffusion tensor $\mathbf{D}$ at location $\mathbf{x}$. For a given starting point $\mathbf{x}(0)$, also referred to as a 'seed', a white matter streamline is specified by the differential equation

$$\mathbf{x}(t) = \mathbf{x}(0) + \int_0^t \mathbf{e}_1(\mathbf{x}(s))\ ds. \tag{9.2}$$

The tractography integral is typically performed using a discrete summation with step sizes considerably smaller than the voxel size so some form of continuous interpolation, e.g., cubic or spline interpolation, is required.

While the diffusion tensor streamline approach has been used to trace major white matter fascicles, the method suffers from a number of significant disadvantages. Most

notably, the diffusion tensor model, with the attending assumption of voxel-wise homogeneous Gaussian diffusion, is incapable of resolving multiple fiber orientations per voxel. Consequently, streamline solutions are deeply confounded by intravoxel fiber crossing (8, 11, 12) which is ubiquitous at typical voxel resolutions (13, 14). Moreover, the streamline approach lacks a statistical model, is highly sensitive to noise and initial conditions, cannot be tabulated on the cortical surface, and provides no quantification of the strengths of the connections. With regards to the latter point, the existence of a streamline solution between two points does not guarantee the existence of a connection nor do the solutions indicate the strength or probability of the connection relative to other possible connections. With the above concerns in mind we sought to formulate a tractography paradigm which could (i) handle intravoxel fiber heterogeneity in a robust fashion, (ii) afford a statistical interpretation of the tract solutions, and (iii) provide a data structure which could be tabulated on the cortical surface.

9.2.2 Diffusion Spectrum Imaging

We have recently described a diffusion imaging method termed diffusion spectrum imaging (DSI) which is capable of resolving complex intravoxel tissue structure including fiber crossing and fiber divergence within a single voxel (15). Whereas DTI measures the diffusion function under the model assumption of Gaussian diffusion, DSI measures the voxel-average diffusion function without recourse to an analytical model of the diffusion process. Specifically, the DSI method measures the voxel-average spin displacement probability density function (PDF) within each voxel. The PDF $P(\mathbf{R}, \tau)$ expresses the average probability over the voxel of a spin being displaced by $\mathbf{R}$ in the experimental diffusion time τ. In regions of fiber crossing, the PDF exhibits clear multi-modal behavior corresponding to the underlying fiber orientation distribution. In contrast, DTI provides only the mean fiber orientation which is heavily confounded in such heterogeneous regions.

The basis of the DSI method lies in the Fourier reciprocal relationship between

the PDF and the diffusion signal as a function of gradient strength (16). Specifically,

$$P(\mathbf{R},\tau) = \mathcal{F}^{-1}[E(\mathbf{q},\tau)] \tag{9.3}$$

where $E(\mathbf{q},\tau)$ is the spin echo magnitude, and $\mathbf{q} = \gamma\delta\mathbf{g}$ is the spin displacement wave vector with γ the gyromagnetic ratio, δ the diffusion gradient duration, and $\mathbf{g}$ the diffusion gradient vector. The Fourier relationship between the PDF and the diffusion signal, which was first noted by Stejskal (17), allows for direct reconstruction of the PDF from a set of measurements of $E(\mathbf{q})$ obtained with various $\mathbf{q}$.

We have recently extended the Stejskal relation by showing that if the displacement function arises purely from diffusion then the diffusion signal is identical to is modulus, i.e., $E(\mathbf{q},\tau) = |E(\mathbf{q},\tau)|$. Hence, no information is lost by taking the modulus, as opposed to the full complex, Fourier transform of the diffusion signal, $P(\mathbf{r}) = \mathcal{F}^{-1}[E(\mathbf{q})] = \mathcal{F}^{-1}[|E(\mathbf{q})|]$. The identity between the diffusion signal and its modulus for a pure diffusion process stems from the fact that the Fourier transform of the ensemble average of a diffusion function is real and positive. For example, considering the short time and long time limits, at short times the diffusion function is Gaussian and the Fourier transform of a Gaussian is another Gaussian which is real and positive. At long times, if the diffusion is fully bounded, then the diffusion function is simply the auto-correlation of the diffusion geometry which again is real and positive (18,19). The proof of the positivity and reality of the diffusion signal in general was given in the previous chapter.

We have aditionally shown that the Fourier relation can be extended from pulsed gradients to effectively constant gradients. The constant gradient experiment produces a center-of-mass PDF which we describe in the following. For sake of comparison, under narrow pulse conditions the pulsed gradient spin echo (PGSE) experiment measures the probability of a spin displacing $\mathbf{R}$ in time Δ. The constant gradient experiment, on the other hand, measures the probability of a spin displacing from its *mean* position over time 0 to TE/2 to its *mean* position over time TE/2 to TE (20) (Fig. 8-2). The net effect of the constant gradient experiment is to artificially

constrict the diffusion function away from restriction barriers. The center-of-mass effect will not, however, reorient the diffusion function. With this simple conceptual modification, it is possible to use effectively constant gradients and take advantage of the dramatic boost in spatial resolution of the diffusion function.

Measuring the PDF for each voxel gives a function $P(\mathbf{x}, \mathbf{R})$ of six dimensions, namely the three dimensions of the voxel location $\mathbf{x}$ and the three dimensions of the displacement location $\mathbf{R}$. We have dropped the time argument for convenience. In order to visualize the PDF field in a lower dimensional space and to provide a function more akin to a fiber orientation distribution field we project the PDF field on to a five dimensional space by integrating over the radial coordinate of the PDF. The projected PDF, referred to as a spin displacement orientation distribution function (ODF), expresses the volume fraction of spins displacing into a differential solid angle about a unit normal vector $\mathbf{u}$. In the complex materials literature $\mathbf{u}$ is sometimes referred to as the microscopic director, or simply the director. Given the PDF $P(\mathbf{x}, \mathbf{R})$, the ODF is obtained via the projection

$$\psi(\mathbf{x}, \mathbf{u}) = \int_0^\infty P(\mathbf{x}, \rho\mathbf{u})\, d\rho \tag{9.4}$$

where $\mathbf{u}$ is a unit normal vector which indicates the spin displacement direction, and ρ is the radial coordinate in the diffusion space coordinate system. In practice the integral cannot be taken out to infinity and is rather taken to the linear field-of-view $\rho_{\max}$ of the PDF.

Despite the ability to resolve intravoxel heterogeneity, ODF streamline solutions will still suffer from all of the disadvantages of the diffusion tensor streamline approach cited above, most notably the lack of a statistical picture. Here, we describe a method for deriving a structural connectivity matrix from a diffusion spectrum image. The structural connectivity matrix framework offers a number of conceptual and practical advantages over the streamline approach including a statistical interpretation, the ability to express the connectivity results on the cortical surface, a register for inter-subject and inter-group comparisons, and a data structure suitable for network models

of functional brain activity. What is more, the cortical-surface representation afforded by the connectivity matrix method will facilitate validation against invasive tracer methods for which the results are typically expressed in terms of tracer density on the cortical surface. In comparison, validation of the actual tract solutions would require a histological method capable of delineating tracts over anatomical scales.

9.2.3 Generalized Streamline Tractography

The ODF measured by DSI is capable of resolving multiple fiber populations within a single voxel. Hence, streamline solutions based on the ODF field, as opposed to the diffusion tensor field, are capable of navigating regions of white matter fiber crossing. As the ODF represents a distribution of fiber orientations within each voxel, it is necessary to generalize the major eigenvector streamline method, which could only handle a single fiber orientation per voxel, to handle the full fiber orientation distribution. The purpose of the generalized streamline method presented in the following is to provide a basis for comparison with the major eigenvector streamline solutions, and to provide an explanatory tool for initial analysis of the data.

Following the major eigenvector streamline solution we define a generalized streamline integral which traces the *local* orientational maximum of the ODF

$$\mathbf{x}(t) = \mathbf{x}(0) + \int_0^t \text{argmax}_{|\dot{\mathbf{x}}(s)|} \psi(\mathbf{x}(s), |\dot{\mathbf{x}}(s)|) \beta(|\ddot{\mathbf{x}}(s)|)\, ds \tag{9.5}$$

where we have identified $\mathbf{u}$ with $\dot{\mathbf{x}}$, and β is a stiffness function, also referred to as a curvature penalty function, which defines a local window around the fiber tangent vector. If we think of ψ as giving the probability of a fiber orientation and β as the prior probability, then the function $\varphi = \psi\beta$ can be viewed as the posterior fiber orientation probability.

The stiffness function encourages paths to follow the local maxima of the ODF as opposed to the global maxima which may appear more favorable but would introduce unanatomical kinks into the paths. For example, given a choice between one direction with a particular probability and a small angular deflection, and another path with

a slightly larger probability but a much larger deflection, we would like to encourage the path to take the former. The need for the stiffness function can be motivated by the anatomical argument that white matter pathways tend to travel in relatively straight paths and do not typically bend rapidly. The 'stiffness' function is not due to the elastic stiffness of the fiber which is relatively negligible. Rather, the stiffness function should be viewed as curvature penalty. The curvature penalty represents a local enforcement of the global tendency for fibers to travel along shortest paths by anatomic design, not by mechanical constraint. We will return to this point later when we discuss the need for robust curvature penalty functions.

The polymer path integral literature often makes the following slender body, or Hookian, approximation for the stiffness function

$$\beta(|\dddot{\mathbf{x}}(s)|) = \exp\left(-\kappa|\ddot{\mathbf{x}}(s)|^2\right) \qquad (9.6)$$

where κ is the elastic stiffness modulus for the fiber (21). The Hookian stiffness function has the disadvantage however of unnecessarily penalizing small angular deflections. It would be desirable to define the stiffness function in such a way so as to heavily penalize fiber orientations far from, but not discourage fiber tangent vectors close to, the instantaneous fiber tangent vector. A probability function which accomplishes this trade-off is the ϵ-insensitive density function introduced by Vapnik(22)

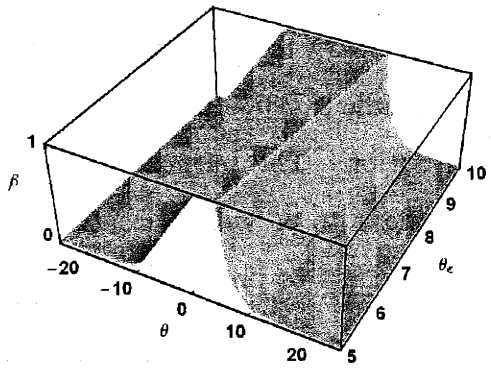

Figure 9-1: Curvature penalty function β (Eqn. 9.7) as a function of the angle θ from the fiber tangent vector and the width θ_ϵ of the angular tolerance window.

$$\beta(|\ddot{\mathbf{x}}(s)|) = \exp\left\{-\kappa[\max(|\ddot{\mathbf{x}}(s)| - \epsilon, 0)]\right\} \qquad (9.7)$$

where ϵ defines the diameter of the window in which the fiber curvature receives no penalty, and κ determines the curvature penalty outside of the tolerance window (Fig. 9-1). The optimal choice of the stiffness function and the stiffness parame-

ters remains an open problem which may benefit from validation studies or a cross-validation approach which is the traditional statistical method for determining the optimal trade-off between data agreement and smoothness. The curvature problem can also be ameliorated by reformulating the tractography problem as a problem not of path detection but of volume detection. In the volume segmentation picture, discrete anatomical structures are separated in position-orientation space, providing a more natural framework for dealing with the problem of intravoxel curvature. The volume segmentation paradigm is discussed in the following section.

9.2.4 Volume Segmentation

The generalized streamline integral given by Eqn. 9.5 allows for construction of white matter pathways from the ODF maps. However, a given set of streamline solutions may not capture the entire anatomical structure of interest. The limited coverage of the streamlines may be due to a number of possible factors including, but not limited to, incomplete seeding of the inputs to the structure of interest, the finite step-size of the tract integration, and the lack of a clear connection from the seed to the region of interest.

The above concerns can be addressed through volumetric segmentation of the diffusion data. The volumetric segmentation paradigm seeks to find volumes, as opposed to paths, which are connected in position-orientation space. The volumetric paradigm appeals to the notion that a white matter bundle is not a collection of paths but rather a volumetric object. The volume segmentation has the additional advantage of providing a data structure which we can describe in terms of morphometrics, e.g., volume, surface curvature, Euler number, etc.

The volume segmentation algorithm employed here uses a volume-growing algorithm to find voxels which are connected in position-orientation space. The cluster is initially taken from the voxel positions and orientations specified by a set of tractography solutions. Given a set of such seeds, the volume-growing algorithm iteratively expands the cluster volume to include connected voxels in position-orientation space until the number of voxels to be added to the cluster is smaller than n. Two voxels

are considered connected if they are spatially contiguous and have directional peaks within α degrees of each other. In sum, the clustering algorithm ultimately provides an anatomical volume which includes the tractography solutions and the neighboring voxels which are similar to those in the tract solutions.

9.2.5 Connectivity Matrix

9.2.5.1 Model

The tractography and volume segmentation methods described above facilitate visualization of the underlying connectivity structure of the data. While the visualization value is not to be diminished, it would be helpful to have a framework for testing specific hypotheses regarding connectivity. For example, the approaches outlined above would allow us to test whether two points in one subject are more strongly connected than two other points; or whether two points in cortex are more strongly connected in one population of subjects relative to another population. Here, we describe a method for constructing structural connectivity formalism which enables tests of this kind.

The objective of the connectivity matrix method is to ascertain the connectivity between any two specified points in cortex. The problem can be formulated in a fully probabilistic framework by defining a fiber orientation distribution function (ODF) field $\varphi(\mathbf{x}, \mathbf{u})$ where $\mathbf{u}$ is a unit normal vector which indicates the fiber orientation. The fiber ODF field expresses the probability of a fiber having orientation $\mathbf{u}$ at a position $\mathbf{x}$ in the image. The fiber ODF is commonly encountered in materials science for descriptions of, for example, polymer or metallic grain orientation distributions (23,24). What we refer to as the fiber ODF field is sometimes referred to as a texture field. It is also worthwhile to note that the major eigenvector streamline solution implicitly assumes $\varphi(\mathbf{x}, \mathbf{u}) = \delta(\mathbf{e}_1(\mathbf{x}) - \mathbf{u})$.

The physical connection between the fiber ODF φ and the spin displacement ODF ψ represents a pressing open problem. In the absence of an explicit forward model, obtained, for example, by numerical simulation or histological correlation, we must

content ourselves with a purely phenomenological ansatz. Here, we take the fiber ODF to be proportional to the spin ODF normalized to $[\langle\psi\rangle, \max\psi]$ where

$$\langle\psi\rangle = \int \psi \, d\mathbf{u} \tag{9.8}$$

is the average over the sphere. Specifically, we define

$$\varphi = Z^{-1}\left[\langle\psi\rangle + \frac{(\psi - \langle\psi\rangle)(\max\psi - \langle\psi\rangle)}{\max\psi - \langle\psi\rangle}\right] \tag{9.9}$$

where Z is a normalization factor to ensure that $\langle\psi\rangle = 1$.

Recall the curvature penalty function $\beta(|\ddot{\mathbf{x}}(s)|)$ which expresses the prior probability of a fiber orientation based on its curvature $|\ddot{\mathbf{x}}(s)|$. While we only consider here terms up to second derivatives in s it would be straightforward to include higher order curvature terms such as torsion. The curvature penalty function can be viewed as a prior fiber ODF, expressing the probability of a fiber orientation in the absence of the experiment data. With the fiber ODF ϕ and the curvature function β in hand we can develop a fully Bayesian formulation of the tractography problem.

Following from Bayes' theorem, the posterior probability $\phi(\mathbf{x}(s), |\dot{\mathbf{x}}(s)|, |\ddot{\mathbf{x}}(s)|)$ of a particular fiber orientation is the product of the empirical fiber ODF $\varphi(\mathbf{x}(s), |\dot{\mathbf{x}}(s)|)$ (the conditional probability) and the curvature ODF (the prior probability) $\beta(|\ddot{\mathbf{x}}(s)|)$, specifically, $\phi = \varphi\beta$. Given a path $\Xi = \mathbf{x}(s)$ obtained, say, from a tractography solution or by hand, we can then compute the normalized probability $\Phi(\Xi)$ of the path in terms of a continuum product over the fiber orientation posteriors

$$\Phi(\Xi) = Z^{-1} \lim_{\substack{\Delta s \to 0 \\ N \to \infty}} \left[\prod_{n=0}^{N} \phi(\mathbf{x}(n\Delta s), |\dot{\mathbf{x}}(n\Delta s)|, |\ddot{\mathbf{x}}(n\Delta s)|)\right]^{1/N} \tag{9.10}$$

where Z is a dimensionless normalization factor, n is the step number, and Δs is the step-size. The $1/N$ normalization exponent is required in order to avoid unnecessarily penalizing longer paths. The product integral (Eqn. 9.10) can be written as a standard

integral

$$\Phi(\Xi) = Z^{-1} \exp\left(L^{-1} \int_{\Xi} \log(\phi(\mathbf{x}(s), |\dot{\mathbf{x}}(s)|, |\ddot{\mathbf{x}}(s)|)) \, ds \right) \tag{9.11}$$

$$= Z^{-1} \exp\langle \log \phi \rangle_{\Xi} \tag{9.12}$$

where

$$L = \int |\dot{\mathbf{x}}(s)| \, ds \tag{9.13}$$

is the length of the path.

We have so far deferred the question of how to compute the partition function Z. The partition function must be computed over all feasible paths, and therefore, the calculation depends.on the particular probability we wish to evaluate. For example, if we wish to evaluate the probability of a given path between two specified points, say, $\mathbf{x}(0) = \mathbf{x}_a$ and $\mathbf{x}(L) = \mathbf{x}_b$, then the partition function can be computed from the path integral

$$Z = \int_{\mathbf{x}_a}^{\mathbf{x}_b} \Phi(\Xi) \, \mathcal{D}\mathbf{x} \tag{9.14}$$

where the path integral

$$\int_{\mathbf{x}_a}^{\mathbf{x}_b} \mathcal{D}\mathbf{x} \tag{9.15}$$

is the integral over all possible paths between $\mathbf{x}_a$ and $\mathbf{x}_b$, and $\mathcal{D}$ is Feynmann's path differential (21). In cases where only a single endpoint is fixed, the partition function can be calculated using Monte Carlo path integral methods.

From Eqn. 9.11 we can calculate (up to the partition function) the probability of any given path between two points. However, there is an infinite number of such paths and, what is more, there is no underlying probability density function from which to sample them. Even if there were such a distribution it would be exceedingly difficult to sample it efficiently. Given the above limitations we are forced to describe the path probability distribution by a limiting feature of the distribution. Here, we assign the connectivity coefficient to be *the probability of the most probable path* between the two points. Compared to, say, the mean or the median of the distribution, the maximum value metric has the advantage of being completely independent of the underlying

structure of the path distribution.

The most conspicuous disadvantage of identifying the maximal probability with the connectivity coefficient and ignoring the underlying structure of the distribution is favoring a thin strong path over a thick, slightly weaker path. That is, taking the most probable path as the objective ignores the neighborhood of the path, or, more generally, ignores the structure of the path probability distribution all together. However, the maximum value metric has the significant practical advantage of not requiring calculation of the entire probability distribution over Φ, but only its maximal value. For example, if we chose rather to represent the connectivity value by the mean or median path probability then we would need to know the underlying probability density function for the path space and a practical strategy for sampling the distribution.

For the sake of statistical testing we can generate a distribution of the maximal path probability under the experimental noise, and then take that as the distribution to be tested. For example, if we generate a distribution of the maximal probability between two specified points in two separate subjects, then we can test the hypothesis that the two distributions have the same mean under the experimental noise.

The identification of the probability of the most probable path with the connectivity coefficient can be written more formally as follows. If the two points are denoted $\mathbf{x}_i$ and $\mathbf{x}_j$ then the most probable path Ξ^* can be written

$$\Xi^*(\mathbf{x}_i, \mathbf{x}_j) = \arg \max_{\Xi(\mathbf{x}_i, \mathbf{x}_j)} \Phi(\Xi) \tag{9.16}$$

where $\Xi(\mathbf{x}_i, \mathbf{x}_j)$ is the set of all paths between $\mathbf{x}_i$ and $\mathbf{x}_j$. For a set of points $\{\mathbf{x}_k\}$ we take the connectivity matrix element C_{ij} to be the probability of the most probable path between $\mathbf{x}_i$ and $\mathbf{x}_j$; specifically,

$$C_{ij} = \Phi(\Xi^*(\mathbf{x}_i, \mathbf{x}_j)). \tag{9.17}$$

The optimization problem implied by Eqn. 9.16 can be solved in practice using the Metropolis-type algorithm (25) described in the following section.

9.2.5.2 Algorithm

The Metropolis algorithm is a simulated annealing algorithm which can, ideally, find the global extremum of an arbitrary energy function with arbitrary constraints (25). Here, we wish to find the most probable path which satisfies the boundary conditions $\mathbf{x}(0) = \mathbf{x}_i$ and $\mathbf{x}(L) = \mathbf{x}_j$. To do so, we represent the path as a smoothing cubic spline through a set of N control points $\{\mathbf{x}_n\}$. To enforce the boundary conditions we fix $\mathbf{x}_0 = \mathbf{x}_i$ and $\mathbf{x}_N = \mathbf{x}_j$.

Initially, the control points are evenly spaced along a circular arc between the end points. We then perturb the control points, calculate a new spline, respace the control points evenly along the spline (referred to here as rethreading), and then calculate the new path probability according to the discrete version of Eqn. 9.11. If the resulting path probability is greater than the best achieved so far then the control points are set to the perturbed control points with some probability. If the space between the control points exceeded some value then an additional control point was added and all the control points were rethreaded. Similarly, if the space between the control points falls below some specified value then a control point is removed and the remaining control points are rethreaded. The acceptance probability and the size of the perturbations are decreased (i.e., 'cooled' in the annealing parlance) exponentially with each iteration until the acceptance probability falls to some negligible value.

If the cooling schedule is sufficiently slow then the Metropolis algorithm described above will find the most probable path between the specified pair of points. Otherwise, the solution may freeze in a local minimum. In sum, the procedure for constructing the connectivity matrix is for every pair of points in the set to find the most probable path via the Metropolis algorithm and assign that probability to the connectivity coefficient between those two points.

9.3 Methods

9.3.1 Imaging

The tractography solutions were computed on the data acquired on Subject A from Chap. 8. We review the protocol here.

Diffusion spectrum images were acquired on a healthy volunteer on a 3T Siemens Allegra. Eight sagittal slices encompassing the entire left hemisphere were acquired. The voxel resolution was 4mm isotropic with no gap. The DSI data were acquired using a single-shot echo-planar MRI acquisition and the cgTRBE sequence describe in the previous chapter (Chap. 8). For each experiment, the π-pulse pair was positioned to minimize the eddy currents at readout. The imaging parameters were TE/Δ/δ = 140/65/60ms. The acquisitions were synchronized with late-diastole by peripheral pulse trigger to minimize effects of brain motion (26).

The diffusion gradient sampling points were obtained from a three-dimensional keyhole Cartesian grid. The keyhole grid consisted of the points in reciprocal space on a $9 \times 9 \times 9$ Cartesian grid ($\Delta q = 0.17\mu\text{m}^{-1}$) which lay a sphere of diameter 9, which gave 258 q-space sampling points. To achieve a desired q_{max} the grid was scaled linearly in g so that the outermost point had a magnitude of $g_{\text{max}} = 40\text{mT/m}$, corresponding to $q_{\text{max}} = 0.67\mu\text{m}^{-1}, b_{\text{max}} = 2.0 \times 10^4\text{s/mm}^2$.

For each voxel the diffusion signal values were placed on a $9 \times 9 \times 9$ grid according to the points from which the values were sampled. The corners of the grid where no values were obtained due to the keyhole truncation were set to zero. For each voxel the PDF was then reconstructed by taking the three-dimensional fast Fourier transform of the data grid for that voxel. The ODF for each voxel was calculated by integrating over the radial coordinate (using cubic interpolation) of the PDF. For visualization purposes the ODFs were scaled to $[0, 1]$ within each voxel and displayed as spherical polar plots. The ODF reconstruction scheme is outlined schematically in Fig. 8-4. For sake of comparison we also calculated the diffusion tensor for each voxel using a least-squares fit to the diffusion data (27).

9.3.2 Connectivity

9.3.2.1 Generalized Streamline Tractography

Streamline solutions were computed for the caudal pons, the corpus callosum, the middle cerebellar pontine fibers, the superior cerebellar peduncle, the corpus callosum, the cingulum, and the anterior/mediodorsal thalamic nucleus. The tracts were seeded by placing a single seed at the base of the the fiber population of interest, and then growing the seed population within a specified cardinal plane. The seed growing was accomplished with the volume segmentation algorithm described in Sec. 9.2.4 and below, but restricting the seeds to the specified cardinal plane.

The streamline solutions were generated using the discrete analog of the general streamline integral given by Eqn. 9.5 with stepsize $\Delta s = .2\text{mm}$, and the robust stiffness function (Eqn. 9.7) with an angular tolerance $\theta_c = 15°$ and falloff $\kappa = .4/\text{o}$. The ODF was evaluated at each step using spline interpolation in the original data. The most probable fiber orientation at each step was obtained by finding the vertex from the geodesation which had the maximum associated ODF value. Each tract solution was terminated when the tract reached empty space.

9.3.2.2 Volume Segmentation

For each fiber population, the points in position-orientation space containing tracts were then input as seeds to the volume segmentation algorithm. Two voxels were considered connected if they were face or edge neighbors (vertex neighbors were excluded) and they had ODF peaks within $\alpha = 15°$ of each other. The ODF peaks were found by identifying the vertices of the ODF geodesation which were local maxima on the sphere and had a magnitude greater than 0.3 times the maximum value. The volume growing was halted when the set of neighboring voxels had less than $n = 8$ voxels. Isosurface contours for the volumes were also computed by smoothing the segmentation volume with a Gaussian kernel ($\sigma = 1\text{mm}$), and then extracting the isocontour for a value of 0.8 times the maximum value.

point #	anatomical location
3	visual striate (Vs)
5	visual parastriate (VPara)
7	visual peristriate (Vperi)
11-12	somatosensory (S)
13	primary sensorimotor (SM1)
16-17	primary motor (M1)
19-20	premotor (Mpre)
21-24	superior frontal gyrus (SFG)

Table 9.1: Points selected for connectivity matrix calculation. The points ran posterior to anterior from approximately the inferior aspect of occipital cortex to the crown of the superior frontal gyrus.

9.3.2.3 Connectivity Matrix

Twenty-five ($n = 25$) evenly spaced points were selected on a single sagittal slice approximately 12mm to the left of the midline. The points ran posterior to anterior from the inferior aspect of occipital cortex to the crown of the superior frontal gyrus (Table 9.1). The optimal path was computed between all $n(n-1)/2 = 300$ unique pairs of points, excluding self-pairs.

For each point pair, the number of control points was selected so that the average space between control points was more than 4mm and less than 8 mm. The optimal path was then found by maximizing the discrete version of the probability integral given by Eqn. 9.11. If during the course of the annealing the average space fell below or above the limits specified above, then a control point was, respectively, subtracted or added. The perturbation size was initially 10mm which was then relaxed exponentially with iteration number. Similarly, the acceptance probability was relaxed exponentially with iteration number. After cooling, the probability of the most probable path between points $\mathbf{x}_i$ and $\mathbf{x}_j$ was then entered into the connectivity matrix element C_{ij}. The perturbations were cooled until the path probability did not decrease by more than 0.1% in 50 iterations. A typical run took approximately 500 iterations to converge.

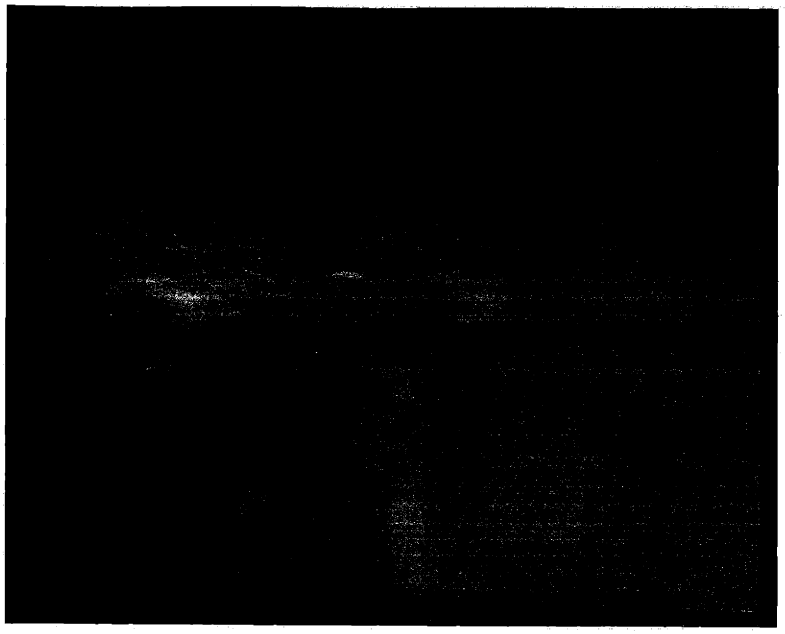

Figure 9-2: Tractography of the antero- and mediodorsal thalamic nuclei.

9.3.3 Results

9.3.3.1 Tractography and Volume Segmentation

The tractography solutions for the anterior/mediodorsal thalamic nucleus are shown in Fig. 9-2. The projections are seen to bifurcate anterior to the genu of the corpus callosum. The first population terminates with approximately uniform density over orbitofrontal cortex to the frontal gyri. The second population projects to the limbic cortex of the cingulate gyrus. The projection to the cingulate gyrus terminates with a superoinferior orientation. Both populations curve medially but are not significantly deflected by the corpus callosum.

The tractography results for the brainstem are shown in Fig. 9-3. The fibers seeded in the rostral pons are seen to bifurcate at the cerebellar pontine fibers, although a fraction of the fibers did not respect the bifurcation. This observed bifurcation is consistent with the known separation of the projections from the rostral pons into, anteriorly, the corticospinal tract and, posteriorly, the projections through the tegmentum. The fibers were not significantly deflected by the cerebellar pontine fibers projecting into the middle cerebellar peduncle. The superior cerebellar peduncle are

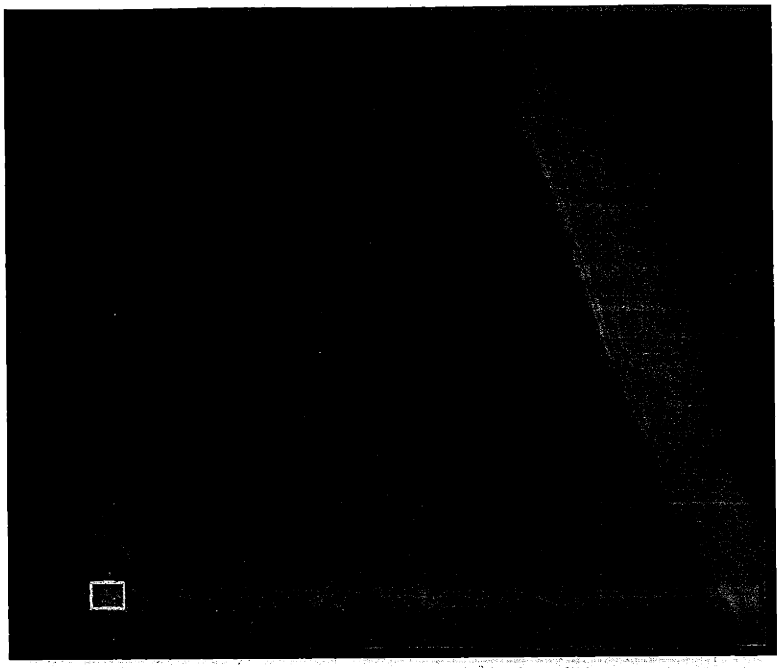

Figure 9-3: Tractography of the pontine decussation. The tractography results are taken from the ROI (yellow square) in the return-to-origin probability image at bottom left. The tracts are displayed as transparent rubes. The blue fibers are the projections from the caudal pons. The anterior blue fibers are the corticospinal tract and the posterior blue fibers include the medial lemniscus, the spinothalamic tract, and the projections from the reticular formation. The red fibers are the cerebellar pontine fibers projecting into the middle cerebellar peduncle, and the green fibers are the superior cerebellar peduncle. The line segments in the background show the peaks of the ODFs within each voxel. The color of the line segments reflect the orientation of the ODF peak with red indicating mediolateral, green anteroposterior, and blue superoinferior.

seen to intersect, and eventually join, the fibers from the tegmentum.

The cortical territory of the projections from the rostral pons can be seen in Fig. 9-4. The corticospinal tract fibers (anterior blue) are seen to curve posteriorly to project to the motor cortex. The tegmental tracts (posterior blue) project via the thalamus to both somatosensory and frontal cortex, although less densely to the latter. The superior cerebellar peduncle (green) projects through the ventral lateral thalamus and terminates in the motor and premotor cortices.

In addition to the projections from the rostral pons we also investigated the cingulum bundle and the striations of the corpus callosum. Fig. 9-5 shows the tractography results and Fig. 9-6 the volume segmentation results. From the tractography results

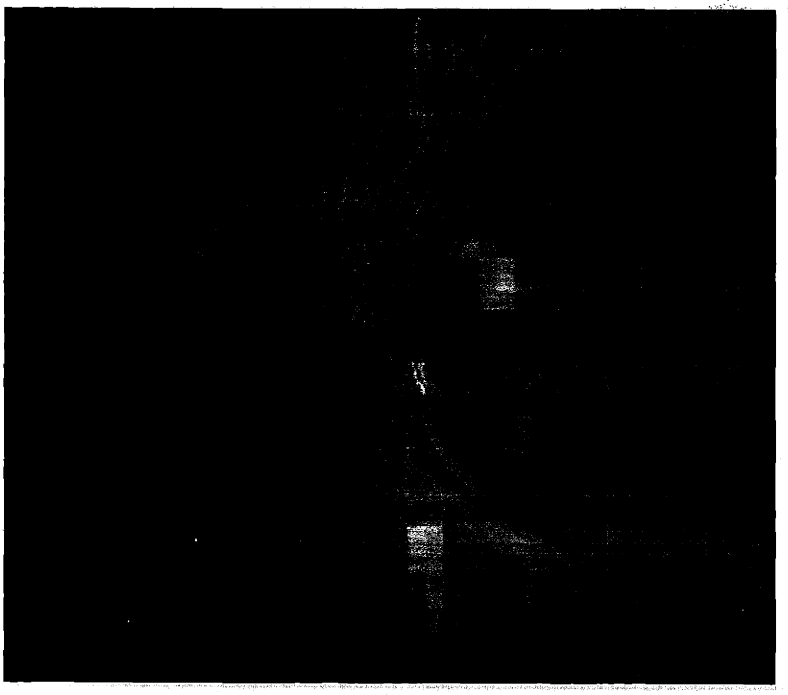

Figure 9-4: Projections from the rostral pons. The blue fibers are the projections from the rostral pons into the corona radiata via the thalamus. The red fibers are the cerebellar pontine fibers projecting into the middle cerebellar peduncle, and the green fibers are the superior cerebellar peduncle.

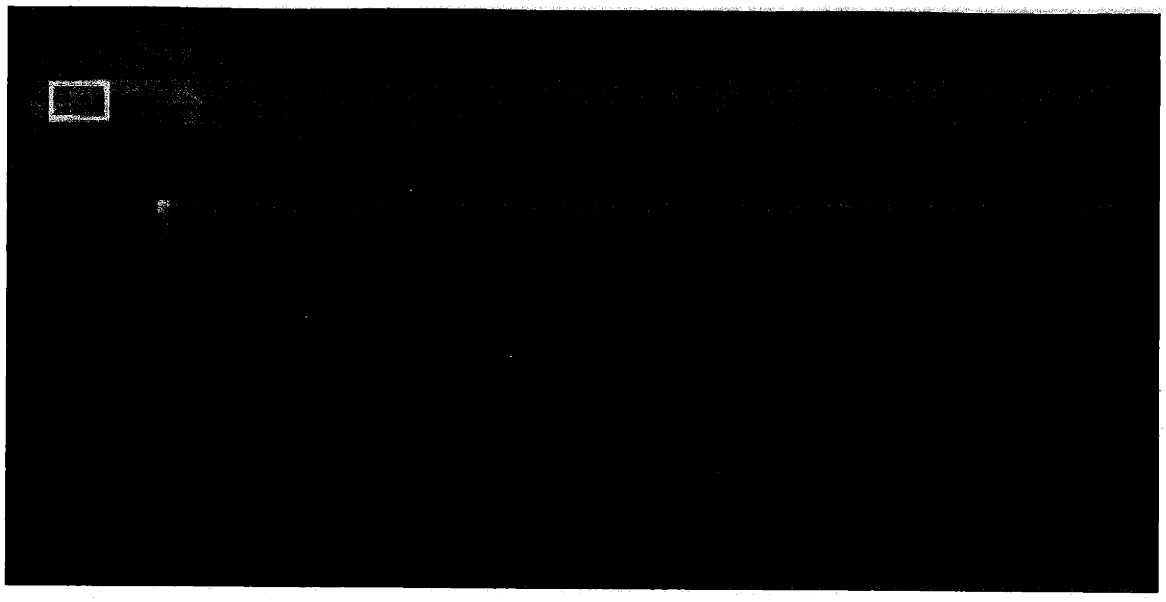

Figure 9-5: Tractography of the corona radiata, the cingulum, and the corpus callosum. The blue fibers are the projections from the rostral pons into the corona radiata via the thalamus. The red fibers are the corpus callosum, and the green fibers are the cingulum bundle and its projections to frontal cortex.

we can see the interdigitation of the corona radiata with the corpus callosum with no discernible deflection of one population by the other. The cingulum bundle is seen to reside superior to the corpus callosum with no intersection. The cingulum curves medially to project to frontal cortex.

9.3.3.2 Connectivity Matrix

Fig. 9-7 shows an example annealing process. The figure shows the annealing process for the optimal path between primary motor and primary sensorimotor cortex. The connectivity matrix for the set of all $n = 25$ points in the test set is shown in Fig. 9-8. Generally, we observe a pattern of strong self-connectivity within the visual system and within the superior frontal gyrus. Low connectivity is observed between visual cortex and all cortices anterior to and including the primary sensorimotor cortex. Points within a sulcus such as points 11 and 15 showed lower connectivity than points located at the crown of gyri.

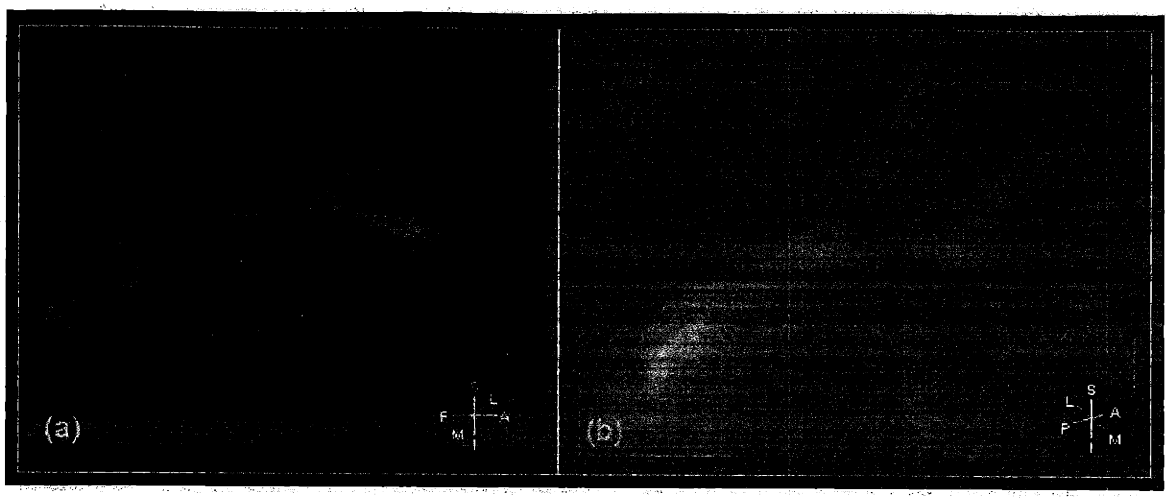

Figure 9-6: Volume segmentation of the corona radiata, the corpus callosum, the cingulum bundle, and the projections of the cingulum. The segmented volume is displayed as a transparent isosurface superimposed on the tractography solutions which were used as the seeds. The red volume is the corpus callosum, the green volume is the cingulum bundle and its projections, and the blue volume is the corona radiata. (a) Viewed medial to lateral (opposite face of Fig. 9-5). (b) Viewed medial-posterior to anterior-lateral.

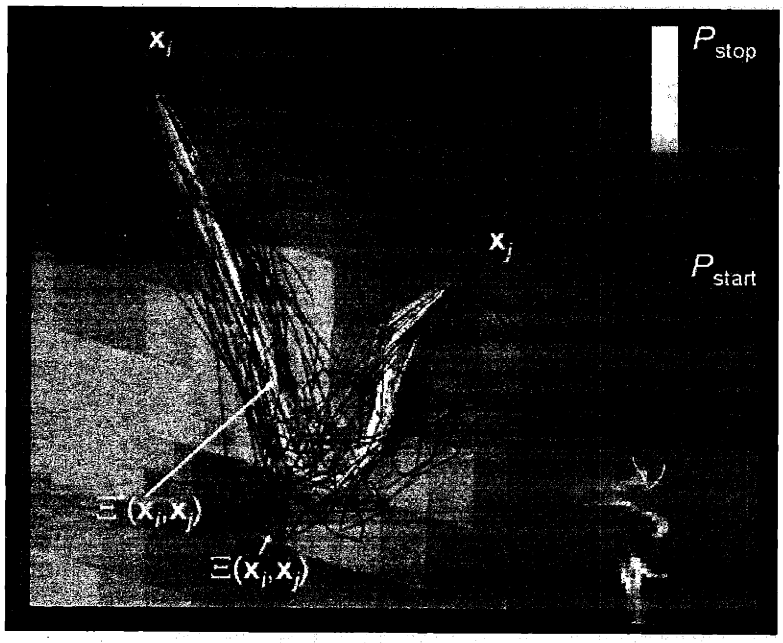

Figure 9-7: Example simulated annealing run for the path between primary motor and primary sensorimotor cortices. The fibers show every 10th sample path out of approximately 500 paths sampled. The color of the fiber indicates the probability of the path according to the color scale shown at top right. The fixed endpoints are indicated by the two small white circles. The image at bottom right shows a return-to-origin probability image with the optimal path in yellow.

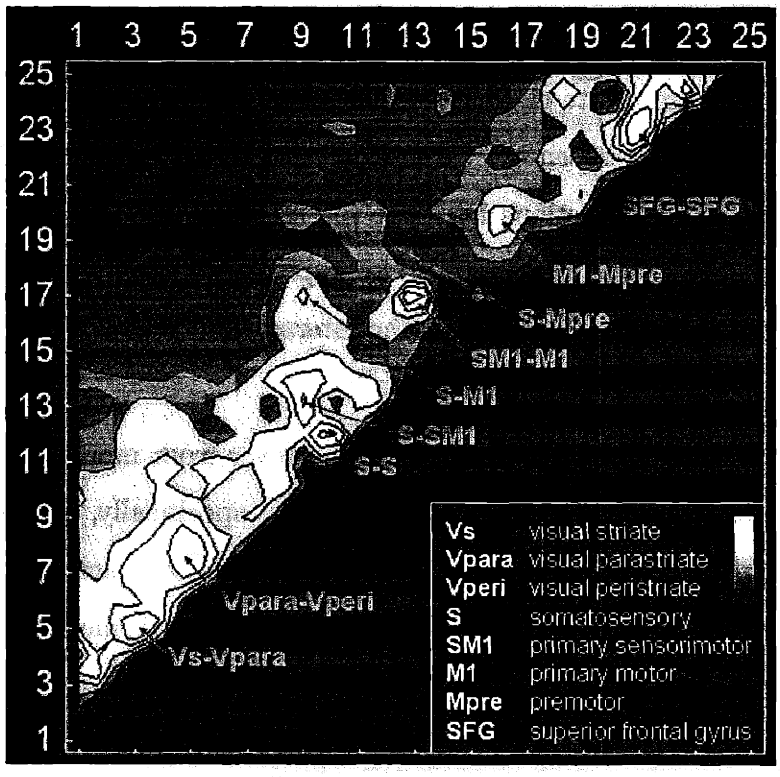

Figure 9-8: Connectivity matrix for all test points. The colorscale shows the relative probability of the connection according to the colorbar shown at bottom right with red indicating less probable and white more probable. The anatomical location of the points is given in the legend at bottom right and in Table 9.1.

9.3.4 Discussion

Three methods were presented for the inference of white matter connectivity from DSI: generalized streamline tractography, volume segmentation, and connectivity matrix mapping. The generalized streamline method represents a generalization of the major eigenvector streamline method commonly employed by diffusion tensor-based tractography (5–9). However, whereas major eigenvector streamline solutions are confounded by intravoxel fiber crossing (8, 11, 12), generalized streamline tractography based on DSI can navigate complex white matter intersections. For example, in Fig. 9-3 the intersection between the cerebellar pontine fibers from the middle cerebellar peduncle and the projections from the rostral pons was clearly resolved. The ability to resolve fiber intersection can also be appreciated from the volume segmentation results in Fig.s 9-6a and b showing the intersection of the corona radiata with the corpus callousm.

The generalized streamline solutions suffer however from many of the disadvantages of the major eigenvector streamline solutions, specifically, the lack of a statistical picture and the difficulty of registering tract solutions across subjects. The above limitations are resolved by the connectivity matrix framework presented in Sec.řefsec:ConnectivityMatrix.

In Sec. 9.3.3.2 we presented the connectivity matrix results for a set of cortical surface points encompassing both positive and negative controls. We observed significant self-connectivity within visual cortex and within motor cortex and relatively weaker connectivity between the two systems. As seen from this example, the connectivity matrix method allows for direct evaluation of both weak and strong connections whereas the tractography solutions tend to find only the strong solutions.

The connectivity matrix method contains two model-dependent terms which could benefit from further investigation, specifically, the form of the stiffness function and the mapping between the spin displacement and fiber ODFs. The model specification problem for the stiffness function bears a strong resemblance to the classical statistical trade-off between data-adherence and smoothness, in which case the smoothness

function specification problem may benefit from traditional model selection methods such as cross-validation. The relationship between the spin displacement and fiber ODFs represents a more profound problem.

The relationship between the observed diffusion function and the underlying tissue microstructure is the problem at the heart of diffusion imaging. While the problem may benefit from numerical simulations of diffusion in toy models of white matter, the number of physical unknowns will ultimately limit the accuracy of such models. It should be possible though to elucidate the diffusion-structure relationship through histological correlation.

The connectivity matrix method provides a number of additional advantages including a statistical interpretation of the tract solutions and the ability to express the connectivity results directly on the cortical surface as opposed to in the anatomical volume. The cortical surface representation should enable cortical-surface based averaging of connectivity results over a pool of subjects (28,29). In contrast, averaging the volumetric tract solutions would require volumetric morphing between subjects and a method to suitably normalize the tract density within the volume. The cortical-surface representation should also facilitate validation against invasive tracer methods for which the results are commonly expressed in terms of tracer density on the cortical surface. Lastly, the connectivity matrix formalism provides a data structure readily submittable to network models of functional brain activity (30,31).

This chapter is based on a paper in preparation and on published abstracts (32–34).

9.4 References

[1] F. Crick and E. Jones. Backwardness of human neuroanatomy. *Nature*, 361:109–110, 1993.

[2] L. Heimer and M.J. Robards, editors. *Neuroanatomical tract-tracing methods.* Plenum, New York, 1981.

[3] L. Heimer and L. Zaborszky, editors. *Neuroanatomical tract-tracing methods 2.* Plenum, New York, 1989.

[4] M-M. Mesulam, editor. *Tracing neural connections with horseradish peroxidase.* Wiley, Great Britain, 1982.

[5] T.E. Conturo, N.F. Lori, T.S. Cull, E. Akbudak, A.Z. Snyder, J.S. Shimony, R.C. McKinstry, H. Burton, and M.E. Raichle. Tracking neuronal fiber pathways in the living human brain. *Proc. Natl. Acad. Sci. USA*, 96:10422–10427, 1999.

[6] R. Xue, P.C. van Zijl, B.J. Crain, M. Solaiyappan, and S. Mori. In vivo three-dimensional reconstruction of rat brain axonal projections by diffusion tensor imaging. *Magn. Reson. Med.*, 42:1123–1127, 1999.

[7] S. Mori, B.J. Crain, V.P. Chacko, and P.C. van Zijl. Three-dimensional tracking of axonal projections in the brain by magnetic resonance imaging. *Ann. Neurol.*, 45:265–269, 1999.

[8] P.J. Basser, D. Pajevic, C. Pierpaoli, J. Duda, and A. Aldroubi. In vivo fiber tractography using DT-MRI data. *Magn. Reson. Med.*, 44:625–632, 2000.

[9] V.J. Wedeen, T.L. Davis, R.M. Weisskoff, R. Tootell, B.R. Rosen, and J.W. Belliveau. White matter connectivity explored by MRI. In *Proc. Int. Conf. Functional Mapping of the Human Brain*, volume 1, page 69, Paris, France, 1995.

[10] P.J. Basser, J. Mattiello, and D. Le Bihan. MR diffusion tensor spectroscopy and imaging. *Biophys. J.*, 66:259–267, 1994.

[11] C. Pierpaoli, A. Barnett, S. Pajevic, R. Chen, L. Penix, A. Virta, and P. Basser. Water diffusion changes in Wallerian degeneration and their dependence on white matter architecture. *Neuroimage*, 13:1174–1185, 2001.

[12] C. Poupon, C.A. Clark, V. Frouin, J. Regis, I. Bloch, D. Le Bihan, and J. Mangin. Regularization of diffusion-based direction maps for the tracking of brain white matter fascicles. *Neuroimage*, 12:184–195, 2000.

[13] A.L. Alexander, K.M. Hasan, M. Lazar, J.S. Tsuruda, and D.L. Parker. Analysis of partial volume effects in diffusion-tensor MRI. *Magn. Reson. Med.*, 45:770–780, 2001.

[14] M.R. Wiegell, H.B.W. Larsson, and V.J. Wedeen. Fiber crossing in human brain depicted with diffusion tensor MR imaging. *Radiology*, 217:897–903, 2000.

[15] V.J. Wedeen, T.G. Reese, D.S. Tuch, M.R. Weigel, J-G. Dou, R.M. Weisskoff, and D. Chessler. Mapping fiber orientation spectra in cerebral white matter with Fourier-transform diffusion MRI. In *Proc. Int. Soc. Magn. Reson. Med.*, volume 8, page 82, Denver, Colorado, 2000.

[16] E.O. Stejskal. Use of spin echoesd in a pulsed magnetic-field gradient to study anisotropic, restricted diffusion and flow. *J. Chem. Phys.*, 43:3597–3603, 1965.

[17] E.O. Stejskal and J.E. Tanner. Spin diffusion measurements: spin echoes in the presence of a time-dependent field gradient. *J. Chem. Phys.*, 42:288–292, 1965.

[18] D.G. Cory and A.N. Garroway. Measurement of translational displacement probabilities by NMR: an indicator of compartmentation. *Magn. Reson. Med.*, 14:435–444, 1990.

[19] P.T. Callaghan. *Principles of nuclear magnetic resonance microscopy.* Oxford, Great Britain, 1993.

[20] P.P. Mitra and I. Halperin. Effects of finite gradient-pulse widths in pulsed-field-gradient diffusion measurements. *J. Magn. Reson. A*, 113:94–101, 1995.

[21] H. Kleinert. *Path integrals in quantum mechanics, statistics, and polymer physics.* World Scientific, Singapore, 1995.

[22] V.N. Vapnik. *Statistical Learning Theory.* John Wiley & Sons, Ontario, 1998.

[23] M. Doi and S.F. Edwards. *The theory of polymer dynamics.* Claredon, Oxford, 1989.

[24] P.G. de Gennes and J. Prost. *The physics of liquid crystals.* Claredon, Oxford, 1993.

[25] P.J.M. van Laarhoven, editor. *Simulated annealing : theory and applications.* D. Reidel, Boston, 1987.

[26] B.P. Poncelet, V.J. Wedeen, R.M. Weisskoff, and M.S. Cohen. Brain parenchyma motion: measurement with cine echo-planar MR imaging. *Radiology*, 185:645–651, 1992.

[27] P.J. Basser, J. Mattiello, and D. Le Bihan. Estimation of the effective self-diffusion tensor from the NMR spin echo. *J. Magn. Reson. B*, 103:247–254, 1994.

[28] A.M. Dale, B. Fischl, and M.I. Sereno. Cortical surface-based analysis. I: Segmentation and surface reconstruction. *Neuroimage*, 9:179–194, 1999.

[29] B. Fischl, M.I. Sereno, and A.M. Dale. Cortical surface-based analysis. II: Inflation, flattening, and a surface-based coordinate system. *Neuroimage*, 9:195–207, 1999.

[30] B. Horwitz, M.A. Tagamets, and A.R. McIntosh. Neural modeling, functional brain imaging, and cognition. *Trends Cogn. Sci.*, 3:91–98, 1999.

[31] A.R. McIntosh. Understanding neural interactions in learning and memory using functional neuroimaging. *Ann. NY Acad. Sci.*, 30:556–571, 1998.

[32] D.S. Tuch, J.W. Belliveau, and V.J. Wedeen. Probabilistic tractography using high angular resolution diffusion imaging. In *Proc. Int. Conf. Functional Mapping of the Human Brain*, volume 6, Paris, France, 2000.

[33] D.S. Tuch, J.W. Belliveau, and V.J. Wedeen. A path integral approach to white matter tractography. In *Proc. Int. Soc. Magn. Reson. Med.*, volume 7, page 791, Philadelphia, Pennsylvania, 2000.

[34] D.S. Tuch, M.R. Wiegell, T.G. Reese, J.W. Belliveau, and V.J. Wedeen. Measuring cortico-cortical connectivity matrices with diffusion spectrum imaging. In *Proc. Int. Soc. Magn. Reson. Med.*, volume 9, page 502, Glasgow, Scotland, 2001.

Chapter 10

Q-Ball Imaging

"And this is the moral - Stick to your sphere..."

John Towsend Trowbridge, *Darius Green and His Flying Machine*

10.1 Introduction

In Chap. 8 we described the diffusion spectrum imaging (DSI) method which provides a practical method for measuring the spin diffusion function *in vivo*. The DSI method exploited the Fourier reciprocal relationship between the diffusion signal and the diffusion function to directly reconstruct the spin diffusion function within each voxel. Specifically, the diffusion function within each voxel was reconstructed by sampling the diffusion signal on a Cartesian grid and then taking the Fourier transform on the grid. In order to visualize and analyze the diffusion function we projected the diffusion function on to the sphere, and the resulting function was termed a spin displacement orientation distribution function (ODF).

The radial projection used to construct the ODF discards all of the radial information contained in the diffusion function. Hence, the ODF does not contain the radial information which was originally present in the Cartesian diffusion function, but preserves the salient angular contrast. It would therefore dramatically boost the acquisition efficiency if we could measure the ODF directly and bypass the intermediate reconstruction of the diffusion function, much of which is ultimately dis-

carded by the radial projection. The above goal could be accomplished by a sampling/reconstruction scheme which sampled the diffusion signal directly on the sphere and reconstructed the ODF directly on the sphere.

The ability to sample directly on the sphere would allow us to spend the signal acquisitions more efficiently on *angular* resolution. In contrast, the signal acquisitions in conventional Cartesian Fourier reconstruction are invested in *spatial* resolution which contributes relatively inefficiently to the desired endgoal of angular resolution. Moreover, spherical sampling provides a more natural framework for describing angular resolution. Whereas the angular resolution of a spherical sampling scheme is upper-bounded by the angular distance between the sampling points, it is not clear how to define angular resolution in the context of Cartesian sampling. Additionally, with spherical sampling the acquisition can be targeted to the spatial frequency band where the angular contrast-to-noise is greater. In contrast, Cartesian Fourier reconstruction expends a significant portion of the acquisitions near the origin and tails of reciprocal space where the angular contrast-to-noise is relatively low.

The notion of sampling the diffusion signal on a sphere was first introduced in Chap. 7. However, the reconstruction involved an elaborate model-fitting procedure which was prone to model misspecification. Here, we present a novel, model-independent sampling and reconstruction scheme termed q-ball imaging. Q-ball samples the diffusion signal directly on the sphere, and reconstructs a function closely resembling the ODF obtained from explicit radial projection. The reconstruction scheme is based on the finding that integration over a great circle (the Funk transform [1]) in reciprocal space is equivalent to the Hankel transform of the planar projection of the diffusion function. We show experimentally that given equal imaging time q-ball imaging method provides significantly greater heterogeneity sensitivity and angular resolution than the DSI method presented in Chap. 8.

10.2 Theory

10.2.1 Fourier Relation

Stejskal and Tanner showed that the magnitude of the spin echo signal $E(\mathbf{q})$ from a PGSE experiment is directly related to the spin displacement probability density function (PDF) $P(\mathbf{R})$ by a Fourier relation

$$\begin{aligned} E(\mathbf{q}) &= E_0 \int P(\mathbf{R}) e^{i\mathbf{q}^T\mathbf{R}} \, d\mathbf{R} \\ &= E_0 \mathcal{F}[P(\mathbf{R})] \end{aligned} \tag{10.1}$$

where $E_0 = E(0)$ is the signal in the absence of the applied diffusion gradient, $\mathbf{R} = \mathbf{r} - \mathbf{r}'$ is the relative spin displacement in the experimental diffusion time τ, $\mathbf{q} = \gamma\delta\mathbf{g}$ is the spin displacement wave vector with γ the gyromagnetic ratio, δ the diffusion gradient duration, and $\mathbf{g}$ the diffusion gradient wave vector (see Chap. 4). The Fourier relationship between the spin echo magnitude and the PDF allows for direct reconstruction of the PDF by inverse Fourier transform of the diffusion signal with respect to the displacement wave vector

$$\begin{aligned} P(\mathbf{R}) &= E_0^{-1} \int E(\mathbf{q}) e^{-i\mathbf{q}^T\mathbf{R}} \, d\mathbf{q} \\ &= E_0^{-1} \mathcal{F}^{-1}[E(\mathbf{q})]. \end{aligned} \tag{10.2}$$

The DSI method exploits the above relationship to reconstruct the PDF within each imaging voxel. The PDF is then radially projected on to the sphere, yielding a function which we term the diffusion orientation distribution function.

10.2.2 Orientation Distribution Function

The PDF $P(\mathbf{R})$ can be projected on to the sphere via the radial projection

$$\psi(\mathbf{u}) = \int_0^\infty P(\rho\mathbf{u}) \, d\rho \tag{10.3}$$

where $\mathbf{u}$ is a unit normal vector referred to as the fiber director, and ρ is the radial coordinate in the diffusion space coordinate system. The function ψ is referred to as the spin displacement orientation distribution function (ODF). The ODF expresses the probability of a spin displacing into a differential solid angle about the fiber director $\mathbf{u}$. While the ODF representation sacrifices all of the radial information in the diffusion function, the ODF captures all of the relevant angular contrast.

In the DSI method (Chap. 8), the ODF is reconstructed by sampling the diffusion signal on a (keyhole) Cartesian grid, Fourier transformation, and then radial projection. The basic idea of the q-ball imaging method presented here is to sample the diffusion signal directly on the sphere and reconstruct the ODF directly on the sphere. The spherical inversion is accomplished with the reciprocal space Funk transform which we describe in the following section.

10.2.3 Reciprocal Space Funk Transform

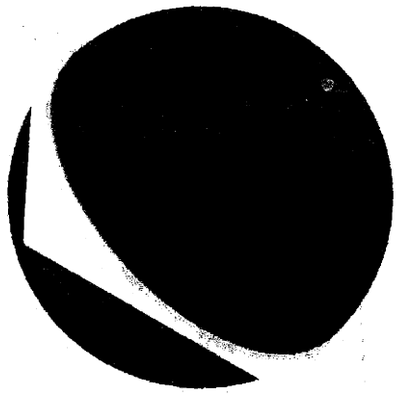

Figure 10-1: The Funk transform assigns the integral over an equator (yellow circle) to the value at the corresponding pole (green dot).

The Funk transform is a generalization of the Radon transform to the sphere. Specifically, the Funk transform maps functions on the sphere to functions on the sphere. For a given point on the sphere which we refer to as a pole, the Funk transform assigns the value at the pole to be the integral over the associated equator (Fig. 10-1). We can write the Funk transform $\mathcal{G}$ explicity as

$$\mathcal{G}(\mathbf{u})[f(\mathbf{u})] = \int_{S^2} f(\mathbf{u})\delta(\mathbf{u}^T\mathbf{w})\, d\mathbf{w} \qquad (10.4)$$

where $f(\mathbf{u})$ is a function on the sphere S^2, and $\mathbf{u}$ and $\mathbf{w}$ are unit vectors on the sphere. Here, we show that the Funk transform of the diffusion signal $E(\mathbf{q})$, where $\mathbf{q}$ is sampled on a sphere, yields an ODF which strongly resembles the ODF obtained by explicit radial projection (Eqn. 10.3).

The connection between the reciprocal space Funk transform and the radial transform can be written as follows. We begin by defining the projection $\mathcal{L}(\mathbf{u})$ of a function $f(\mathbf{x})$ on to a plane through the origin

$$\mathcal{L}(\mathbf{u})[f(\mathbf{x})] = \int_{-\infty}^{\infty} f(\mathbf{x} + \alpha\mathbf{u})\, d\alpha \tag{10.5}$$

where $\mathbf{u}$ is the unit vector normal to the plane. From the above relation we can see that

$$\psi(u) = \mathcal{L}(\mathbf{u})[P(0)]. \tag{10.6}$$

According to the central slice theorem the two-dimensional Fourier transform on a plane through the Fourier transform of function is equivalent to the projection of the function on to that plane. In terms of the above definition, the central slice theorem can be written

$$\mathcal{L}(\mathbf{u})[f(\mathbf{x})] = \mathcal{F}_2[\mathcal{I}(\mathbf{u})[\mathcal{F}[f(\mathbf{x})]]] \tag{10.7}$$

where $\mathcal{F}_2$ is the two-dimensional Fourier transform, and

$$\mathcal{I}(\mathbf{u})[f(\mathbf{x})] = f(\mathbf{x})\delta(\mathbf{x}^T\mathbf{u}) \tag{10.8}$$

is the intersection of the function with the plane through the origin with surface normal vector $\mathbf{u}$.

Instead of taking the two-dimensional Fourier transform on the plane, the reciprocal space Funk transform integrates over a circle in the reciprocal space, where the circle has a radius q'. The reciprocal space Funk transform for a sphere of radius q' can be written

$$\mathcal{G}(\mathbf{u}, q')[f(\mathbf{q})] = \int f(\mathbf{q})\delta(\mathbf{q}^T\mathbf{w})\delta(|\mathbf{q}| - q')\, d\mathbf{q}. \tag{10.9}$$

Using the result from the Appendix (Sec. 10.6) that the integral over a circle in reciprocal space is equivalent to the integral over the zeroth-order Hankel transform

$\mathcal{H}$ of the direct space function, we obtain

$$\mathcal{G}(\mathbf{u}, q')[\mathcal{F}[f(\mathbf{x})]] = \int_{R^2} \mathcal{H}(q')[\mathcal{L}(\mathbf{u})[f(\mathbf{x})]] \, d\mathbf{x} \tag{10.10}$$

where the integral is taken over the plane R^2. The above equation reveals that the reciprocal space Funk transform is simply the integral over the zeroth-order Hankel transform of the diffusion function projected on to the plane.

In order to restate the above result in the context of the diffusion experiment, if we identify $P(\mathbf{R})$ with $f(\mathbf{x})$ and, from Eqn. 10.1, $E(\mathbf{q})$ with $\mathcal{F}[f(\mathbf{x})]$ then we have

$$\mathcal{G}(\mathbf{u}, q')[E(\mathbf{q})] = \int_{R^2} \mathcal{H}(q')[\mathcal{L}(\mathbf{u})[P(\mathbf{R})]] \, d\mathbf{R}. \tag{10.11}$$

Hence, the integral of the diffusion signal over any circle around the origin is equal to the integral over the projection of the diffusion function on the plane of the circle multipled by a zeroth-order Bessel Function. It might be helpful to restate the above result in plain language. Summing the diffusion signals over a circle around the origin is equivalent to the following steps: projecting the diffusion function on to the plane containing the circle, multiplying the projection by a zeroth-order Bessel function, and then summing over the modified projection.

If the kernel of the Hankel transform were a delta-function instead of a Bessel function then the transform given by Eqn. 10.11 would be identical to the radial projection transform given by Eqn. 10.3. Hence, the width of the Bessel function in the Hankel transform determines the angular resolution of the projection, where the width of the Bessel function is specified by the radius of the reciprocal space sphere. Owing to the linearity of the reciprocal space Funk transform it would be possible to design sampling schemes with multiple spheres in order to achieve a kernel more closely resembling a delta-function, and thereby increase the angular resolution.

10.3 Methods

10.3.1 Imaging

One diffusion spectrum image (Experiment A) and two q-ball images (Experiments B and C) were acquired on a healthy volunteer on a 3T Siemens Allegra. Experiment A provided a standard DSI image for comparison purposes, and Experiments B and C provided, respectively, a lower and higher spatial frequency q-ball acquisition. All three experiments used the constant gradient twice-refocused balanced echo sequence described in Chap. 8 although the imaging parameters and sampling schemes differed. The slice prescription for all three experiments was identical and consisted of two sagittal slices with isotropic 2.8mm resolution and a 6.72mm gap. Whole-head mprage images were also acquired for anatomical reference. For all three experiments, one image with no diffusion weighting was also acquired.

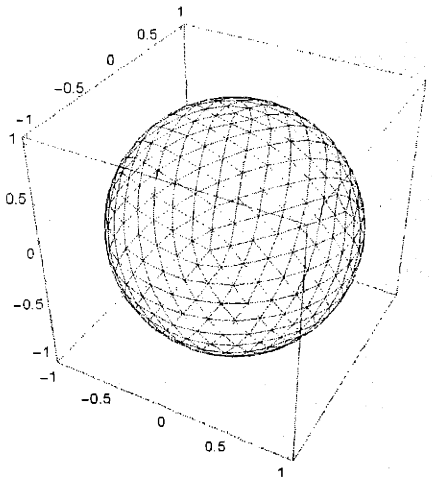

Figure 10-2: Gradient directions for the q-ball imaging experiment. The 493 gradient directions were obtained from the vertices of a 7-fold tessellated icosahedron.

The imaging parameters for the DSI experiment (Experiment A) were TR/TE/Δ/δ = 800/143/66/61ms, $b_{\max} = 1.7 \times 10^4 \mathrm{s/mm}^2$. 515 q-space points were sampled on a keyhole Cartesian grid with $g_{\max}$=40mT/m and $q_{\max} = 0.66 \mu\mathrm{m}^{-1}$. For both q-ball experiments (Experiments B and C) the q-space sampling points were obtained from the $n = 492$ vertices of a 7-fold tessellated icosahedron (Fig. 10-2). This scheme gives an average minimum angular distance between points of $9.30 \pm 0.76°$. The parameters for the first q-ball experiment (Experiment B) were TR/TE/Δ/δ= 800/98/44/39ms, $b_{\max} = 4.0 \times 10^3 \mathrm{s/mm}^2$, $g_{\max}$= 40mT/m, $q = 0.36 \mu\mathrm{m}^{-1}$, and the parameters for the second q-ball experiment (Experiment C) were TR/TE/Δ/δ=800/130/60/55ms, $b_{\max} = 1.2 \times 10^4 \mathrm{s/mm}^2$, $g_{\max}$=40mT/m, $q = 0.54 \mu\mathrm{m}^{-1}$. Experiments B and C will

be referred to, respectively, as the low and high spatial frequency q-ball experiments. We will also refer to Experiment D as the average of the images from experiments B and C.

10.3.2 Reconstruction Algorithm

The DSI data were reconstructed and visualized as described in Chap. 8. The q-ball data were reconstructed using the reciprocal space Funk transform which was implemented in practice as follows.

The acquired data are denoted $E(\mathbf{q}_j)$ where $\mathbf{q}_j$ are the q-space sampling points described in the Methods section. For a given direction $\mathbf{u}_i$ in the direct space the associated great circle was described by a set of $n = 36$ uniformly spaced points. The points were sampled over angles $\theta_j = 2\pi j/n$, $j = 1, .., n$. The radius of the great circle is denoted q'. The great circle points corresponding to the direction $\mathbf{u}_i$ are then

$$\mathbf{q}(q', \theta_j, \mathbf{u}_i) = q'\mathbf{H}_i(\cos(\theta_j)\ \sin(\theta_j)\ 0)^T \tag{10.12}$$

where

$$\mathbf{H}_i = \begin{cases} \frac{(\mathbf{z}+\mathbf{u}_i)(\mathbf{z}+\mathbf{u}_i)^T}{1+\mathbf{z}^T\mathbf{u}_i} - \mathbf{I} & \mathbf{u}_i \neq \mathbf{z} \\ \mathbf{I} & \mathbf{u}_i = \mathbf{z} \end{cases} \tag{10.13}$$

and $\mathbf{z} = (0\ 0\ 1)$.

Due to the fact that the geodesic sampling scheme does not have uniformly spaced points along an arbitrary equator it was necessary to interpolate the data. The interpolation was performed using kernel regression (2). The kernel regression estimate $\hat{E}(\mathbf{q}_j)$ for the diffusion signal at point $\mathbf{q}_j$ is

$$\hat{E}(\mathbf{q}_j) = \frac{\sum_i E(\mathbf{q}_i)G(\mathbf{q}_i, \mathbf{q}_j)}{\sum_i G(\mathbf{q}_i, \mathbf{q}_j)} \tag{10.14}$$

where the kernel $G(\mathbf{q}_i, \mathbf{q}_j)$ is a truncated Gaussian kernel with standard deviation of $\sigma = 10°$ and a cutoff of $\alpha_c = 20°$. If the angle between two reciprocal space vectors

$\mathbf{q}_i$ and $\mathbf{q}_j$ is denoted $\alpha_{ij} = \angle(\mathbf{q}_i, \mathbf{q}_j)$ then the kernel can be written

$$G(\mathbf{q}_i, \mathbf{q}_j) = e^{-\alpha_{ij}^2/(2\sigma^2)}\theta(\alpha_c - \alpha_{ij}) \tag{10.15}$$

where θ is the Heaviside step function.

For a specified direction $\mathbf{u}_i$ in the direct space, the great circle sum $h(\mathbf{u}_i)$ is then

$$h(\mathbf{u}_i) = \sum_j \hat{E}(\mathbf{q}(q', \theta_j, \mathbf{u}_i)). \tag{10.16}$$

For each voxel the great circle sum was caluclated for the $m = 752$ vertices of a 5-fold tessellated dodecahedron. As with the ODFs reconstructed from the DSI data, the ODFs reconstructed from the q-ball data were normalized to $[0, 1]$ for visualization purposes.

10.4 Results

Fig. 10-3 shows a comparison of the ODF maps obtained from Experiments A-C. The images are taken from the crossing of the corpus callosal (cc) striations to motor cortex with the ascending corona radiata (cr). In all images we can resolve the intersection of the cc striations with the cr. The low frequency q-ball image shown in Fig. 10-3b shows almost identical architecture to the the DSI shown in Fig. 10-3a. In the low frequency q-ball image (b) the ODF peaks are slightly sharper and are more uniform in width.

The high frequency q-ball image reveals structural detail not seen in either the DSI or the low-frequency q-ball image. Specifically, the callosal striations interdigitate the corona radia over a wider area including the anteroposterior-directed association fibers at the sulcal base. The fiber intersections display a more uniform density, as opposed to the discrete appearance of the intersections in images a and b. The intersection between the corpus callosum and the cingulum, and between the corona radiata and the cingulum is also clearly seen.

Fig. 10-4 shows a coronal section of the right frontal and temporal lobes taken

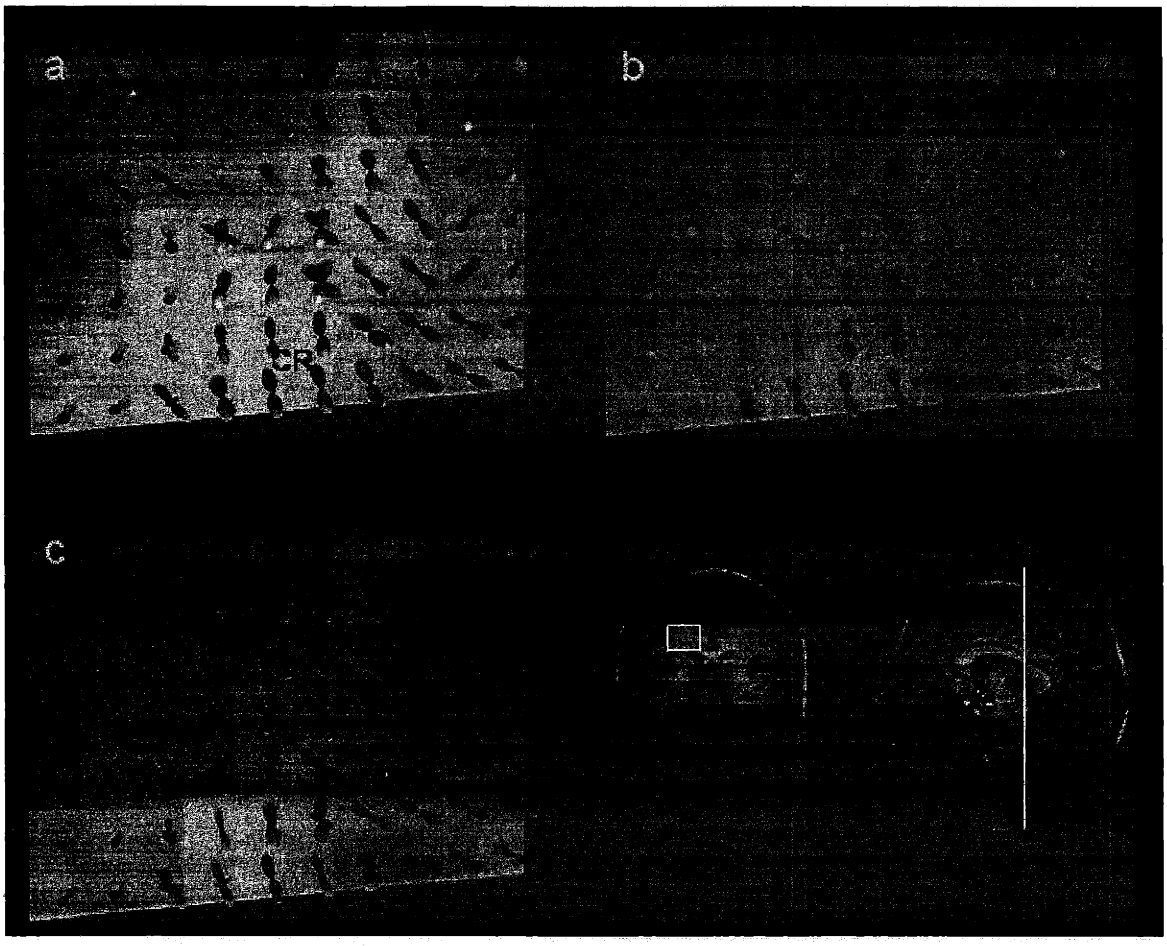

Figure 10-3: Comparison of (a) DSI, and (b) low and (c) high spatial frequency q-ball images. The images are sagittal slices taken from the intersection of striations from the corpus callosum with the the corona radiata. The ROI and anteroposterior level are shown in the mp-rage images at bottom right. The peaks of the ODFs are colored according to their direction with red indicating mediolateral, green anteroposterior, and blue superoinferior. The brightness is scaled by the height of the peak. Images a-c correspond, respectively, to experiments a-c: (a) DSI at $q_{\text{max}} = 0.66\mu\text{m}^{-1}$, (b) q-ball at $q_{\text{max}} = 0.36\mu\text{m}^{-1}$, and (c) q-ball at $q_{\text{max}} = 0.54\mu\text{m}^{-1}$. The grayscale background image is the sum of all the diffusion-weighted images for a particular experiment. CC corpus callosum, CR corona radiata, CST corticospinal tract, Ci cingulum, SLF superior longitudinal fasciculus.

from Experiment D. The gyri are identified SMG for the supramarginal gyrus, STG for the superior temporal gyrus, and MTG for the middle temporal gyrus (MTG). All gyri have approximately mediolateral white matter fiber orientation (inplane, red). At the crown of the gyri, anteroposterior (out-of-plane, green) fiber components are seen (yellow arrows) which we identify as intracortical fiber populations within the gyral crown.

Along the gyri, superoinferior (in-plane, blue) fiber orientations are seen (white arrows), most likely due to the insertion of the white matter fibers into the gray matter, which is known to occur perpendicular to the cortical surface, but in plane with the white matter fiber populations. Due the relatively larger number of these fibers compared to the intracortical fibers, the latter can be hard to detect along the gyral wall. A couple of examples can be made out though, shown as green arrows. At the crown the white matter fiber insertions would be indistinguishable from the white matter fiber population (see enlarged insert). The insert shows the crossing between the white matter fiber (mediolateral, red) insert into gray matter and the intracortical fiber populations (anteroposterior, green).

10.5 Discussion

In this chapter we presented a method for sampling and reconstructing the spin displacement ODF directly on the sphere. The reconstruction was based on the reciprocal space Funk transform and yielded an ODF which functionally closely resembles the spin displacement ODF obtained by explicit radial projection of the Cartesian diffusion function. However, given the ability of the spherical sampling scheme to directly target a spatial frequency band where the angular contrast-to-noise is greater, the spherical reconstruction scheme affords significantly greater complexity sensitivity than the Cartesian Fourier reconstruction employed by the DSI method (Chap. 8).

The greater complexity sensitivity of the q-ball method relative to DSI was demonstrated at the intersection of the corpus callosum with the corona radiata where the q-ball method revealed a continuous interdigitation of fibers whereas the DSI recon-

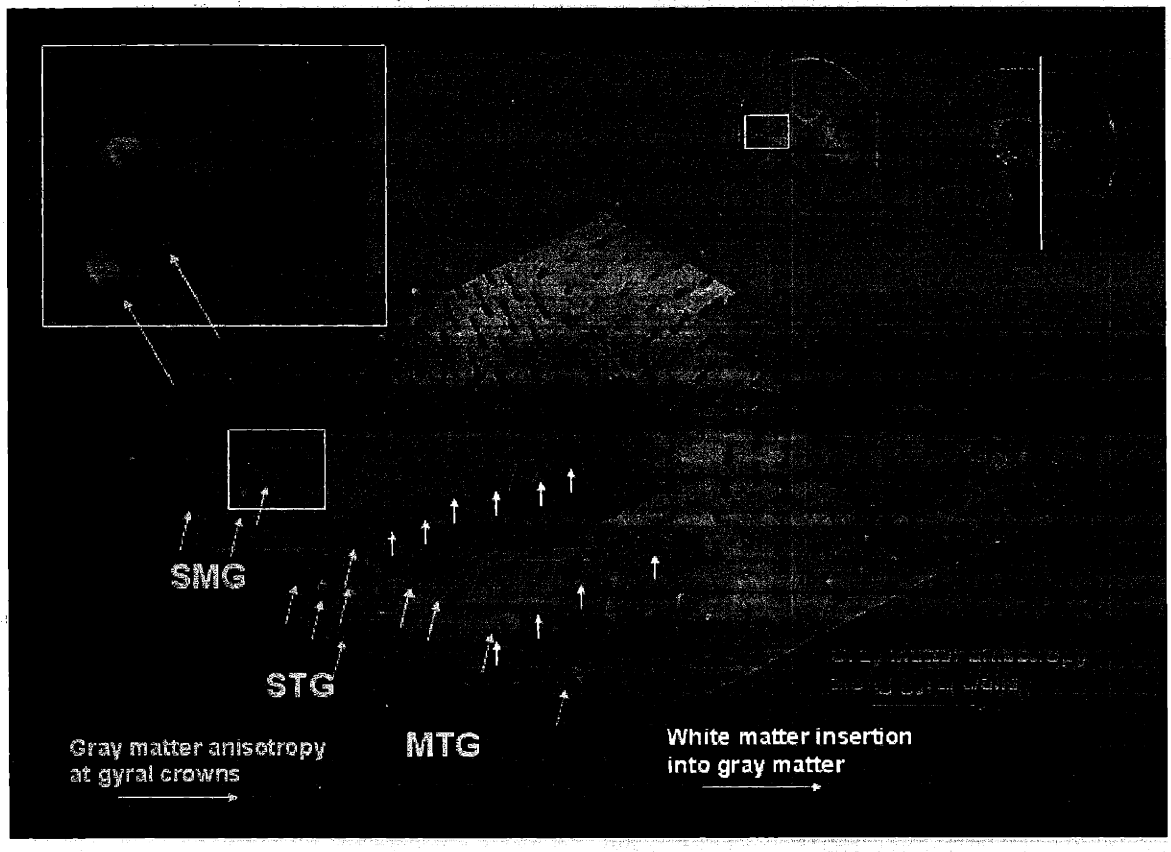

Figure 10-4: Q-ball image (Experiment D) from the temporal lobe. The ROI and anteroposterior level are shown in the mp-rage images at top right. The zoomed insert shown at top left is taken from the region indicated by the yellow square at the crown of SMG. The peaks of the ODFs are colored according to their direction with red indicating mediolateral, green anteroposterior, and blue superoinferior. The brightness is scaled by the height of the peak. Yellow arrows point to gray matter anisotropy at a gyral crown; white arrows to white matter interstions into gray matter; and green arrows to gray matter anisotropy at gyral walls. SMG supramarginal gyrus, STG superior temporal gyrus, MTG medial temporal gyrus.

struction exhibited a more discrete intersection geometry. The complexity sensitivity of the q-ball method was also demonstrated for gray matter architecture where we observed composite diffusion structure at the gyral crowns in the temporal lobe corresponding, putatively, to intracortical connection architecture. To our knowledge this represents the first demonstration of anatomically significant structure in gray matter with diffusion imaging.

The greater complexity sensitivity exhibited by the high spatial frequency q-ball acquisition relative to the lower spatial frequency acquisition indicates that there exists a spatial frequency which will optimize the complexitiy sensitivity. Future work will need to investigate the complexitiy sensitivity as a function of spatial frequency, i.e., the radius of the q-ball. As the optimal spatial frequency will be a function of the underlying diffusion, the optimal spatial frequency may differ for white and gray matter. Hence, the radius of the q-ball will need to be specified based on the anatomical target.

The angular resolution, and consequently the complexity sensitivity, of the q-ball acquisition is determined by the radius of the q-ball. By obtaining acquisitions with multiple radii it should be posssible to design filters with sharper angular resolution. Ideally, the multiplication kernel should be a delta-function in which case the q-ball acquisition will be theoretically identical to the radial projection transform of the Cartesian diffusion function.

In the cgTRBE sequence (Chap. 8) employed by both the DSI and q-ball experiments presented here, the diffusion gradient is on during approximately the entire experiment. As a result the diffusion time differs for different echo times; specifically, the diffusion time is roughly half of the echo time. The q-ball experiments obtained here had a lower TE than the DSI experiment and therefore had a lower effective diffusion time. The greater structural complexity observed in the high frequency q-ball experiment relative to the DSI may therefore be due then to the shorter diffusion time and not any inherent sensitivity increase provided the q-ball sampling/reconstruction scheme.

Whether the increased complexity sensitivity is due to the lower diffusion time of

the reconstruction scheme could be investigated by employing a conventional pulsed gradient spin echo experiment and setting the diffusion time to be the same for the DSI and q-ball reconstructions. However, the greater complexity seen in the high frequency q-ball image relative to the low frequency q-ball image, which had a shorter diffusion time, would tend to argue that the enhanced complexity sensitivity is inherently due to the q-ball reconstruction scheme and not the shorter diffusion time.

In sum, we have presented a method for sampling and reconstructing a spin displacement ODF directly on the sphere. The sensitivity of the method to complex structure is determined by the radius of the reciprocal space sphere, which also affects the signal-to-noise. Given the inherent trade-off between signal-to-noise and voxel resolution, further work will be required to determine the optimal trade-off between angular and spatial resolution for resolving a particular anatomical structure of interest.

10.6 Appendix

We wish to show that integration over a circle in reciprocal space is equivalent to integration of the two-dimensional Hankel transform of the direct space function projected on to the plane containing the circle. The direct space function is denoted $F(\mathbf{x})$ and the projection of the direct space function on to the plane is denoted

$$f(\mathbf{r}) = \int_{-\infty}^{\infty} F(\mathbf{r} + \alpha\mathbf{u})\, d\alpha. \tag{10.17}$$

Following here on, $\mathbf{r}$ is understood to be a two-dimensional vector in the plane. The intersection of the plane with the reciprocal space function is written as $s(\mathbf{q})$ where $\mathbf{q}$ is a two-dimensional vector in the plane.

The central slice theorem can then be written

$$f(\mathbf{r}) = \int s(\mathbf{q}) e^{i\mathbf{q}^T\mathbf{r}}\, d\mathbf{q} \tag{10.18}$$

If instead of taking the two-dimensional Fourier transform we simply integrate over a circle of radius q' in the plane we have

$$h = \int s(\mathbf{q})\delta(|q| - q')\ d\mathbf{q} \tag{10.19}$$

where h is the integral over the circle. This is the reciprocal space Funk transform. Substituting Eqn. 10.18 into the above equation gives

$$\begin{aligned} h &= \int f(\mathbf{r})e^{i\mathbf{q}^T\mathbf{r}}\delta(q - q')\ d\mathbf{q}\ d\mathbf{r} && (10.20)\\ &= \int f(r,\theta_r)e^{iqr\cos(\theta_q-\theta_r)}\delta(q - q')q\ dq\ d\theta_q\ r\ dr\ d\theta_r. && (10.21) \end{aligned}$$

Taking the Jacobi-Anger expansion (3) yields

$$h = \int f(r,\theta_r) \sum_{n=-\infty}^{\infty} i^n J_n(qr)e^{in(\theta_q-\theta_r)}\delta(q - q')\ q\ dq\ d\theta_q\ r\ dr\ d\theta_r. \tag{10.22}$$

Evaluating the above integral we obtain

$$\begin{aligned} h &= q' \int f(r,\theta_r) \sum_{n=-\infty}^{\infty} i^n J_n(q'r)e^{in(\theta_q-\theta_r)}\ d\theta_q\ r\ dr\ d\theta_r && (10.23)\\ \therefore\ &= 2\pi q' \int f(r,\theta_r)J_0(q'r)\ r\ dr\ d\theta_r. && (10.24) \end{aligned}$$

which is the zeroth-order Hankel transform.

10.7 References

[1] P. Funk. Über eine geometrische Anwendung der Abelschen Integralgleichnung. *Math. Ann.*, 77:129–135, 1916.

[2] E. Parzen. On the estimation of a probability density function and mode. *Ann. Math. Stat.*, 33:1065–1076, 1962.

[3] G.B. Arfken and H.-J. Weber. *Mathematical methods for physicists.* Harcourt/Academic Press, New York, 2000.

Chapter 11

Conclusions

11.1 Summary

In this thesis I developed a set of diffusion imaging methods for measuring the spin diffusion function *in vivo*. In contrast to previous approaches, most notably diffusion tensor imaging, the diffusion spectrum (Chap. 8) and q-ball (Chap. 10) imaging methods presented here do not invoke any assumptions on the underlying diffusion process. The model-independent picture of the diffusion function revealed white matter tissue architecture previously thought to be beyond the scope of diffusion imaging. For example, we demonstrated the ability to resolve deep white matter intersections, composite tissue structure at the cortical margin, and fiber-specific degeneration in neurodegenerative pathology.

While we have endeavored to develop a robust, principled method for model-free diffusion imaging *in vivo*, there remain, thankfully and regrettably, a number of open problems. I hope that this thesis has helped in some small way to formulate the problems in an answerable form, and has provided some of the tools which may someday help to answer them.

11.2 Open Problems

11.2.1 Experimental

Where does diffusion anisotropy come from?

The interpretation of *in vivo* diffusion imaging rests on the notion that spin diffusion is restricted by diffusion barriers. However, the identity of the biophysical barrier or barriers responsible for diffusion restriction in tissue, particularly brain tissue, is not fully known. The experimental evidence indicates that myelination is not required for diffusion anisotropy (1–4), neurofilaments do not contribute significantly to diffusion anisotropy (5), and the neural membrane is relatively permeable to water, all results which raise significant questions about the identity of the diffusion barrier.[1] The picture is further confounded by the common misinterpretation of non-Gaussian diffusion as necessarily arising from multi-component diffusion, although such behavior can be due to diffusion restriction as well. The ability of diffusion spectrum imaging to quantitatively measure the diffusion function may help identify the diffusion barriers which in turn would greatly facilitate the interpretation of diffusion imaging results in general.

What is the trade-off between anatomical and diffusion space resolution?

The diffusion spectrum imaging method presented in this thesis (Chap. 8) measures the microscopic spin diffusion function within each voxel. Similarly, the q-ball imaging method (Chap. 10) measures a modified radial projection of the spin diffusion function within each imaging voxel. Hence, both methods measure the microscopic diffusion function, or a property thereof in the case of the q-ball method, in the context of macroscopic anatomy. Whereas the macroscopic resolution is on the order of millimeters, the diffusion space resolution is on the order of microns. Hence, there are two resolution domains which communicate via orientation.

The signal-to-noise constraints inherent to spin displacement imaging force an

[1]For an excellent review of the current understanding of the mechanisms of diffusion anisotropy in brain tissue the interested reader is referred to Ref. 6.

experimental trade-off between the spatial resolution in the microscopic and macroscopic domains: increased spatial resolution of the anatomy comes at the expense of lower resolution of the diffusion function, and vice versa. As we have seen, higher diffusion spatial resolution enhances the experimental sensitivity to complex tissue structure, but the associated decrease in signal-to-noise reduces the confidence in that observed structure. But where exactly is the optimal trade-off between resolution and confidence? For example, is it optimal to acquire diffusion imaging data with, say, 2μm resolution of the diffusion function and 2mm resolution of the anatomy, or $1mum$ and 4mm resolution of the anatomy? The answer certainly depends on the anatomical target or the hypothesis being evaluated, but given these how should the trade-off be determined. Presently the experimental picture of what structure is gained and lost as we vary the resolution trade-off is far from complete.

What are the roles of the diffusion time and the diffusion gradient duration?

The experiments presented in this thesis measured the diffusion function at a fixed diffusion time and fixed diffusion gradient duration, and therefore provided a static picture of the diffusion function. However, the evolution of the diffusion function over time may shed considerable light on to the spatial structure as well. For example, were two diffusion peaks to merge over time then one could infer the approximate exchange distances between the compartments.

In addition to providing insight into the exchange regimes, the temporal evolution of the diffusion function may also help improve the orientational contrast to noise. Specifically, if the spin diffusion is restricted perpendicular to fibers but relatively free in the direction of the fibers, then the peaks of the orientation distribution functions should become sharper with time. This effect will compete with the possible blurring of the spectral peaks due to the increased exchange between orientational compartments at longer diffusion times. It remains to be tested empirically which effect dominates. We also note that if the effect of the diffusion gradient duration is to expel the diffusion function away from diffusion barriers (Chap. 8) then the diffusion peaks should also sharpen with longer diffusion gradients. This also remains to be

tested.

11.2.2 Theoretical

What does contrast-to-noise mean in diffusion projective space?

The diffusion spectrum imaging method presented in Chap. 8 measures the diffusion function within each voxel. The diffusion function was visualized and analyzed in terms of the projection of the diffusion function on to a sphere, a transformation which we called the radial projection transform. The resulting function was termed a diffusion orientation distribution function. The q-ball imaging method (Chap. 10) allows for direct reconstruction of the orientation distribution function and therefore does not require post-processing to obtain the function.

Both methods contain a number of experimental design parameters: the voxel resolution, the diffusion space resolution, the number of reciprocal space sampling points, the reconstruction scheme, the diffusion time, etc. Conventionally in imaging, experimental parameters can be selected so as to maximize some predefined contrast-to-noise function. For example, if we know the T2 of two different tissue types which we would like to discriminate we could select a TE to provide the optimal contrast-to-noise.

However, it is not clear how to define contrast-to-noise in the context of the orientation distribution function. The problem is principally due to the fact that the diffusion peaks have no simple analytical form and consequently the contrast-to-noise function cannot be written a priori. For the same reason, conventional measures of spectral resolution such as the full-width at half-max may poorly characterize the true spectral resolution. It also needs to be borne in mind that the peaks are continuous and overlapping and not discrete, and so any measure which has to identify and characterize discrete peaks is prone to identification error. For this reason spectral width fails to be a valid measure simply because it does not discriminate between simple and complex diffusion. For example, if the diffusion is truly composite then a reconstruction which provides a single sharp peak would be less desirable than one which gave multiple slightly broader peaks. What is called for then is a contrast

measure that can simultaneously reward spectral resolution and complexity.

What is the relationship between the observed diffusion and the underlying tissue structure?

The infererence of actual tissue microstructure from the observed diffusion function is severely restricted by our limited understanding of the physical relationship between diffusion and structure. As Stejskal noted in his classic paper (7): "As an investigative tool, the method had an incomplete ability to analyze the experimental data in terms of an unambiguous structure or behavior. The experimental problem is far from simple." In interpreting the diffusion imaging experiments presented here we have drawn on the principle that directions of enhanced diffusion correspond to fiber directions, but if we attempt to infer more detailed structural properties such as the morphology of the diffusion space we find ourselves at a loss. For example, in Chap. 9 on the tractography problem the diffusion and fiber orientation distribution functions could only be related at a phenomenological level.

While the diffusion-structure mapping problem may benefit from numerical simulations of diffusion in toy models of white matter, the number of biophysical unknowns and the complexity of brain tissue structure will ultimately limit the accuracy of such models. Perhaps the most glaring gap in our understanding of the diffusion-structure relation is the fact that the biophysical barriers responsible for diffusion anisotropy have not been unequivocally identified. Further, the role of surface relaxation, surface permeability and cellular transport in shaping the diffusion function is not fully known. Hopefully, theory and experiment can mutually contribute to a better understanding of the diffusion-structure relationship *in vivo*.

The most positive outcome of such a project would be the ability to directly infer the morphology of the diffusion space from the diffusion function. This prospect is not as unlikely as it might seem if we consider that in the long-time limit for fully bounded diffusion, the diffusion function is exactly the spatial auto-correlation of the diffusion space. If a similar relationship could be developed for intermediate times and more general boundary conditions then, paraphrasing Kac (8), we might be able

indeed to 'hear the shape of brain tissue'.

11.3 References

[1] C. Beaulieu, F.R. Fenrich, and P.S. Allen. Multicomponent water proton transverse relaxation and T2-discriminated water diffusion in myelinated and nonmyelinated nerve. *Magn. Reson. Imag.*, 16:1201–1210, 1998.

[2] C. Beaulieu and P.S. Allen. Determinants of anisotropic water diffusion in nerves. *Magn. Reson. Med.*, 31:394–400, 1994.

[3] D.M. Wimberger, T.P. Roberts, A.J. Barkovich, L. M. Prayer, M.E. Moseley, and J. Kucharczyk. Identification of "premyelination" by diffusion weighted MRI. *J. Comput. Assist. Tomogr.*, 19:28–33, 1995.

[4] J. Ono, K. Harada, M. Takahashi, M. Maeda, K. Ikenaka, K. Sakuri, N. Saki, T. Kagawa, B. Fritz-Zieroth, T. Nagai, Ä. Nihei, S Hashimoto, and S. Okada. Differentation between dysmyelination and demyelination using magnetic resonance diffusional anisotropy. *Brain Res.*, 671:141–148, 1995.

[5] C. Beaulieu and P.S. Allen. Water diffusion in the giant axon of the squid: implications for diffusion-weighted MRI of the nervous system. *Magn. Reson. Med.*, 32:579–583, 1994.

[6] D.G. Norris. The effects of microscopic tissue parameters on the diffusion weighted magnetic resonance imaging experiment. *NMR in Biomedicine*, 14:77–93, 2001.

[7] E.O. Stejskal. Use of spin echoesd in a pulsed magnetic-field gradient to study anisotropic, restricted diffusion and flow. *J. Chem. Phys.*, 43:3597–3603, 1965.

[8] M. Kac. Can one hear the shape of a drum? *Am. Math. Monthly*, 73:1–7, 1966.

Appendix A

Notation

Multiple definitions are separated by a slash.

$\mathbf{A}$	microstructure correlation tensor
β	fiber stiffness function / prior fiber ODF
b	b-value
$\mathbf{B}$	B-matrix
χ	characteristic function of the pore space
C	connectivity matrix
$\mathcal{C}$	pore space
δ	duration of diffusion gradient
Δ	time between diffusion gradients
d_e	extracellular diffusion
d_i	intracellular diffusion
d_ν	diffusion tensor eigenvalue
D	diffusion coefficient
D_0	free space diffusion coefficient
$\mathbf{D}$	diffusion tensor
$\mathcal{D}$	path differential
$\mathbf{e}_\nu$	diffusion tensor eigenvector
E	spin echo signal
E_0	spin echo signal in the absence of an applied diffusion gradient
E_n	diffusion propagator eigenvalue

$\mathcal{F}$	Fourier transform
$\mathcal{F}_2$	two-dimensional Fourier transform
$\mathcal{F}^{-1}$	inverse Fourier transform
γ	gyromagnetic ratio
$\mathbf{g}$	diffusion gradient
$\mathcal{G}$	Funk transform
$\mathcal{H}$	Hankel transform
$\mathcal{I}$	planar intersection
$\mathbf{j}$	spin flux
κ	fiber stiffness modulus
ℓ	diffusion mixing length
λ_e	extracellular transport
λ_i	intracellular transport
λ_ν	diffusion tensor eigenvalue / general transport tensor eigenvalue
$\mathbf{\Lambda}$	diffusion tensor eigenvalue matrix
$\mathcal{L}_\mathbf{u}$	projection on to plane with unit normal vector $\mathbf{u}$
μ	surface relaxation
m_+	complex magnetization vector
$\mathbf{n}$	diffusion compartment surface normal
$\partial\Omega$	diffusion compartment boundary
ρ	bulk relaxation
φ	spin phase / empirical fiber ODF
ϕ	spin velocity autocorrelation function / posterior fiber ODF
ϕ_i	intracellular volume fraction
ϕ_e	extracellular volume fraction
$\boldsymbol{\phi}$	spin velocity autocorrelation tensor
Φ	probability of path
Φ^*	probability of most probable path
p	initial spin density
$P(\mathbf{r}, \mathbf{r}', \tau)$	diffusion propagator, cPDF
$P(\mathbf{R}, \tau)$	ensemble-average propagator, PDF
$\mathcal{P}$	surface permeability

$\mathbf{q}$	spin displacement wave vector
$\mathbf{r}$	final spin position
$\mathbf{r}_{\mathrm{cm}}$	final COM spin position
$\mathbf{r}'$	initial spin position
$\mathbf{r}'_{\mathrm{cm}}$	initial spin position
$\mathbf{R}$	relative spin displacement / diffusion tensor eigenvector matrix
$\mathbf{R}_{\mathrm{cm}}$	COM relative spin displacement
σ_e	extracellular conductivity
σ_i	intracellular conductivity
σ_ν	conductivity tensor eigenvalue
$\boldsymbol{\sigma}$	conductivity tensor
s	coordinate along fiber path
S_p	surface area of diffusion compartment interfaces
ψ	spin displacement ODF
τ	diffusion time
τ_c	diffusion correlation time
Θ	return-to-origin probability
T	diffusion tensor trace
u_n	diffusion propagator eigenfunction
$\mathbf{u}$	spin displacement orientation / fiber orientation
$\mathbf{U}$	unit tensor
$\mathbf{v}'$	initial spin velocity
$\mathbf{v}$	final spin velocity
V_p	volume of the excluded diffusion space
$\mathbf{x}$	voxel position / path position
Ξ	tractography path
Ξ^*	most probable tractography path

Appendix B

Abbrevations

ADC	apparent diffusion coefficient
cg	constant gradient
cPDF	conditional spin displacement probability density function
COM	center-of-mass
DSI	diffusion spectrum imaging
DTI	diffusion tensor imaging
EAP	ensemble average propagator
ECG	electrocardiogram
FA	fractional anisotropy
IVOH	intravoxel orientational heterogeneity
MLE	maximum likelihood estimate
MRI	magnetic resonance imaging
NMR	nuclear magnetic resonance
ODF	orientation distribution function
PDF	spin displacement probability density function
PGSE	pulsed gradient spin echo
ROI	region of interest
RTO	return-to-origin probability
TE	echo time
TR	repetition time
TRBE	twice-refocused balanced echo